Synthesis and Aqueous Self-assembly of Atactic and Isotactic Poly(butylene oxide)-*block*-poly(glycidol) Diblock Copolymers

Inauguraldissertation

zur Erlangung der Würde eines Doktors der Philosophie

vorgelegt der

Philosophisch-Naturwissenschaftlichen Fakultät

der Universität Basel

von

Riccardo Pascal Wehr

2021

Genehmigt von der Philosophisch-Naturwissenschaftlichen Fakultät

auf Antrag von

Prof. Dr. Wolfgang Meier (Universität Basel)

Erstbetreuer

Prof. Dr. Cornelia Palivan (Universität Basel)

Zweitbetreuerin

Prof. Dr. Andreas Walther (Johannes Gutenberg-Universität Mainz)

Externer Experte

Basel, den 21.09.2021

Prof. Dr. Marcel Mayor

Dekan

Table of Contents

Abstract

Aqueous self-assembly of amphiphilic block copolymers (BCPs) is studied extensively for biomedical applications such as drug delivery, nano- or microreactors or artificial cell mimics. The commonly used poly(ethylene glycol) (PEG) as hydrophilic block and poly(dimethyl siloxane) (PDMS) as hydrophobic block suffer from several drawbacks regarding synthesis, reproducibility or biocompatibility. As potent alternatives, poly(glycidol) (PG) as hydrophilic block and poly(butylene oxide) (PBO) as hydrophobic block have gained increasing interest, benefiting from their easy synthesis, high biocompatibility and flexibility. In this thesis, a quick and well-controlled microwave-assisted synthesis of poly(butylene oxide)-*block*-poly(glycidol) (PBO-*b*-PG) amphiphilic BCPs is presented together with a straight-forward self-assembly protocol. Depending on the hydrophilic mass fraction of the BCPs, nanoscopic micelles, worms and polymersomes (Small Unilamellar Vesicles, SUVs) were formed as well as microscopic giant unilamellar vesicles (GUVs). The self-assemblies were analysed regarding their size and shape, using a combination of light scattering and electron and fluorescence microscopy techniques. A strong dependence of the formed morphology on the self-assembly method was discovered, proving that only solvent exchange led to the formation of homogenous phases.

Additionally, this work takes advantage of the possibility to introduce chirality into the PBO-*b*-PG backbones to create fully isotactic BCPs. The commonly used isotactic BCPs such as poly(L-lactic acid) or poly(propylene oxide) typically exhibit (semi-) crystalline behaviour, inducing high membrane stiffness and limiting their applicability in systems involving membrane proteins or sensitive cargo. Here, isotactic yet fully amorphous PBO-*b*-PG BCPs are introduced in order to overcome these limitations. Three PBO-*b*-PG BCPs, differing solely in their tacticities (*R*/*S*, *R* and *S*), were synthesised and characterised regarding their structural, optical and thermal properties. Their self-assembly into homogenous phases of SUVs was analysed, revealing stability differences between SUVs composed of the different BCPs. Additionally, GUVs were prepared by double emulsion microfluidics. Only the atactic BCP formed GUVs which were stable over several hours, whereas GUVs composed of isotactic BCPs ruptured within several minutes after formation. The ability of atactic PBO-*b*-PG to form microreactors was elucidated by reconstituting the membrane protein OmpF in the GUVs membrane and performing an enzyme reaction inside its lumen. A comparison with the established PDMS-*b*-PMOXA revealed that PBO-*b*-PG GUVs were more permeable to hydrophilic substrates. Hence, this study sets the basis to create functional nano- or microreactors composed of fully amorphous isotactic BCPs. It allows to assess how BCP tacticity affects the formation, morphology, stability and membrane thickness of SUVs and GUVs without affecting the membrane flexibility. This, in turn, will open a path to access interaction of the membrane forming isotactic BCPs with chiral cargo or chiral membrane proteins.

Acknowledgements

I am deeply grateful to everybody who supported me within the last four years of my PhD and who made this journey so valuable and unforgettable for me.

First and foremost I thank Prof. Wolfgang Meier for the opportunity to work in his group on such an interesting project. Thanks a lot for all the freedom, support, ideas and help I received from you over the last years and the chance to grow and advance under your supervision. I also thank Prof. Cornelia Palivan for the discussions and feedback from your side and the support and trust throughout my stay in your groups. I am grateful to Prof. Andreas Walther for the evaluation of my thesis and the PhD examination. Thanks to Prof. Daniel Häussinger for agreeing to chair the examination.

A huge thank you goes out to all current and former group members of the awesome Meier/Palivan groups. I want to thank especially Dr. Jens Gaitzsch for all his ideas, support and feedback and for accompanying me through all my publications and this thesis. A big thank you goes also to Dr. Davy Daubian, who helped me a lot in the lab, with writing or proofreading my thesis.

I am very grateful to all the co-authors of my publications – Jens, Davy, Csaba, Elena, Moritz and Vittoria – for their help with my projects. Thanks a lot to Stefano, Claire, Elena and whoever might still come for giving me the chance to support you in your projects and publications.

I thank all my colleagues – or better friends – who made my stay at the University of Basel such an awesome experience. It was a pleasure to work and spend time with you Christoph, Maryame, Csaba, Moritz, Stefano, John, Davy, Alessandro, Dalila, Sven (and his wife Diana, who actually introduced me to this group), Jens, Maria, Vittoria, Saziye, Serena, Dimitri, Dalin, Phally, Elena, Claire, Lukas, Adi, Myrto, Michał, Katrin, Sarah-Luise, Dănuţ, Daniel, Shabnam, Andrea, Luisa, Martina, Sagana, Ioana, Jenny, Charline, Alain, Cora, Pascal and all the others that I met and could spend time with.

I acknowledge all members of the University of Basel who helped in research, administration, IT, from the workshop and infrastructure team, especially Dr. Markus Dürrenberger, Susanne Erpel, Michael Krämer from pss, Prof. Daniel Häussinger, Carola Alampi, Dr. Mike Devereux, Maya Greuter, Mariella Schneiter, Markus Hauri, Susanne Foley, Markus Ast, Pascal Andrek, Hisni Meha and Andreas Sohler.

I thank my old friends Simon, Armin and Marcel for the company during my studies in Mainz and Basel, but also all other friends who contributed immensely to my life, as well as my firefighting colleagues from Mainz and Lörrach.

Last and definitely not least: A huge thank you to my whole family: my grandma Hilde, my aunt Birgit, my aunt Ruth, my uncle Mike, my cousin Louisa, my sister Jessica, but especially my parents Anne and Bruno for their support and help.

The four years of my PhD were an awesome time; I learned many valuable skills for my personal and professional development and gained many new friends and awesome memories. I am grateful for everything and everyone I met during my stay at the University of Basel.

List of frequently used abbreviations

AROP	anionic ring-opening polymerisation
at/*it*/*st*	atactic/isotactic/syndiotactic
BCP	block copolymer
(*R*/*S*)-BCP/(*R*)-BCP/(*S*)-BCP	(*R*/*S*)-PBO_{26}-*b*-(*R*/*S*)-PG_{14}/(*R*)-PBO_{26}-*b*-(*R*)-PG_{14}/(*S*)-PBO_{27}-*b*-(*S*)-PG_{14}
BO	1,2-butylene oxide
CD	circular dichroism
CDSA	crystallisation-driven self-assembly
CLSM	confocal laser scanning microscopy
CROP	cationic ring-opening polymerisation
Cryo-TEM	cryogenic transmission electron microscopy
DLS	dynamic light scattering
DP	degree of polymerisation
DPPC	(*R*)-dipalmitoylphosphatidylcholine
DSC	differential scanning calorimetry
D_3	hexamethylcyclotrisiloxane
Đ	dispersity
EEGE	1-ethoxyethyl glycidyl ether
f	hydrophilic mass ratio
GPC	gel permeation chromatography
GUV	giant unilamellar vesicle
ITC	isothermal titration calorimetry
KNaph	potassium naphthalenide
KO^tBu	potassium *tert*-butylate
l_m	membrane thickness

L-Ala	L-alanine
L-Cys	L-cysteine
L-Ser	L-serine
MOXA	2-methyl-2-oxazoline
M_n	number-average molecular weight
M_w	weight-average molecular weight
NMR	nuclear magnetic resonance
NTA	nanoparticle tracking analysis
OmpF	Outer membrane protein F
PBO	poly(butylene oxide)
PBS	phosphate-buffered saline
PDI	polydispersity index
PDMS	poly(dimethyl siloxane)
PEEGE	poly(1-ethoxyethyl glycidyl ether)
PEG	poly(ethylene glycol)
PEO	poly(ethylene oxide)
PG	poly(glycidol)
PLA/PLLA	poly(lactic acid)/poly(L-lactid acid)
PMOXA	poly(2-methyl-2-oxazoline)
POPC	(*R*)-palmitoyloleoylphosphatidylcholine
PP	poly(propylene)
PPO	poly(propylene oxide)
QCM-D	Quartz Crystal Microbalance with Dissipation monitoring
R_{coil}	end-to-end distance in coil-like conformation
$R_{contour}$	contour length in stretched conformation
R_h	hydrodynamic radius

R_g	radius of gyration
SLS	static light scattering
SUV	small unilamellar vesicle
TEA	triethylamine
TEM	transmission electron microscopy
TGA	thermogravimetric analysis
T_g	glass transition temperature
Δf	change in resonance frequency of the QCM-D sensor
ΔD	change in dissipation
ρ	particle scattering factor

1. Introduction

Parts of the text of this chapter are adapted and modified from:

"Polymer membranes as templates for bio-applications ranging from artificial cells to active surfaces" by Martina Garni, Riccardo Wehr, Saziye Yorulmaz Avsar, Christoph John, Cornelia Palivan and Wolfgang Meier, published in *European Polymer Journal*, **2019**, 112, 346-364. Copyright Elsevier (2019).

1.1. Synthesis of amphiphilic BCPs

1.1.1. General synthetic concepts for BCPs

Amphiphilic BCPs are commonly synthesised through a variety of methods based on the commonly used chain-growth polymerisation techniques such as controlled radical polymerisation (ATRP, RAFT), ionic (ring-opening) polymerisation and combinations thereof. More details about the general synthesis of BCPs can be found in common literature.[1–3] In general, two strategies to form BCPs are possible: *i*) chain-extension of a homopolymer, which then serves as macro-initiator for the sequential addition of a subsequent monomer, or *ii*) click reactions to couple two or more end-functionalised homopolymers.[4]

i) Sequential chain extension reactions for the formation of BCPs benefit from the easily adjustable block lengths and ratios by terminating the polymerisation of the chain-extending blocks when the desired degree of polymerisation (DP) is reached. The chain-extension can be performed either in a two-pot reaction by terminating, purifying and reinitiating the first block, or by an one-pot reaction, *i.e.* immediate addition of a second monomer after full conversion of the first block.[5,6] If the polymerisation of the first block is terminated, a high re-initiation rate is required to suppress the remaining of homopolymer. Also the combination of different polymerisation techniques such as radical and ionic polymerisation is possible after re-initiation of specifically terminated or end-group modified homopolymers.[7]

ii) Coupling reactions such as Diels-Alder, copper-catalysed azide-alkyne cycloaddition (CuAAC) or thiol-ene reactions often require high temperatures or metal catalysts, which hamper biomedical applications.[8,9] Copper-free click reactions such as strain-promoted alkyne-azide cycloadditions (SPAAC) are beneficial in this sense.[10] As the removal of non-reacted homopolymer is usually

challenging, click reactions should be quantitative, requiring complete end-group functionalisation and equimolar ratios of both homopolymers. Steric hindrance of the coiled structure can prevent a quick and quantitative reaction, leading to the remaining of undesired homopolymer. On the other hand, the properties of the BCP after click reaction such as molecular weight, dispersity and block ratio are easily predictable if the properties of the homopolymer precursors are known.

1.1.2. Living ionic polymerisations

Living polymerisations are the gold standard to obtain narrowly distributed polymers with controlled molecular weights.[11–13] According to IUPAC, a living polymerisation is "a chain polymerization from which chain transfer and chain termination are absent. In many cases, the rate of chain initiation is fast compared with the rate of chain propagation, so that the number of kinetic-chain carriers is essentially constant throughout the polymerization".[14] This definition includes an effectively parallel initiation of all polymer chains as well as a constant growth of all chains until the reaction is quenched or all monomer has been consumed. The absence of termination reactions results in active chain ends that continue growing when a second monomer is added. The degree of polymerisation (DP) is given as

$$\mathrm{DP} = \frac{[M]_0}{[I]} \tag{1}$$

with $[M]_0$ = monomer concentration at time 0 and $[I]$ initiator concentration at time 0.[1] Characteristic for such a polymerisation is a linear increase of $\ln([M]_0/[M]_t)$ with the reaction time t ($[M]_t$ = monomer concentration at time t).[15] The dispersity ($Đ$) of a polymer is defined as the quotient of weight-average molecular weight (M_w) and number-average molecular weight (M_n):[15]

$$Đ = \frac{M_w}{M_n} \tag{2}$$

A prominent example for living polymerisations are ionic polymerisations, as they usually fullfil the above mentioned criteria. Ionic polymerisations can be categorised into cationic or anionic polymerisations, starting from linear or cyclic monomers. The latter ones are referred to as cationic or anionic ring-opening polymerisation (CROP/AROP) and allow for the synthesis of hydrophilic polymers such as PEG and poly(oxazolines) and hydrophobic polymers such as poly(siloxanes) and poly(caprolactones).[1,16]

Challenging is their extreme sensitivity to water, oxygen, carbondioxide or protic chemicals, as termination reactions can easily occur. Hence, it is crucial to use inert conditions with extensively dried glassware, absolute aprotic solvents and highly pure and dry chemicals. Polar solvents such as

ethylacetate, THF or dioxane in combination with large counterions such as potassium for AROP are favourable. This leads to a better solvation of the counterion and a free growing chain end and thus to accelerated reaction kinetics.[1,15]

1.1.3. Microwave-assisted synthesis

Microwave-based syntheses are an alternative to the conventional reactions performed in oil baths.[17,18] In a lab microwave, reaction mixtures are heated by microwave irradiation and the temperature is sensed with an infrared (IR) sensor. In general, microwave-assisted reactions have several advantages, but also some drawbacks compared to the oil bath-based reactions. Most importantly, the heating efficiency is enhanced as microwave irradiation penetrates the whole sample directly; hence, it is independent of inhomogeneous heat flux through the oil, glassware and reaction mixture. Additionally, the temperature control is more accurate as the IR sensor measures the temperature directly inside the vessel and not in the oil surrounding the conventional flask. The heating and cooling occurs comparably quickly so that a high control and reproducibility is achieved.[18] As the vessel is tightly closed, even overpressure reactions are possible by heating above the boiling point of compounds. Thus, higher temperatures can lead to significantly reduced reaction times. As a practical aspect, the reaction mixtures can be prepared in a glovebox.[6,19] Nonetheless, subsequent addition of reactants is still possible through the septum in the lid. In this regard, a time-consuming cleaning and drying of the glassware using a Schlenk line is redundant, especially as all consumables are disposable.

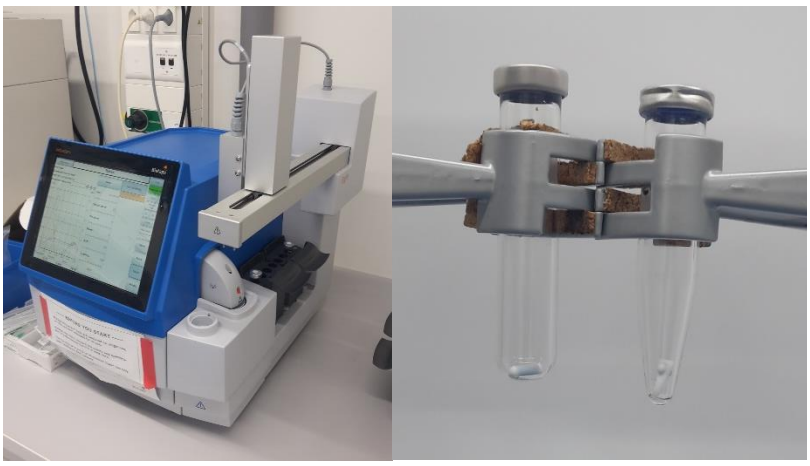

Figure 1: Photograph of the lab microwave employed for the present work (left picture). Exemplary microwave vessels (right picture): a 5 mL vessel on the left, a 2 mL vessel on the right.

On the other hand, the batch size is limited, as the microwave furnace can only host vessels of maximum 20 mL (for the microwave system employed in this work). In particular, when using large vessels, the heat flux can be negatively influenced.[20] An immediate reaction start is also impossible, particularly

after addition of liquid reactants through the septum, as the vessels need to be inserted and the system started before the heating begins. This delay of several seconds could lead to decomposition or a loss of the living character of polymerisations, if the reaction initialises itself already at room temperature.

1.2. Chirality

1.2.1. Chirality in biology and chemistry

Chirality is a main driving force for uncountable biological processes, where protein binding, transport, metabolism or clearance strongly depend on the stereochemistry of substrates.[21] For example carbohydrates naturally occur preferably in their D configuration, whereas aminoacids only occur in their L configuration. Some macroscopic properties such as smell and taste depend on the chirality of a compound, for example in case of (+)-carvone, which smells caraway-like and (−)-carvone which smells spearmint-like.[22] Consequently, different enantiomers of the same drugs can have different effects on organisms, as one enantiomer delivers the desired theropeutic activity, whereas its counterpart exhibits a potentially toxic effect.[23] In addition, the phospholipids forming the cell membrane are intrinsically chiral, as they exhibit one asymmetric carbon atom.[24] Stereocontrol in polymers can be achieved by introducing chirality in the side groups of the repeating units, for example by using monomers exhibiting a chiral moiety that remains unchanged when polymerised. Alternatively, chirality can be introduced in the polymer backbone itself, referred to as tacticity if every repeating unit bears a stereoregular side group. This approach is particularly interesting in the material sciences, as mechanical and thermal properties of plastics such as rigidity, stability and melting are affected by variations in the tacticity, allowing for a fine-tuning of these macroscopic properties depending on the desired applications (see following section).

1.2.2. Tacticity of polymers

Tacticity describes the configuration of subsequent repeating units on a polymer backbone. In this regard, atactic polymers do not possess any stereoregularity and a random configuration from one repeating unit to an adjacent one is present. Isotactic polymers in contrast possess a similar configuration on every repeating unit, whereas syndiotactic polymers exhibit an alternating configuration (Figure 2).

In order to quantify the isotactic content of polymers, diad tacticity has been introduced.[1] Hence, a meso diad (*m*) corresponds to two adjacent repeating units which are isotactic to each other. A racemic diad (*r*) corresponds to two adjacent repeating units syndiotactic to each other (Figure 2). The sum of *m* and *r* is defined as 1, meaning that a fully isotactic polymer corresponds to $m = 1$, a fully syndiotactic polymer to $m = 0$ and a perfectly atactic polymer to $m = 0.5$. Usually, because of synthetic deviations, isotactic polymers do not consist entirely of isotactic conjunctions. Generally, polymers with $m > 0.9$ are referred to as isotactic.[16]

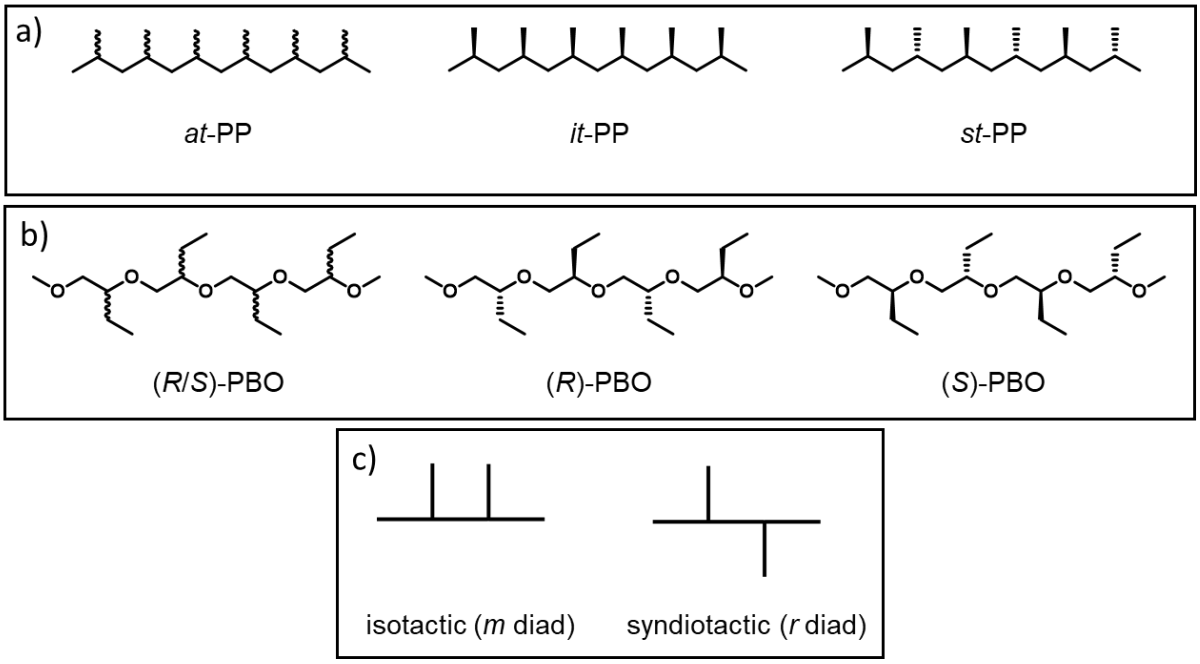

Figure 2: a) Chemical structures of atactic poly(propylene) (*at*-PP), isotactic poly(propylene) (*it*-PP) and syndiotactic poly(propylene) (*st*-PP). b) Chemical structures of atactic (*R*/*S*)-PBO, isotactic (*R*)-PBO and isotactic (*S*)-PBO. c) Schematic representation of an isotactic conjunction, forming an *m* diad, and a syndiotactic conjunction, forming an *r* diad.

The introduction of stereoregularity within the polymer backbone leads to changes in their mechanical and thermal properties. Atactic polymers are typically amorphous and of limited physical strength. Stereoregular polymers however, *i.e.* syndio- or isotactic polymers, exhibit a higher order and tend to crystallise. This (semi-) crystallinity leads to a higher physical strength, increased solvent and chemical resistance and different thermal behaviour.[1] Isotactic polypropylene (*it*-PP) for example is a rigid, crystalline polymer used industrially as plastic, whereas atactic polypropylene (*at*-PP) is soft and waxy and of little industrial relevance. The glass transition temperatures of *it*-PP (–18 °C) are about 10 °C lower than the ones of *at*-PP (–6 °C).[25] It should be noted that first order transitions (melting, crystallisation) occur only if crystalline parts are present. Second order transitions (glass transitions) are present for all polymers that (partly) exhibit amorphous character, but are the only thermal transitions observed for fully amorphous polymers.[1]

In contrast to small chiral molecules possessing one stereocentre, isotactic polymers are not necessarily optically active. The optical activity, *i.e.* the ability of compounds to rotate polarised light, is a result of the presence of asymmetrically substituted ("chiral") atoms. In case of *it*-PP for example, only a pseudo-asymmetry of a backbone carbon atom is observed, as the difference of the two substituting polymer chains growing in both directions is negligible for long chains. Hence, the chains are similar in close proximity and no optical activity is observed.[16] In contrast, if an effective asymmetry is present, as for example in polyethers or polyesters, optical activity is observed (Figure 2). Only for those polymers the (+) and (–) annotation of optical activity or the Cahn-Ingold-Prelog (CIP) prioritisation into (*R*) or (*S*) isotactic polymers is feasible. The absence of stereoregularity in these polymers, *i.e.* the presence of atactic (*R*/*S*) polymers, does not result in optical activity, as the effects of (*R*) and (*S*) stereocentres within the backbone cancel out over the whole chain.

1.2.3. Chiral interaction

The above-mentioned different effects between enantiomers on organisms such as smell, taste and therapeutic activity are the result of chiral recognition mechanisms.[26–28] Similar effects can be employed in chemical applications. In the field of synthetic chemsitry stereocontrolled syntheses are possible by using chiral metal-based catalysts. These catalysts allow for the a directed spatial attack of reactants and thus enable the formation of stereocontrolled products.[27,28] In a similar manner, the synthesis of syndio- or isotactic polymers is possible.[29,30] A typical example thereof is the synthesis of *it*-PP or *st*-PP by Ziegler-Natter catalysts.[16] Also molecular imprinted micelles allow for the stereoselective recognition and separation of racemic mixtures of small compounds.[31] In chiral high performance liquid chromatography (HPLC) the enantioselective elution of chiral compounds is achieved by using chiral stationary phases (CSPs). These CSPs are commonly based on polymers bearing chiral side groups.[32–34] Additionally, nanoparticles composed of poly(amino acids) can be employed for enantioselective crystallisation, where L-amino acids were shown to preferably adsorb on poly(L-amino acid) nanoparticles.[35,36] In contrast to polymers bearing chiral side groups, no reports about chiral interaction solely based on the tacticity of polymers are known.

A powerful physico-chemical method to prove chiral interaction is isothermal titration calorimetry (ITC).[36–38] There, the heat development during binding of one compound to another is detected and allows for the calculation of binding constants. Alternatively, surface-sensitive methods such as quartz crystal microbalance with dissipation monitoring (QCM-D) and surface plasmon resonance (SPR) can be employed to calculate the mass adsorption of compounds on functionalised solid substrates.[39–42] By adsorption or desorption of analytes on the sensor, these methods reveal information of the compound-surface specific interactions, *e.g.* binding forces, crosslinking, (de)coupling and etching. The working

principle of QCM-D, being of particular interest for the present work, will be explained in more detail below.

QCM-D allows for real-time monitoring of mass changes within the ng range and layer thicknesses in the nm range of substances adsorbing on solid support. The resonance frequency of an oscillating quartz crystal changes depending on the mass adsorbed on the sensor.[43] For homogenous, thin and rigid films deposited on the QCM sensor the adsorbed wet mass Δm can be calculated using the Sauerbrey equation from the change in the resonance frequency Δf:

$$\Delta m = -C\frac{\Delta f}{n} \tag{5}$$

with C being the mass sensitivity constant and n the number of the uneven harmonic.[44] A decrease of frequency thus corresponds to a mass adsorption. If for example vesicles adsorb on the QCM-D sensor, the frequency will not only decrease due to the weight of the membrane-forming BCPs but also due to the entrapped water. Consequently, the rupture of the vesicle will decrease the mass and increase the frequency as this water is being released.[45] The Sauerbrey conditions are not matched for adsorbed vesicles as the layer is neither sufficiently homogenous nor rigid. In this case, sophisticated multivariant models can be applied to calculate the adsorbed mass or layer thickness.[40,46] The dissipation provides information about the viscoelastic properties of the adsorbents, *i.e*. the energy loss during oscillation. The higher the dissipation, the more elastic or viscous is the adsorbent. In this regard, vesicles show high dissipations because of their flexible nature.[40,46,47]

1.3. Aqueous self-assembly of amphiphilic block copolymers

1.3.1. Lipids and their synthetic analogues: amphiphilic BCPs

In biological systems, lipids play an essential role as building blocks of cell membranes.[48,49] They exhibit an amphiphilic character, meaning they consist of a polar, hydrophilic head group, and an apolar, hydrophobic tail. In case of phospholipids, the main component of cell membranes, a phosphate ester represents the polar head, whereas the apolar tail consists of long aliphatic carbon chains. The amphiphilicity of lipids leads an assembly of lipid molecules into nano- and macroscopic structures in order to protect the hydrophobic part from the aqueous surrounding. Hydrophobic, non-covalent interactions of the lipid carbon chains stabilise the membrane, which is surrounded by the hydrophilic head groups on the interphase to the aqueous medium. Thus, a bilayer is formed, separating the aqueous lumen of the cell from the surrounding. While the membrane forming lipids provide stability and a

barrier against cytotoxic substances, several additional molecules such as transmembrane or peripheral proteins enable specific functions such as sensing, transport or signalling.[24]

Lipid-based nano- or micrometre sized (synthetic) vesicles are referred to as liposomes.[50] They are similarly built of lipid bilayer membranes and usually do not contain any other cell ingredients such as membrane proteins. However, they can be equipped with these, serving as cell mimics or nano- or microreactors. In addition, the formation of spherical lipid micelles is possible, resembling surfactant micelles with an inner hydrophobic core. In this case, no bilayer membrane is formed. Recently, such lipid-based nanoparticles have gained public attention as carriers for the Covid-19 vaccines.[51]

Amphiphilic BCPs represent fully synthetic analogues to lipids.[52,53] They consist of a hydrophobic domain, build up by a hydrophobic polymer block and a hydrophilic domain which is in contrast to lipids not formed by a polar head group, but by a second, hydrophilic polymeric block. Amphiphilic BCPs exhibit similar behaviour in aqueous media as lipids as they self-assemble into – amongst others – spherical micelles, wormlike structures or hollow spheres. The latter ones are in analogy to liposomes referred to as polymersomes, whose sizes vary in the nanometre (small unilamellar vesicles, SUVs) or micrometre range (giant unilamellar vesicles, GUVs). In general, not only linear diblock copolymer architectures can be employed. Various different architectures ranging from linear tri-or multiblock over brushlike copolymers up to dendrimers have also been reported to self-assemble in aqueous media.[54–56] This work will focus on linear diblock copolymer architectures.

1.3.2. Polymer membranes versus lipid membranes

Generally, lipids form thin membranes with thicknesses below 5 nm, resulting from their small size and low molecular weight. Polymeric membranes, in contrast, are composed of BCPs with usually significantly higher molecular weights and increased chain lengths, resulting in thicker membranes commonly between 5 and 30 nm (Figure 3).[57,58] The increased thickness, in turn, leads to a decreased permeabilisation for substrates. Additionally, the reconstitution of membrane proteins is challenging, as a high size mismatch between membrane pore size and membrane thickness needs to be compensated.[59] On the other hand, the higher membrane thickness of polymer membranes and chain entanglements lead to an increased mechanical stability.[52,60] In addition, the chemical versatility of the membrane forming BCPs offers multiple ways of functionalisation. By selecting the appropriate BCP composition, the desired functional groups can be included either as end groups on the hydrophilic or hydrophobic chain end or as functional repeating units in both blocks. Thus, cross-linking to further enhance the stability can be achieved, as well as the incorporation of functional groups for example for labelling or signalling purposes or cluster formation.[61–66] Stimuli-responsive BCPs even allow the

triggering of specific functions like morphological changes, size adjustments or release of cargo. To conclude, polymer membranes benefit from their high stability and versatility, whereas the permeability is reduced due to their increased thickness.[67]

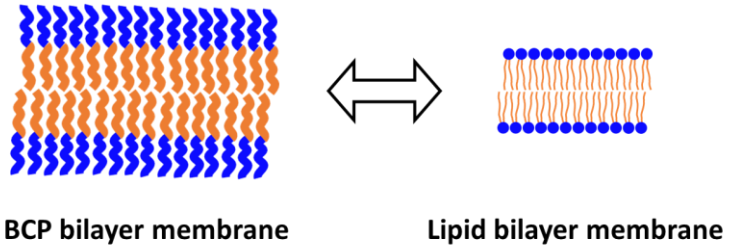

Figure 3: Schematic representation of a bilayer membrane formed by an amphiphilic diblock copolymer in comparison to a lipid bilayer membrane. Possible entanglements of the BCP chains are not displayed in this sketch. The blue colour represents the hydrophilic domains and the orange colour represents the hydrophobic domains.

1.3.3. Polymer requirements and potential self-assembly candidates

The choice of suitable polymers for self-assembly depends on the target application. In general, there are no limitations regarding the polymer composition as long as the BCP is able to self-assemble into the desired structure (Figure 4). Naturally, polymers are favourable which allow an easy, quick and well-controlled synthesis to enable reproducibility. For biomedical applications like drug delivery (section 1.3.8) the BCP has to be non-toxic and biocompatible. In order to guarantee biological harmlessness, its synthesis should ideally avoid toxic and hard-to-remove compounds such as metal catalysts. Biodegradability is favourable if a controlled decomposition is desired. Examples of biocompatible and -degradable polymers are polyesters like poly(lactic acid) (PLA) or poly(caprolactone) (PCL).[68] Those polymers often exhibit high glass transition temperatures (T_g) and (semi-) crystalline behaviour; hence, high temperatures or thorough dissolution in an organic solvent are essential to create well-defined self-assemblies.[69–71] Those BCPs lead to stiff and inflexible membranes, which increases the stability but prevents applications requiring high membrane flexibility and fluidity. BCPs that allow self-assembly in moderate conditions (room temperature and organic solvent free) are especially favourable if temperature-sensitive compounds like enzymes should be encapsulated or membrane pores should be incorporated.[59,69,72] In this regard, the use of amorphous polymers with a T_g below room temperature is advantageous. Additionally, depending on the application of the self-assemblies, polymers with specific properties such as stimuli-responsiveness can be employed. Typical examples are, amongst others, temperature-sensitivity as in poly(glycerol monomethacrylate-)-*block*-poly(2-hydroxypropyl methacrylate) (PGMA-*b*-PHPMA)[73] or pH-sensitivity as in poly(ethylene glycol)-*block*-poly[2-(diethylamino) ethyl methacrylate] (PEG-*b*-PDEAEMA).[74] Applying a respective stimulus can lead to morphological changes or controlled release

of cargo.[53,75] A compilation of for this work important hydrophilic and hydrophobic polymers is presented below (Figure 4).

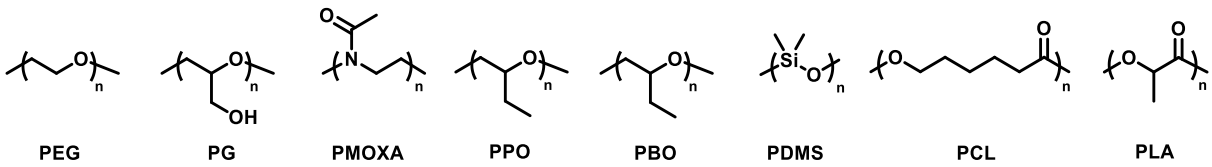

Figure 4: Chemical structures of some of the common polymers for aqueous self-assembly: poly(ethylene glycol) (PEG), poly(glycidol) (PG), poly(2-methyl-2-oxazoline) (PMOXA), poly(propylene oxide) (PPO), poly(butylene oxide) (PBO), poly(dimethyl siloxane) (PDMS), poly(caprolactone) (PCL) and poly(lactic acid) (PLA).

1.3.3.1. Poly(ethylene oxide) (PEO)/Poly(ethylene glycol) (PEG)

PEO and PEG designate the same polymer.[5,76] The name PEO is prevalent in industrial applications and cites the actual monomer ethylene oxide (EO), whereas the denotation PEG is more prevalent in the biomedical field or for shorter polymer chains. PEG represents the simplest hydrophilic polyether. It benefits from a high biocompatibility and a low T_g of about –40 °C but exhibits also crystalline behaviour.[19,77] The so-called PEGylation, the conjugation of drugs with PEG, enables a stealth effect and prevents a decomposition of the drug in the blood stream.[78–81] Thus, the protein adsorption is reduced, leading to a higher drug efficacy. PEG is not only the gold standard in the biomedical field, also in industrial and consumer applications it is widely spread. PEG is FDA approved and an ingredient of food products and cosmetics. In particular, di- and triblock copolymers containing PEG and poly(propylene oxide) (PPO) (PEG-*b*-PPO and PEG-*b*-PPO-*b*-PEG) are well-known as poloxameres or pluronics® and used as emulsion stabilisers and surfactants.[5,82] As a hydrophilic block in amphiphilic BCPs, it has been extensively used.[6,69,71] However, PEG suffers from some drawbacks. Regarding the use in biological environments, it is not biodegradable and tends to accumulated within the organism and an immune response by anti-PEG antibodies is possible.[83–85] In addition, it can induce complement activation in human sera, suffer from accelerated blood clearance when injected repetitively and possesses a risk of peroxidation.[86–88] From a synthetic perspective, the absence of functional groups on the repeating units prevents a functionalisation except on the chain ends (Figure 5a). The dangerous synthesis starting from highly toxic gaseous EO is dangerous at a lab scale, although well controlled. Hence, PEG alternatives have been suggested, which aim to overcome at least some of the disadvantages.[76,89,90]

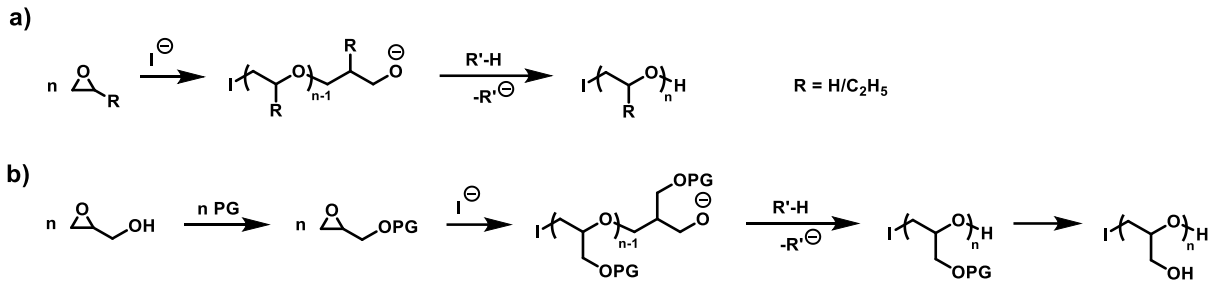

Figure 5: a) Reaction equation for the synthesis of PEG (for R = H) and PBO (for R = C_2H_5) *via* AROP. b) Reaction equation for the synthesis of poly(glycidol) *via* AROP. The first step includes the protection of the hydroxy moiety with a protecting group (PG), the last step the cleavage thereof.

1.3.3.2. Poly(glycidol) (PG)

As an alternative hydrophilic block to PEG, poly(glycidol) (PG) has gained increasing interest.[91,92] PG is structurally similar to PEG, but more hydrophilic and can be further functionalised because of the additional hydroxymethyl moieties on every repeating unit. Its synthesis starts from the AROP of easy-to-handle protected glycidol derivatives like 1-ethoxy ethyl glycidyl ether (EEGE), *tert*. butyl glycidyl ether (*t*BGE) or allyl glycidyl ether (AGE).[91] The protection prevents unintended branching from the hydroxy side groups. Acidic cleavage of the protecting groups after polymerisation eventually leads to linear PG (Figure 5b).[93,94] PG has already shown its potential as PEG alternative in several self-assembly applications.[95–101] It is equally biocompatible and exhibits a reduced protein adsorption compared to PEG.[95,102–104]

1.3.3.3. Poly(2-methyl-2-oxazoline) (PMOXA)

Poly(2-methyl-2-oxazoline) (PMOXA) as a hydrophilic polymer is considered as another alternative to PEG.[89,105,106] PMOXA is biocompatible and shows a stealth effect similar to PEG. Especially in combination with PDMS, it has shown great potential in aqueous self-assemblies.[6,69,107–109] PMOXA is commonly synthesised *via* CROP starting from triflates, nosylates or tosylates as initiators.[110–112] No lower critical solution temperature (LCST) is observed for PMOXA, meaning it is soluble at any temperature in aqueous medium and in bulk even hygroscopic.[89] The hydrophilicity of poly(oxazolines) decreases drastically if the methyl group is replaced by longer aliphatic chains. Whereas poly(2-ethyl-2-oxazoline) (PEtOX) is still hydrophilic with a lower critical solution temperature (LCST) of 60-70 °C, the longer analogues from poly(2-propyl-2-oxazoline) on are fully hydrophobic.[106]

1.3.3.4. Poly(butylene oxide) (PBO)

Poly(butylene oxide) (PBO) as a hydrophobic polyether shares the same backbone as PEG and PG. Especially its low T_g of –70 °C[113] enables applications where high membrane fluidity and flexibility are required. Compared to PPO, PBO exhibits a higher hydrophobicity, is totally amorphous and easier to synthesise at a lab scale due to the higher boiling point of the monomer BO.[113–115] PBO is commonly synthesised in an AROP starting from BO monomer (Figure 5a).[95] Several studies employed PBO in aqueous self-assemblies and highlighted the high biocompatibility of PBO containing nanoparticles.[95,116–119]

1.3.3.5. Poly(dimethyl siloxane) (PDMS)

Poly(dimethyl siloxane) is a highly hydrophobic polymer. It is extremely flexible with a low T_g of only –125 °C.[120,121] The flexibility originates from the Si-O bonds with a length of 1.65 Å and arranged in a bond angle of 142.5° (Si-O-Si) or 109° (O-Si-O), respectively.[122] It is biocompatible and has been used extensively for aqueous self-assembly applications both for the formation of SUVs and GUVs.[123] Especially for the insertion of membrane proteins to create nanoreactors or cell mimics PDMS is predestined due to its high flexibility, low T_g and amorphous character.[107–109,124,125] PDMS is commonly synthesised in an AROP starting from the cyclic monomers hexamethyl cyclotrisiloxane (D_3) or octamethyl cyclotretrasiloxane (D_4).[126–128] Recently studies of the synthesis and properties of discrete PDMS with $Đ < 1.00002$ have been published.[129,130] However, this polymer has not been subjected to aqueous self-assembly yet.

1.3.4. Self-assembly morphologies

Similar to lipids, amphiphilic BCPs undergo self-assembly in aqueous media to prevent the hydrophobic block from interaction with the surrounding water. The hydrophilic block serves as stabiliser and enables the formation of thermodynamically or kinetically stabilised structures in the nano- or micrometre range.[53,67] Depending on various factors, different nanoscopic morphologies are possible. The most common ones are spherical micelles, cylindrical micelles (worms) and vesicles (polymersomes) (Figure 6). The latter ones are composed of a symmetric bilayer membrane (in case of diblock copolymers) and enclose an aqueous cavity. In this work, nanoscopic vesicles are referred to as Small Unilamellar Vesicles (SUVs). On a microscale, so-called Giant Unilamellar Vesicles (GUVs) can be obtained. Besides the above mentioned morphologies, also more sophisticated structures like multicompartment vesicles (MCMs), gyroidal or lamellar assemblies have been reported.[19,131,132]

Several different factors and their interplay govern the morphology and size of the self-assemblies: the nature of the BCP (chemical composition,[133] dispersity,[134,135] hydrophilic mass ratio *f*)[136] external conditions such as BCP concentration,[137] temperature and pH,[138] salt content[136] and finally the preparation method.[19,111] The dispersity, *f*-ratio and the different formation methods, being of particular interest for the present work, are discussed in detail below.

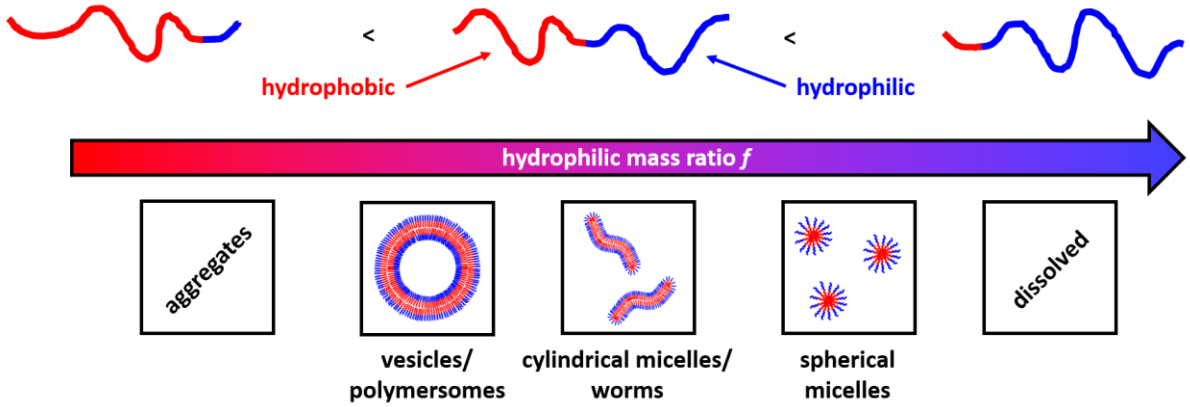

Figure 6: Effect of an increasing hydrophilic mass fraction *f* of an amphiphilic BCP on the self-assembly morphologies in aqueous medium.

1.3.4.1. Dispersity

Theoretical studies suggest that a certain dispersity in the BCP leads to a segregation of polymer between the inner and outer layer of the vesicle membrane: shorter chains favour the assembly at the inner monolayer, while longer ones preferably cover the outside of the vesicle and thus support the curvature of the membrane.[134,139] In this regard, the formation of well-defined self-assemblies such as vesicles was possible using BCPs with relatively high dispersities of up to 2.[136] Recent studies compared the self-assembly formation of discrete ($Đ$ = 1.00) and disperse ($Đ$ = 1.01-1.06) PLA-*b*-PEG BCPs.[71] For spherical micelles and worms no differences was found. For vesicles a reduced reproducibility was observed when using disperse hydrophobic blocks. The general morphology however was not affected. Thus, the effect of dispersity remains unclear and seems to depend on the specific system employed.

1.3.4.2. Hydrophilic mass ratio *f*

The hydrophilic mass ratio *f* (*f*-ratio) is calculated by the molecular weight of the hydrophilic block ($M_{\text{hydrophilic}}$) divided by the total molecular weight of the BCP (M_{BCP}).

$$f = \frac{M_{\text{hydrophilic}}}{M_{\text{BCP}}} \quad (3)$$

Besides the formation method and the dispersity, it is one factor that governs the morphology of the self-assemblies.[140–142] *f*-ratios between 25% and 40% are generally considered to lead to the formation of vesicles.[60,136,143–145] Increasing the *f*-ratio to values up to 50% leads to the formation of cylindrical micelles (worms). Even higher values favour the formation of spherical micelles (Figure 6). This consideration does not take sophisticated structures such as tubes, MCMs or other intermediate structures into account.[19] Hence, the above-mentioned values should be rather seen as rule of thumb and are not sufficient to predict a certain morphology. Once the *f*-ratio falls below a critical value, the hydrophilic block is no longer able to stabilise a well-defined structure, resulting in aggregates. On the contrary, if the *f*-ratio exceeds a certain value, the BCP chains are molecularly dissolved as the hydrophobic interactions are too weak to stabilise a membrane.

1.3.5. Self-assembly formation

Besides the dispersity and *f*-ratio, the final morphology of self-assemblies is strongly dependent on the formation method. The same BCP can exhibit various structures depending on their formation method, differing in morphology, sizes, uniformity or reproducibility.[19] Deciding for the right method to obtain the desired morphologies is not straight-forward and requires systematic studies and tests. Certain considerations, however, help to narrow down possible approaches. Crystalline polymers or polymers below their T_g require thorough dissolution in an organic solvent or high temperatures, whereas sensitive cargo or membrane proteins are incompatible with those conditions.[69,70,72] Some of the most common methods are explained below.

1.3.5.1. Nanoscale self-assembly

Nanoscopic self-assemblies can be formed by a variety of different techniques.[52,143,146] The two methods employed in this work are described in the following and in Figure 7.

Film rehydration. A BCP is deposited as a thin film in a flask or vial by slowly evaporating an organic solvent that dissolves both blocks. This film, in turn, is subsequently rehydrated with the aqueous medium. A high shear rate induced by stirring or ultrasound supports the hydration process. In this top-down approach, the energy provided by stirring or ultrasound is considered to lead to the formation of kinetically trapped morphologies rather than structures in their thermodynamic equilibrium.[143]

Solvent exchange. Solvent exchange, in contrast to film rehydration, is a bottom-up approach where the BCP is dissolved in a small volume of an organic solvent that dissolves both blocks and that is miscible with water. Subsequently, an excess of aqueous medium is added slowly by a syringe pump under moderate stirring. Ultimately, the organic solvents can be removed by dialysis, ultrafiltration, centrifugation or evaporation. The self-assembly of the BCP chains, induced by the increasing insolubility, favours the formation of rather thermodynamically stabilised nanoparticles.[19]

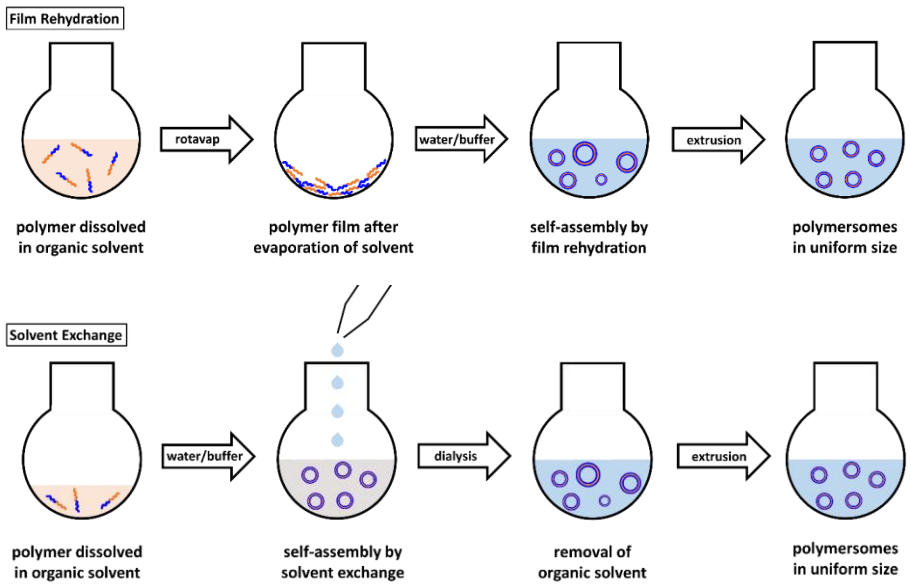

Figure 7: Schematic representation of the aqueous self-assembly formation techniques film rehydration (top) and solvent exchange (bottom) and extrusion of the formed SUVs.

Alternatively, self-assemblies can be formed also by direct dissolution, which implies that a BCP is added to an aqueous medium and dispersed by stirring, ultrasound or simply diffusion without external trigger. Additionally, physical triggers such as pH or temperature changes allow for the formation of nanoparticles from stimuli-responsive BCPs.[147,148] Polymerisation-induced self-assembly (PISA) represents a method to synthesise and self-assemble BCPs in a one-pot reaction.[73,149] The latter techniques have no significance for this work and will not be discussed in detail.

Nanoscopic self-assemblies, especially SUVs, typically suffer from high size variations after the formation. In order to narrow down this polydispersity, the dispersions can be extruded using standard extruders for lipids. This leads to smaller particles and narrower size distributions, depending on the pore size of the extruder membrane.[150]

1.3.5.2. GUV formation

GUVs can be formed using different approaches such as electroformation, film rehydration or double emulsion microfluidics.[53,151] When using electroformation, dry BCP films deposited on conductive indium tin oxide (ITO) coated glass slides form GUVs when rehydrated with an aqueous medium in an alternating sine-wave electric current.[152] Film rehydration is based on the same principle as discussed for nanoscopic self-assemblies: a thin BCP film is rehydrated with aqueous medium. In contrast to the nanoscopic self-assembly gentle mixing with low shear forces has to be applied to create microscopic structures.[109] Even more than for SUVs, GUV formation by electroformation and film-rehydration does not produce GUVs with homogeneous sizes. Besides aggregates and multicompartment vesicles, typically a mixture of GUVs in the size range between 1 to and 40 µm is formed. In order to circumvent this drawback, microfluidics has emerged as an advanced tool to create monodisperse GUVs at high throughput.[125,153–157] There, GUVs are produced from water-in-oil-in-water double emulsion droplets. After evaporation of the organic phase, GUVs are obtained. The GUVs formed by microfluidics benefit from their size uniformity, absence of aggregates and high yield. A remaining pocket of non-evaporated organic solvent and dissolved BCP within the membrane is commonly observed.[125]

1.3.6. Self-assembly characterisation

The physico-chemical methods used to characterise aqueous self-assemblies strongly depend on the magnitude of the structures to analyse.[158] Nanoscopic self-assemblies are typically characterised using (light) scattering techniques as well as electron microscopy. Dynamic light scattering (DLS) enables the calculation of the hydrodynamic radius (R_h), whereas static light scattering (SLS) serves to assess the radius of gyration (R_g). By combining of DLS and SLS, the calculation of the so-called particle scattering factor ρ is possible:

$$\rho = \frac{R_g}{R_h} \tag{4}$$

ρ is a measure for the morphology of the formed structure.[159,160] A value of ρ = 1.0 represents an ideal hollow sphere with infinitely thin shell. A full sphere is expected to give ρ = 0.775. Hence, a particle scattering factor of ρ = 1.0 or slightly lower is regarded as ideal for SUVs with a thin membrane. In contrast to DLS, nanoparticle tracking analysis (NTA) provides a more accurate size distribution, as it tracks the diffusion of every particle individually and thus calculates their hydrodynamic radii. Transmission electron microscopy (TEM) allows for the direct imaging of nanoparticles in a dried state. As a result of the vaccuum applied, hollow structures like SUVs usually deflate.[111] Sizes or diameters of SUVs can be estimated, but are inaccurate because of the collapsed nature and staining effects. In contrast, cryogenic transmission electron microscopy (Cryo-TEM) can be employed to measure sizes as well as membrane thicknesses of SUVs as drying and staining artefacts are avoided. There, particles keep ther original morphology as in solution as they are frozen in amorphous ice and are imaged only by direct and natural contrast.[57,152]

Microscopic structures like GUVs can be characterized using methods adapted from cell biology due to their similar sizes. Especially light, fluorescence or confocal laser scanning microscopy (CLSM) are beneficial, as they allow a direct visualisation in transmission or emission mode, respectively.[53]

Various other characterisation techniques for nano- or microparticles can be employed such as fluorescence correlation spectroscopy (FCS),[59,108] atomic force microscopy (AFM),[161] small angle X-ray scattering (SAXS),[162] flow cytometry[163] and zeta potential measurements[164] but are not significant for this thesis and will not be discussed.

1.3.7. Membrane permeabilisation

Lipid membranes are generally semipermeable and the passage of substances through the membrane depends on their size, hydrophobicity and charge. In order to allow a controlled passage of specific substrates for metabolic pathways through cell membranes, they are equipped with membrane proteins.[24,48,49] A similar approach can be employed to generate permeable polymeric membranes, as they are generally even less permeable towards hydrophilic substances than lipid membranes.[67,72] The type of the reconstituted membrane pore determines the substances the pore is permeable for. The Outer membrane protein F (OmpF) allows for example the passage of substrates below 600 Da.[165] Aquaporin Z (AqpZ) enables permeability solely for water,[166] whereas ion channels such as the pore forming peptide gramicidin (gA) allow for a passage of protons and monovalent cations.[167] Recently, the pore forming peptide melittin gained increasing interest as a non-specific channel pore without specific cut-off.[108]

The reconstitution of membrane pores, in particular membrane proteins, is generally challenging as several requirements need to be matched. The expression of membrane proteins like OmpF from bacteria is time consuming and the purification needs to be done shortly before reconstitution to prevent denaturation in aqueous medium without detergent.[168] A low molecular weight of the BCP, leading to relatively thin membranes, is essential to keep the size mismatch between membrane thickness and the significantly smaller membrane pore as small as possible. In this regard, a certain BCP dispersity also supports the arrangement of shorter chains around the membrane pore. The hydrophobic block needs to be fluid and flexible, in order to allow a functional reconstitution of membrane proteins.[59,72]

1.3.8. Applications of aqueous self-assemblies

Aqueous self-assemblies in the nano- or microscale possess various possible applications. In particular vesicular structures (SUVs and GUVs) are extensively used for drug delivery systems, as nanoreactors or cell mimics. These applications are summarised below.

1.3.8.1. Drug delivery

SUVs are of particular interest as drug delivery agents in biomedical applications (Figure 8a). They are able to host hydrophobic drugs within the membrane as well as hydrophilic cargo inside their inner aqueous cavity.[169,170] The encapsulation of drugs leads to a prolongation in the blood stream and prevents a possible degradation. Especially stimuli responsive SUVs enable a controlled release of their cargo by triggering rupture, permeability or morphological changes. Small vesicle sizes enhance the cell uptake, hence diameters below 200 nm are favoured.[171] Loading of SUVs with cargo is commonly done during vesicle formation, where encapsulation efficiencies of up to 67 % could be reached.[172] In case of film rehydration, cargo can be deposited either with the film or added with the aqueous medium during rehydration. The latter method allows for the encapsulation of sensitive cargo that is not compatible with organic solvents. This limitation applies even more for solvent exchange as the vesicle formation there occurs in presence of organic solvent.[173] In addition, a complete removal of the organic solvent cannot be assured unequivocally after solvent exchange, diminishing the potential use of those self-assemblies in organisms.[19]

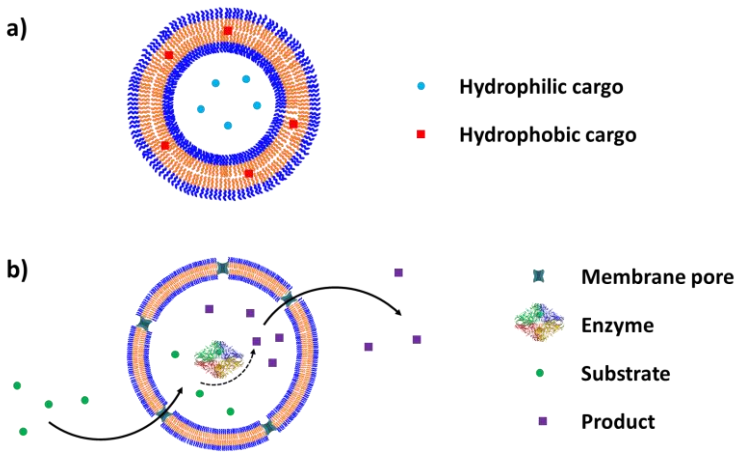

Figure 8: a) Schematic representation of a vesicle employed for drug delivery. Hydrophilic cargo (blue dots) is encapsulated in the lumen of the vesicle, hydrophobic cargo (red squares) is encapsulated in the hydrophobic core of the membrane. b) Schematic representation of a vesicle employed as nano- or microreactor. The substrate (green dots) diffuses through the membrane pore into the vesicle and reacts with the encapsulated enzyme. The product (violet squares) accumulates in the lumen and over time diffuses out of the membrane pores. The sizes of the different compounds are not to scale.

1.3.8.2. Nano-/Microreactors

Nano- or microreactors serve as confined reaction spaces based on SUVs or GUVs with encapsulated enzymes and reconstituted membrane pores (Figure 8b).[53,140] Substrates diffuse through the pores inside the cavity and react there in enzyme reactions. The products accumulate in the cavity and over time diffuse out of the pores. Even cascade reaction involving several sequential reactions in multiple vesicles have been created.[124,125] Nano- and microreactors allow the kinetic analysis of enzyme reactions and the on-demand production of substrates in compartments preventing enzyme degradation. Typical enzyme reactions are for example the reaction of hydrogen peroxide with Amplex Ultra Red (AUR) in presence of the enzyme Horseradish Peroxidase (HRP),[174] forming the fluorescent dye resorufin, or the cleavage of resorufin-D-galactopyranoside (RGP) into resorufin and D-galactose, catalysed by the enzyme β-galactosidase (β-Gal).[175]

1.3.8.3. Cell mimics

Whereas SUVs represent ideal candidates for biomedical applications, GUVs can be used as simplified cell mimics to visualise and imitate biological processes in cells due to their similar sizes. They can be tuned according to desired applications regarding compartmentalisation, composition, function and complexity. For example, membrane proteins allow a controlled passage of substrates, encapsulated SUV or liposomes mimic organelles and polymerised actin represents the cytoskeleton.[109,176–179]

Especially advances in double emulsion microfluidics to create homogenous well-defined GUVs seem advantageous for further cell mimics in increasing complexity as the loading with artificial organelles and substrates is more reproducible than the conventional film rehydration method.[125]

1.3.9. Isotactic block copolymers in aqueous self-assembly applications

Whilst bulk self-assembly of isotactic BCPs is a well-studied field,[180,181] only few examples are reported that involve their aqueous self-assembly. All of them have in common that the formation of nanoparticles was based on crystallisation-driven self-assembly (CDSA). Thus, the stereocontrol of the hydrophobic blocks isotactic polystyrene (*it*-PS) or poly(L-lactic acid) (PLLA) served solely as means to introduce crystallinity within the membrane. Poly(L-lactic acid)-*block*-poly(acrylic acid) (PLLA-*b*-PAA) BCPs formed for example cylindrical micelles, whereas spherical micelles were obtained when atactic PLA was employed.[182–184] The effect of dispersity and crystallinity of PLA-*b*-PEG self-assemblies composed of atactic or isotactic PLA was recently analysed.[71,185,186] However, no differences in the morphology of spherical micelles, cylindrical micelles and SUVs were observed. The sizes of different batches of vesicles were more uniform when PLLA was used; this observation, however, was addressed to the reduced dispersity and not to the crystallinity. Only the packing of chains within the vesicle membrane was affected by crystallinity, as isotactic BCPs occupied a denser and more elongated conformation within the membrane.[71] CDSA of *it*-PS-*b*-PEG BCPs led to the formation of spherical and petal-like micelles in DMF, which transitioned into bowl-like micelles upon dialysis against water.[187] Micellar phases were also formed upon self-assembly of *it*-PS-PBD-*g*-PEO BCPs.[188] In both studies, comparisons to atactic *at*-PS containing BCPs were however missing. Hence, the effect of stereoregularity alone, independently of crystallinity, remains unknown so far.

2. Motivation and Aim

The numerous possible applications as drug delivery agents, as nano- or microreactors or for cell mimics highlight the potential of BCP-based aqueous self-assemblies, especially of SUVs and GUVs. Although extensive research has been performed to find appropriate polymers for the desired biomedical or biotechnological applications, some of the most frequently used ones still exhibit drawbacks: PEG with the rise of anti-PEG antibodies and a possible immune response, PDMS with the challenging synthesis and the lack of reproducibility or (isotactic) PLA, PCL and PPO with their semicrystallinity hindering applications involving sensitive cargo or membrane proteins. Thus, it seems beneficial to establish alternative polymers overcoming these limitations. In this regard, PBO-*b*-PG is a promising alternative as it is biocompatible, amorphous and flexible with low glass transition temperatures. As an additional feature, the ethyl or hydroxymethyl side groups of every PBO or PG repeating unit allow for the introduction of chirality into the polymer backbone, *i.e.* the preparation of stereoregular, isotactic BCPs. In particular, PBO is expected to maintain its amorphous character even in an isotactic configuration, which would be essential for applications requiring highly flexible and fluid membranes, for example for the functional reconstitution of membrane proteins. Additionally, the need to thoroughly dilute crystalline (isotactic) BCPs or to heat them above their melting or glass transition temperatures to form well-controlled self-assemblies prevents a combination with cargo sensitive to organic solvents or elevated temperatures. Advanced applications such as platforms to analyse enzymatic cascade reactions or cell mimics with controlled passage of substrates are thus considerably more difficult with (semi-) crystalline BCPs. Polymeric self-assemblies composed of isotactic, yet non-crystalline BCPs to create fully flexible and amorphous chiral membranes would overcome these limitations but have not been available so far. Such BCPs would permit to evaluate the effect of stereoregularity on the self-assemblies without compromising on flexibility and enable applications involving sensitive biomolecules such as membrane proteins.

In this thesis, the ability of (isotactic) PBO-*b*-PG-based BCPs to fill this gap will be analysed. The following questions will be addressed in this work:

- How can PBO-*b*-PG BCPs be synthesised in a quick and reproducible manner with narrow molecular weight distributions?
- Are PBO-*b*-PG based BCPs able to form well-controlled aqueous self-assemblies, in particular SUVs and GUVs?
- How does the introduction of chirality, *i.e.* the stereocontrol, affect the synthesis of PBO-*b*-PG?
- Do isotactic PBO-*b*-PG BCPs maintain their amorphous character?
- How does the stereocontrol affect the self-assembly of PBO-*b*-PG BCPs into SUVs and GUVs?

- Can membrane proteins be functionally reconstituted in membranes composed of atactic or isotactic PBO-*b*-PG?
- Can PBO-*b*-PG compete with the established PDMS-*b*-PMOXA regarding SUV and GUV formation and membrane protein insertion?
- Can chiral interaction be detected when adding a chiral substance to a dispersion of SUVs composed of isotactic BCPs?

To answer these questions, a set of PBO-*b*-PG BCPs has been synthesised, differing in their composition and configuration. The work is divided into four parts: the first one (chapter 3.1) presents the synthesis and characterisation of atactic and isotactic PBO-*b*-PG and PDMS-b-PMOXA. Differences between atactic and isotactic (*R*)-PBO-*b*-(*R*)-PG and (*S*)-PBO-*b*-(*S*)-PG BCPs regarding synthesis, structural, optical and thermal properties will be discussed. In the second part (chapter 3.2), it will be elucidated which BCP composition and which self-assembly method is favourable to obtain homogenous phases of self-assemblies, particularly vesicles. This knowledge will be applied to create SUVs and GUVs composed of atactic and isotactic PBO-*b*-PG as well as PDMS-*b*-PMOXA. The third part (chapter 3.3) focuses on the application of atactic and isotactic BCPs as microreactors by reconstituting membrane proteins. In order to set the finding into context, comparisons with the established PDMS-*b*-PMOXA are drawn. Additionally, in the fourth part (chapter 3.4) potential chiral interaction will be analysed by adsorbing chiral substances onto SUVs composed of the (*R*)- or (*S*)-BCP, monitored by QCM-D.

3. Results and Discussion

Text and figures of parts of this chapter are adapted and modified from:

"Deepening the insight into poly(butylene oxide)-block-poly(glycidol) synthesis and self-assemblies: micelles, worms and vesicles" by Riccardo Wehr, Jens Gaitzsch, Davy Daubian, Csaba Fodor and Wolfgang Meier in *RSC Advances*, **2020**, 10, 22701-22711. Reproduced from Ref.[189] with permission from the Royal Society of Chemsitry.

and

"Fully amorphous atactic and isotactic block copolymers and their self-assembly into nano- and microscopic vesicles" by Riccardo Wehr, Elena C. dos Santos, Moritz Muthwill, Vittoria Chimisso, Jens Gaitzsch and Wolfgang Meier in *Polymer Chemistry*, **2021**, 12, 5377-5389. Reproduced from Ref.[190] with permission from the Royal Society of Chemistry.

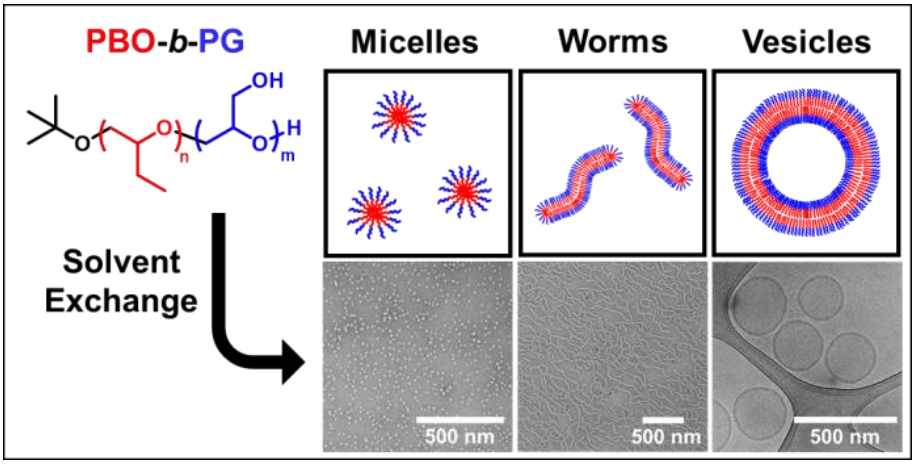

Figure 9: Graphical abstract of the aqueous self-assembly of atactic PBO-*b*-PG BCPs.

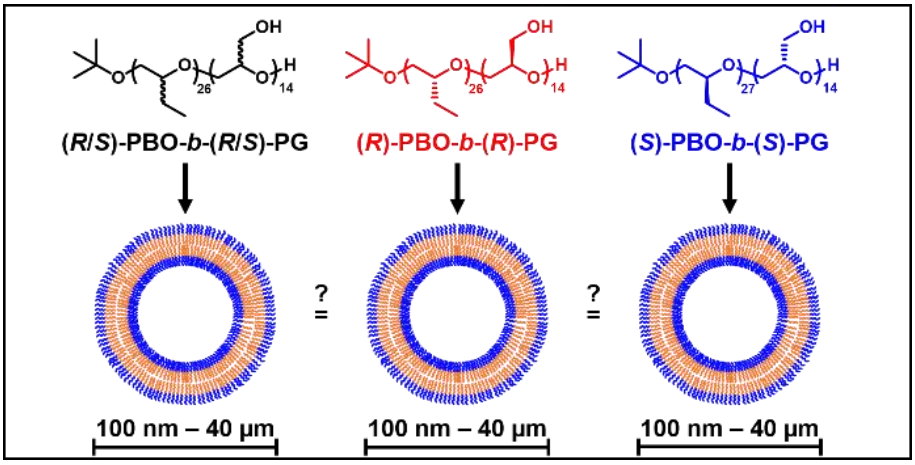

Figure 10: Graphical abstract of the self-assembly of atactic and isotactic PBO-*b*-PG into SUVs and GUVs.

3.1. Synthesis and characterisation of atactic and isotactic PBO-*b*-PG and PDMS-*b*-PMOXA

This chapter will give insights into the microwave-assisted synthesis of atactic and isotactic PBO-*b*-PG BCPs. Kinetic measurements will be presented, showing the high control and reproducibility of the polymerisations. Additionally, a thorough polymer characterisation consisting of ^{1}H NMR spectroscopy, GPC and DSC amongst others will be provided. A set of three similar BCPs with differing configuration will be synthesised and characterised systematically regarding their structural, optical and thermal properties. Additionally, the synthesis and characterisation of the commonly used PDMS-*b*-PMOXA will be presented.

3.1.1. Synthesis of atactic PBO-*b*-PG

The amphiphilic PBO-*b*-PG diblock copolymers were synthesised in two sequential microwave-assisted AROP. The synthesis protocol involved three steps: the hydrophobic block PBO was synthesised first, followed by the chain extension with the protected glycidol derivative EEGE and eventually, the acetal protecting group of the PEEGE block was removed to obtain the final BCP (Figure 11).

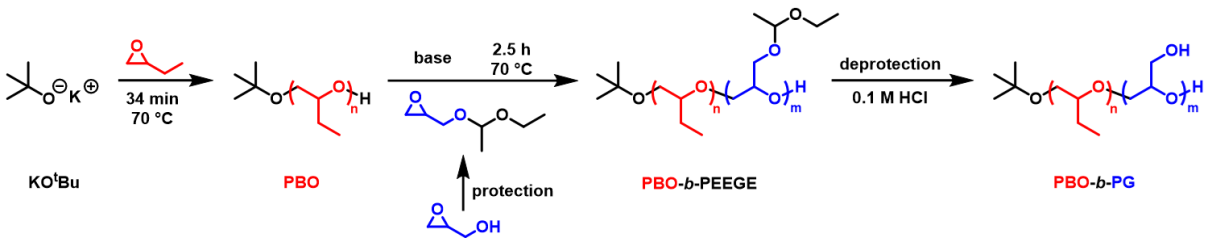

Figure 11: Reaction equation for the synthesis of the amphiphilic diblock copolymer poly(butylene oxide)-*block*-poly(glycidol) (PBO-*b*-PG).

Commercially available KO^{t}Bu was chosen as initiator for the first block. The polymerisation of BO monomer was conducted in a microwave-based reaction at 70 °C. The use of 0.5 equivalents crown ether to solubilise the potassium ions both accelerated the reaction and led to a significantly reduced dispersity.[191,192] The kinetics of the reaction was analysed by ^{1}H-NMR spectroscopy and GPC. The linear increase of $\ln([M]_0/[M]_t)$ with reaction time t (Figure 12a) represented ideal first-order kinetics. Also the linear increase of the molecular weight with conversion, independently confirmed by ^{1}H NMR spectroscopy and GPC (Figure 12b), indicated that no unwanted monomer-consuming side reactions took place. The data confirmed a living and well-controlled polymerisation up to a high conversion of

86%. The dispersity remained low during polymerisation and was decreased even further to 1.05 after purification. The GPC traces of every time point of the kinetic measurements can be found in Figure 13. The use of the largest possible microwave vessel with a capacity of 20 mL required a stepwise temperature increase from 50 °C over 60 °C, until the actual reaction temperature of 70 °C was reached. A faster heating program would have forced a system shutdown due to the accelerated heating rate. The reaction was quenched by adding methanol to obtain hydroxy end groups for the following chain-extension. Compared to time-consuming conventional syntheses at lower temperatures (6 days at –15 °C[193] or 24 h at 25 °C[95]) the microwave-based protocol benefited from a drastically reduced reaction time of only 34 min. The quick heating based on permeating microwave irradiation[18] compared to conventional oil bath-based heat-flow syntheses appeared advantageous for retaining both the high control and the living character. Side reactions or broadening of the molecular weight distribution due to the elevated temperatures was not observed.

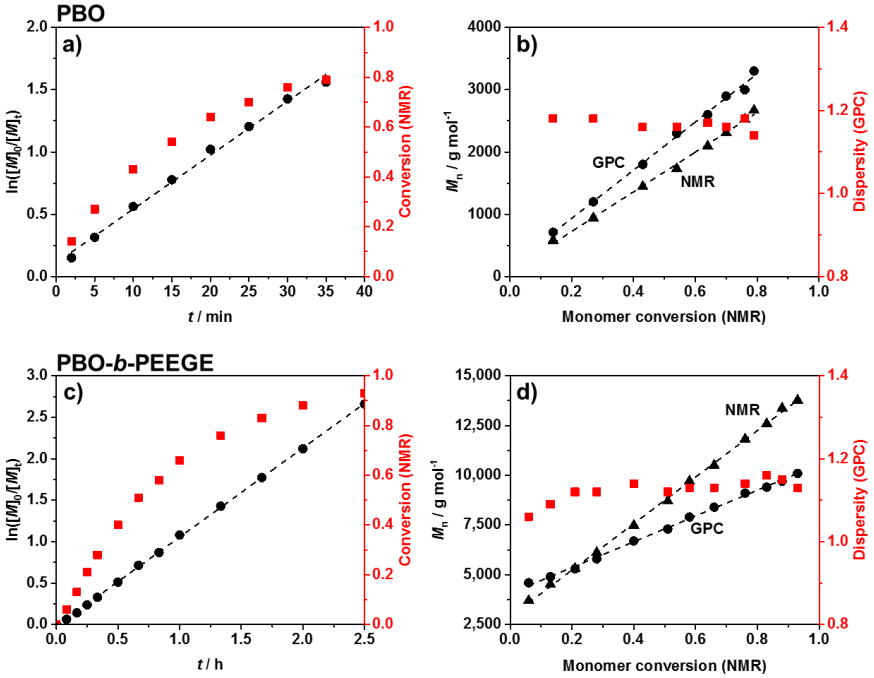

Figure 12: Kinetic analyses for the synthesis of PBO (a and b) and PBO-*b*-PEEGE (c and d). a) and c) show the living character of both polymerisations up to high conversions. b) and d) show the absence of monomer-consuming side reactions and low dispersities during the syntheses.

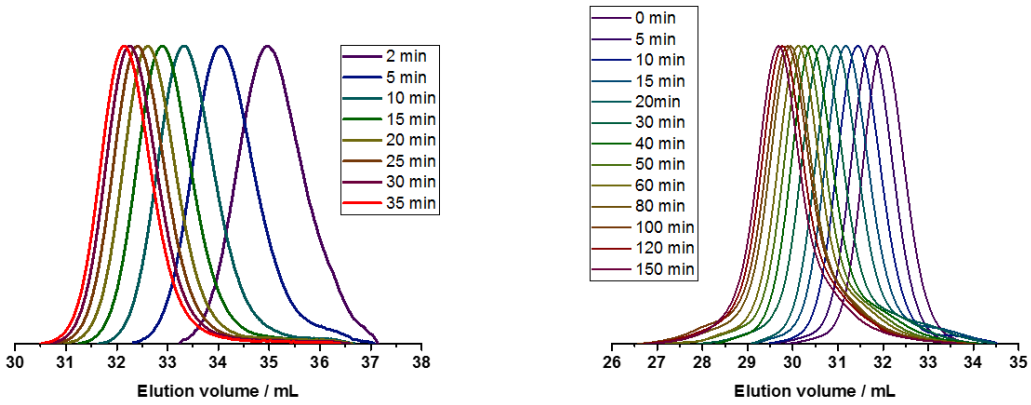

Figure 13: GPC traces of the kinetic measurements of PBO (left) and PBO-*b*-PEEGE (right) in DMF. The latter one shows the development of a small PEEGE homopolymer shoulder with increasing reaction time.

Chain-extension of the PBO macroinitiator was performed in a similar, microwave-based synthesis using EEGE as an acetal protected glycidol derivative. KNaph was used to activate the PBO homopolymer. A complete deprotonation and thus the titration end point with KNaph was visually recognised as the solution remained clear during deprotonation and the dark green colour of KNaph remained as soon as the reaction was complete.[194] The use of KNaph as base also benefited from reduced side reactions like chain-transfer, enabeling lower dispersities especially at higher molecular weights than comparable metal alkoxides.[195,196]

Kinetic measurements confirmed that the EEGE polymerisation at 70 °C again yielded a perfectly linear growth (Figure 12c) and retained a living character up to high conversions. Also here both NMR and GPC measurements confirmed the high control. The almost ideal linear increase of molecular weight with EEGE conversion (Figure 12d) again proved the absence of any monomer-consuming side reactions or the production of high quantities of unwanted homopolymer. Polymerisations were conducted until an EEGE conversion of typically 93% was reached. The high conversion rate did not have a negative effect on the dispersity, which remained low at all time spots (1.1–1.2, Figure 12d, Figure 13) and was even lower after purification. The use of crown ether here was redundant as the low dispersity was achieved even without on a much shorter time scale of 2.5 hours than conventional PEEGE syntheses (3 or 4 days at 50 °C[197,198] or 24 h at 25 °C[95]). Acidic cleavage of the acetal protecting group on every PEEGE repeating unit was done without previous purification of the BCP in 0.1 M HCl. The low concentration of acid was necessary to prevent the *tert.* butoxy end group from being cleaved as well, a risk more pronounced for higher acid concentrations.[199] A possible loss of end groups would have been detectable by NMR spectroscopy by an apparently increased DP of both blocks. As this was not observed, it was concluded that the end groups stayed intact. After neutralisation, the mixtures were purified by dialysis to give the final diblock copolymers (Table 1).

Table 1: Composition, molecular weight, hydrophilic mass ratio *f*, dispersity and glass transition temperatures of the PBO-*b*-PG diblock copolymers. Values determined by (a) ^{1}H-NMR, (b) GPC and (c) DSC.

composition[a]	M_n [a] / g·mol^{-1}	*f*-ratio[a]	$Đ$[b]	T_g[c] (PBO)/ °C	T_g[c] (PG)/ °C
PBO_{42}-*b*-PG_{77}	8800	0.65	1.10	–71	–14
PBO_{42}-*b*-PG_{35}	5700	0.46	1.09	–68	–22
PBO_{42}-*b*-PG_{21}	4700	0.33	1.09	–68	–23
PBO_{36}-*b*-PG_{59}	7000	0.62	1.11	–	–
PBO_{30}-*b*-PG_{38}	5100	0.56	1.09	–	–
PBO_{50}-*b*-PG_{18}	5000	0.27	1.04	–	–
PBO_{67}-*b*-PG_{14}	5900	0.17	1.08	–	–

3.1.2. Characterisation of atactic PBO-*b*-PG

All polymers were characterised using ^{1}H-NMR spectroscopy, GPC and DSC. ^{1}H-NMR spectra were used to determine the average composition and molecular weight of all polymers. Figure 14 shows the ^{1}H-NMR spectrum of PBO_{42}. The signal of the *tert*. butoxy end group (A) was used as integration reference to determine the DP of the PBO macroinitiator. As this signal was overlaid in the sprectum of the crude PBO-*b*-PEEGE (Figure 15), the methylene signal of the PBO side groups (D) was used as integration reference and set to a DP of 42 for the BCPs before deprotection. To be consistent, this signal was retained as reference also for the spectra of the cleaved and purified BCPs. A representative spectrum of the cleaved and purified PBO_{42}-*b*-PG_{21} is shown in Figure 16. The DP of the PG block was determined with 21 units based on the signals between 3.4 and 3.8 ppm. The average molecular weights of all BCPs as well as the hydrophilic mass ratios *f* are summarised in Table 1.

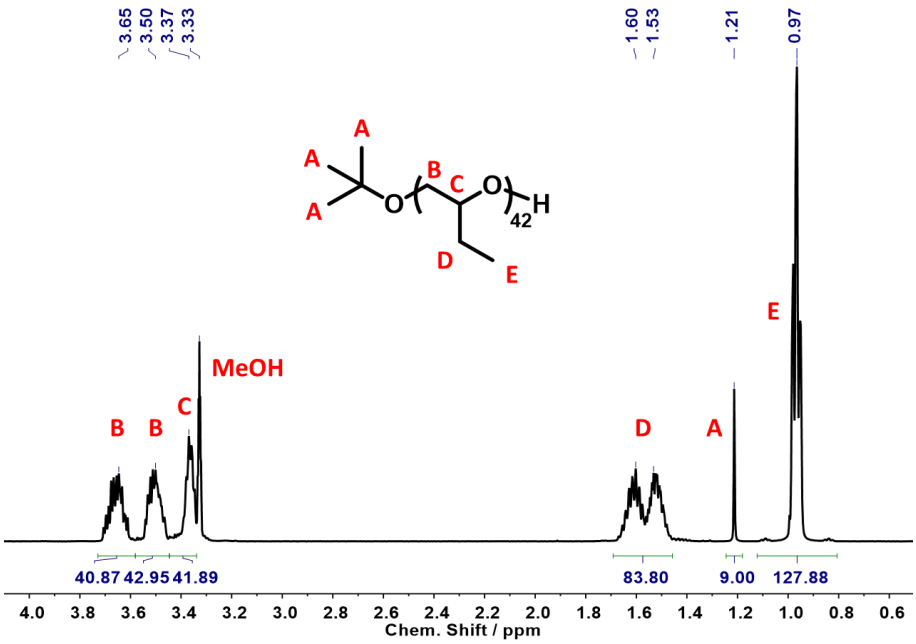

Figure 14: ^{1}H-NMR spectrum of PBO_{42} in MeOD. Signal A was used as integration reference. The DP was determined using signal D.

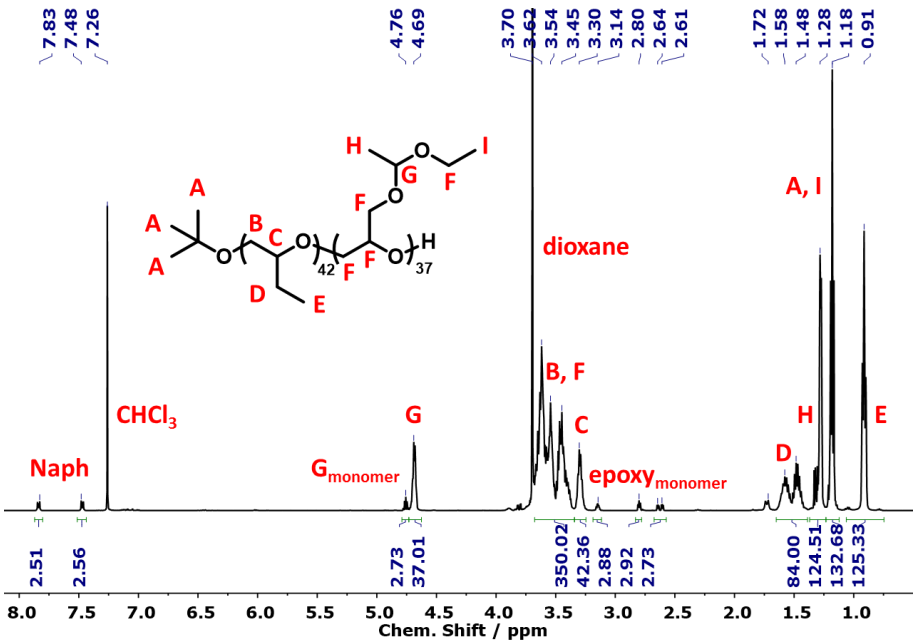

Figure 15: ^{1}H NMR spectrum of crude PBO_{42}-*b*-$PEEGE_{37}$ in $CDCl_3$, as the BCP was not purified before the cleavage of the protecting groups. Using the *tert*. butoxy end group as integration reference was not possible due to the overlaid signal, so the PBO peak D was set to its integral according to the previously determined DP of 42. The conversion was calculated by the integrals of the signals G of monomer and polymer: conversion = 1-($G_{monomer}$/(G+$G_{monomer}$) = 93%.

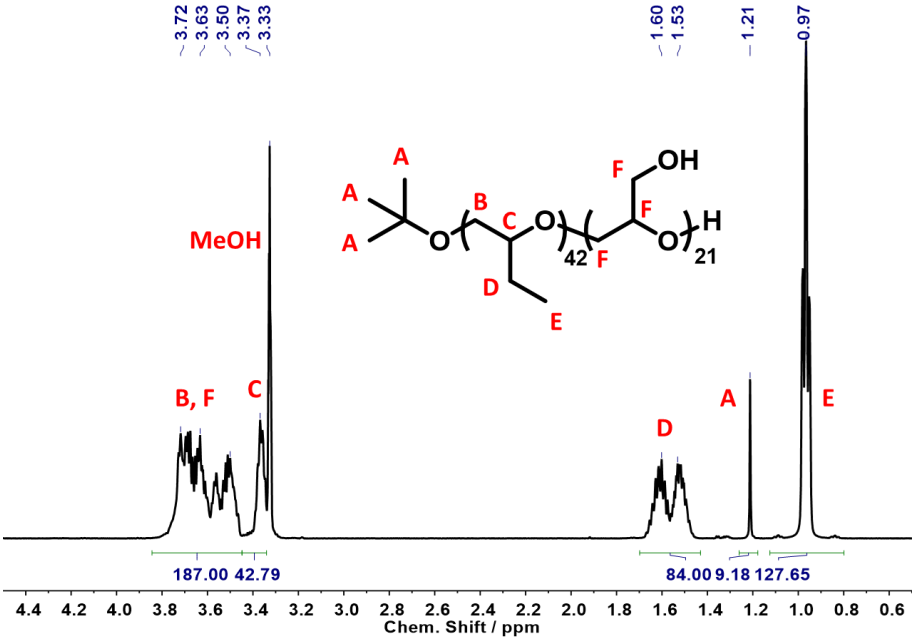

Figure 16: ^{1}H-NMR spectra of PBO_{42}-*b*-PG_{21} in MeOD. Signal D was used as integration reference. The DP of PG was determined using signals B and F.

Figure 17 shows representative GPC traces of PBO_{42} homopolymer (red), PBO_{42}-*b*-$PEEGE_{37}$ before cleavage of the protecting groups (black) and the final PBO_{42}-*b*-PG_{35} (blue). After addition of the PEEGE block, the trace of the PBO_{42} homopolymer ($Đ$ = 1.05) was shifted to higher molecular weights while the dispersity remained low ($Đ$ = 1.10), showing a successful chain-extension. Cleavage of the protecting groups resulted in a shift to smaller molecular weights with the dispersity remaining at its low level of 1.09. The small low molecular weight shoulders in the traces of PBO_{42}-*b*-$PEEGE_{37}$ and PBO_{42}-*b*-PG_{35} corresponded to small amounts of PEEGE and PG homopolymer, which was probably caused by a slight overtitration with KNaph or by transfer reactions. Especially for BCPs with shorter hydrophilic blocks, it was possible to remove remaining PG homopolymer by dialysis to a large extend (Figure 18), explaining the slightly decreased DP of PG compared to the DP of PEEGE. Remaining PBO homopolymer could not be observed, indicating a complete deprotonation and chain-extension of all PBO chains.

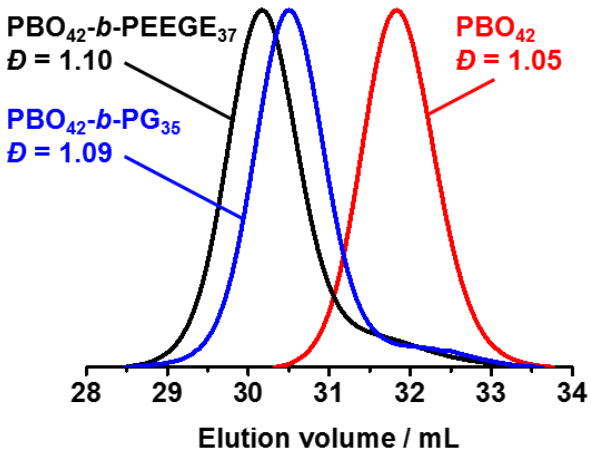

Figure 17: GPC traces of PBO_{42} homopolymer (red), PBO_{42}-*b*-$PEEGE_{37}$ before cleavage of the protecting group (black) and PBO_{42}-*b*-PG_{35} after cleavage of the protecting group (blue) in DMF showing low dispersities in all steps.

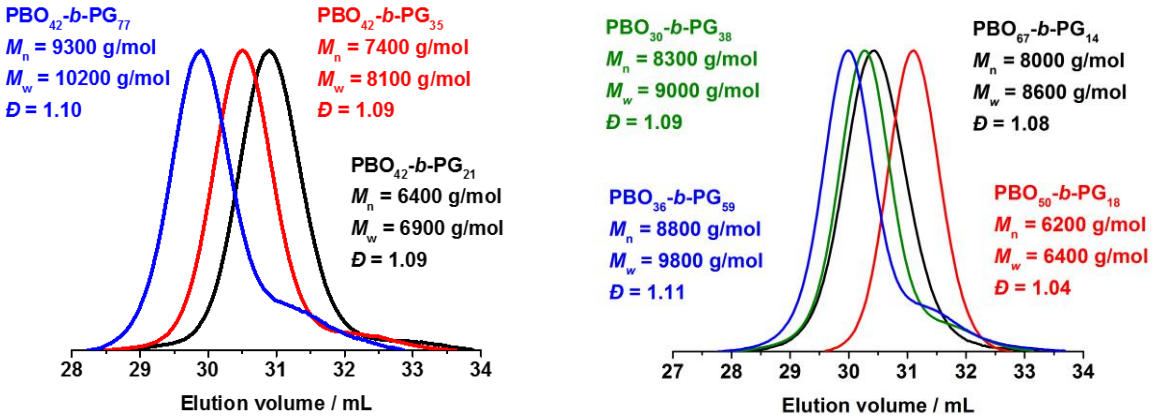

Figure 18: GPC traces of the BCPs presented in Table 1 in DMF showing low dispersities. The small low molecular weight shoulders originating from PEEGE/PG homopolymer are visible.

Thermal transitions of the BCPs were analysed by DSC to elucidate their suitability for applications which require flexible and amorphous membranes. The representative traces of PBO_{42} and PBO_{42}-*b*-PG_{35} are shown in Figure 19. The PBO block of the BCP exhibited a T_g of –68 °C, which was in agreement to the measured T_g of the PBO homopolymer, –73 °C, as well as its literature value of –70 °.[113] The T_g of the PG block was detected at –22 °C, which matched the literature values of PG homopolymers between –32 °C[200] and –15 °C[201] depending on end groups and chain lengths. Also the DSC traces of the other two BCPs (Figure 20) exhibited a similar behaviour with T_g values in similar ranges. The T_g values of the PG blocks increased with increasing DP from –23 °C for DP 21 over –22 °C for DP 35 to –14 °C for DP 77.[142] The appearance of two separate glass transition areas below room temperature as well as the absence of first order transitions like crystallisation or melting confirmed the presence of two distinct, immiscible and amorphous blocks.

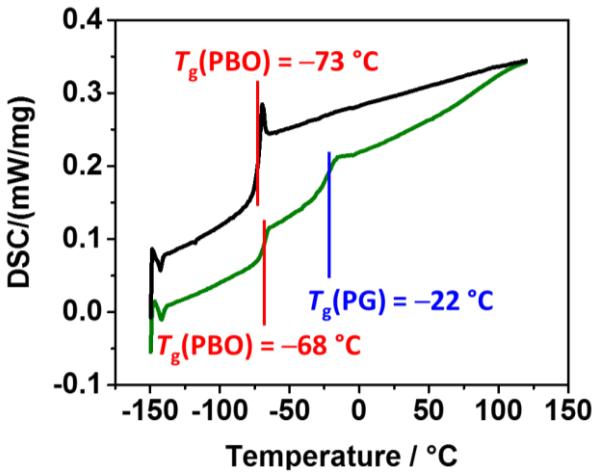

Figure 19: DSC traces of PBO_{42} homopolymer (black) and PBO_{42}-*b*-PG_{35} BCP (green) showing distinct glass transition temperatures for both blocks of the BCP.

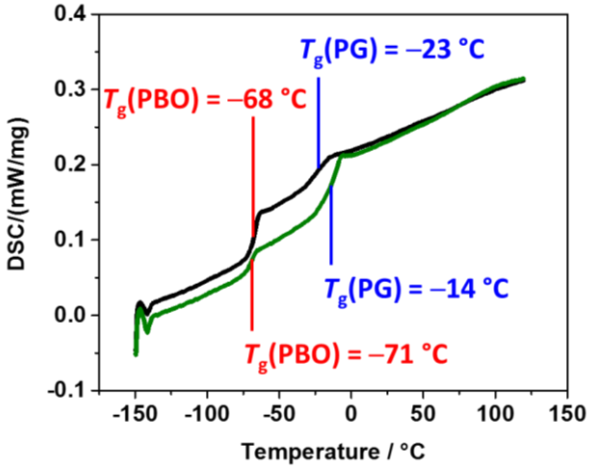

Figure 20: DSC traces of PBO_{42}-*b*-PG_{21} (black) and PBO_{42}-*b*-PG_{77} (green).

3.1.3. Synthesis of isotactic PBO-*b*-PG

The microwave-assisted AROP of isotactic PBO-*b*-PG BCPs followed the previously established procedure. Three similar BCPs were synthesised in this manner, differing only in their configuration (Figure 21): one fully atactic PBO-*b*-PG, referred to as (*R*/*S*)-BCP, and two all-isotactic PBO-*b*-PGs: one of them in (*R*) configuration on all repeating units of both blocks, referred to as (*R*)-BCP, and one in (*S*) configuration, referred to as (*S*)-BCP. The stereocontrol was achieved solely by using racemic or enantiopure monomers of both blocks. Additionally, PG homopolymers of all three configurations were synthesised following a similar protocol (Figure 22). Thus, a series of nine atactic and isotactic polymers – three PBO homopolymers, three PG homopolymers and three PBO-*b*-PG BCPs in (*R*/*S*), (*R*) and (*S*) configuration – were obtained (Table 2).

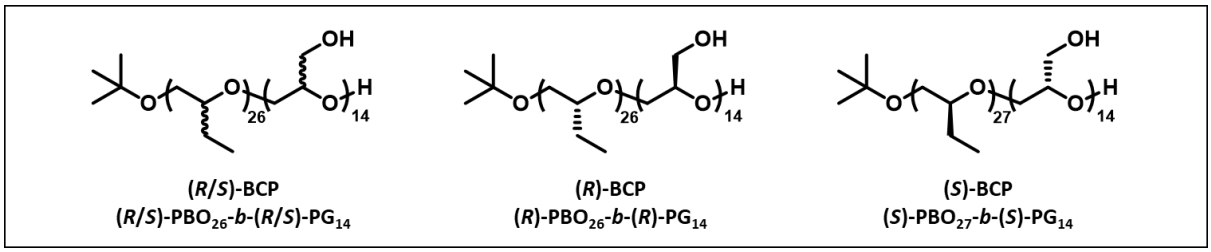

Figure 21: Structures of the atactic (*R*/*S*)-BCP, the isotactic (*R*)-BCP and the isotactic (*S*)-BCP.

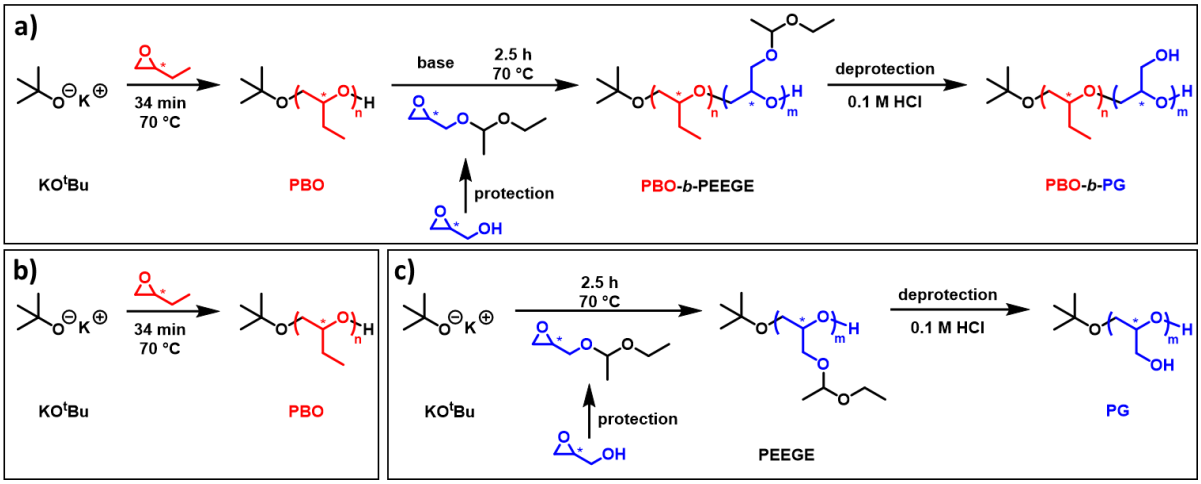

Figure 22: Reaction equations for the syntheses of atactic and isotactic a) PBO-*b*-PG BCPs, b) PBO homopolymers and c) PG homopolymers.

It should be noted that all compounds of one configuration are consistently referred to as (*R*) or (*S*). For example, for protected compounds annotated (*R*)-EEGE and (*R*)-PEEGE, the official configuration according to IUPAC would be (*S*)-EEGE and (*S*)-PEEGE, respectively, because of the changing priorities of the side groups compared to their unprotected (*R*)-glycidol precursors and (*R*)-PG successors. For the sake of clarity and simplicity, the selected annotation will be used throughout, referring to the related compounds of (*R*)-glycidol and (*R*)-PG as (*R*)-EEGE and (*R*)-PEEGE and *vice versa* for the (*S*) compounds.

In order to elucidate whether the configuration of the monomers affected the polymerisation process, kinetic measurements were performed (Figure 102-Figure 110). The kinetics of the PBO syntheses starting from the enantiopure monomers (*R*)- and (*S*)-BO and of their chain extensions with (*R*)- and (*S*)-EEGE were analysed and compared to the data obtained for the racemic mixtures. For all polymerisations, $\ln([M]_0/[M]_t)$ showed a linear increase with the reaction time *t*, representing a living polymerisation and ideal first-order kinetics (Figure 23). The reaction constant (the slope of the linear fit) was calculated for all PBO and PBO-*b*-PEEGE polymerisations. For the PBO syntheses, values of about 40 min^{-1} were determined and for PBO-*b*-PEEGE values of about 1.05 h^{-1}. Within experimental error, these kinetic constants were independent of the respective configuration. This is evident from the fact that the (*R*/*S*)-monomer is a racemic mixture of both enantiomers. Hence, it confirmed that atactic

PBO and PBO-*b*-PEEGE and thus the final PBO-*b*-PG consisted of statistically distributed (*R*) and (*S*) repeating units, as no enantiomer was consumed quicker or slower than the other. The linear growth of the molecular weights with increasing conversion, as well as the low dispersities during the polymerisations (Figure 102 to Figure 107) were another proof for the high control and reproducibility of the reactions. Neither monomer-consuming side reactions nor the formation of unwanted PEEGE homopolymer in the case of the PBO-*b*-PEEGE syntheses could be observed.

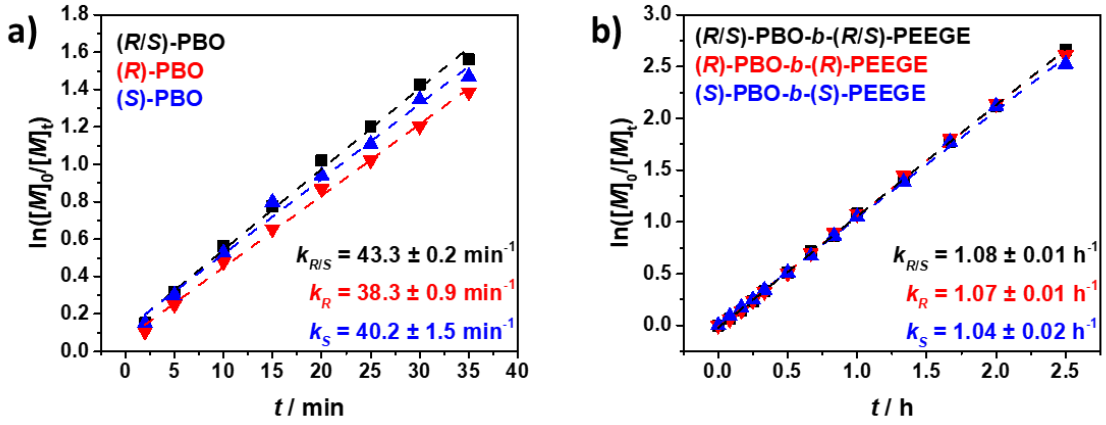

Figure 23: Kinetics of a) the PBO syntheses and b) the PBO-*b*-PEEGE syntheses. The reaction constants *k* are displayed for all three configurations.

3.1.4. Characterisation of isotactic PBO-*b*-PG

3.1.4.1. Structural characterisation

Table 2: Polymer characterisation. (a) Composition, molecular weight M_n and hydrophilic block ratio *f* determined by ^{1}H NMR spectroscopy. (b) Dispersity determined by GPC.

composition[a]	M_n[a] / g·mol^{-1}	*f*-ratio[a]	*Đ*[b]
(*R*/*S*)-PBO$_{26}$-*b*-(*R*/*S*)-PG$_{14}$	3000	0.35	1.06
(*R*)-PBO$_{26}$-*b*-(*R*)-PG$_{14}$	3000	0.35	1.06
(*S*)-PBO$_{27}$-*b*-(*S*)-PG$_{14}$	3100	0.34	1.06
(*R*/*S*)-PBO$_{27}$	2000	–	1.07
(*R*)-PBO$_{27}$	2000	–	1.07
(*S*)-PBO$_{27}$	2000	–	1.08
(*R*/*S*)-PG$_{30}$	2300	–	1.07
(*R*)-PG$_{28}$	2100	–	1.06
(*S*)-PG$_{30}$	2300	–	1.06

^{1}H NMR spectra revealed the DPs, molecular weights and hydrophilic block ratios *f* of all polymers. An exemplary spectrum of the (*S*)-BCP is presented in Figure 24; the spectra of all other polymers are

shown in Figure 111 to Figure 119. Three sets of similar PBO-*b*-PG BCPs, PBO and PG homopolymers were obtained, which possessed highly comparable DPs among themselves (Table 2). The signal of the *tert*. butoxy end groups was used as integration reference (signal A in Figure 24). The DPs of the PBO blocks were calculated using the side-group methylene signals D. The DPs of the PG blocks were calculated by integrating signals B, F, G and H and subtracting the respective number of protons of the overlaying PBO blocks. The DPs of the PBO homopolymers were 27, of the PG homopolymers 28-30, and of the BCPs 26-27 for the PBO blocks and 14 for the PG blocks. The *f*-ratios of the BCPs of 34-35% were in the range where vesicular structures were found for atactic PBO-*b*-PGs (section 3.1.3).

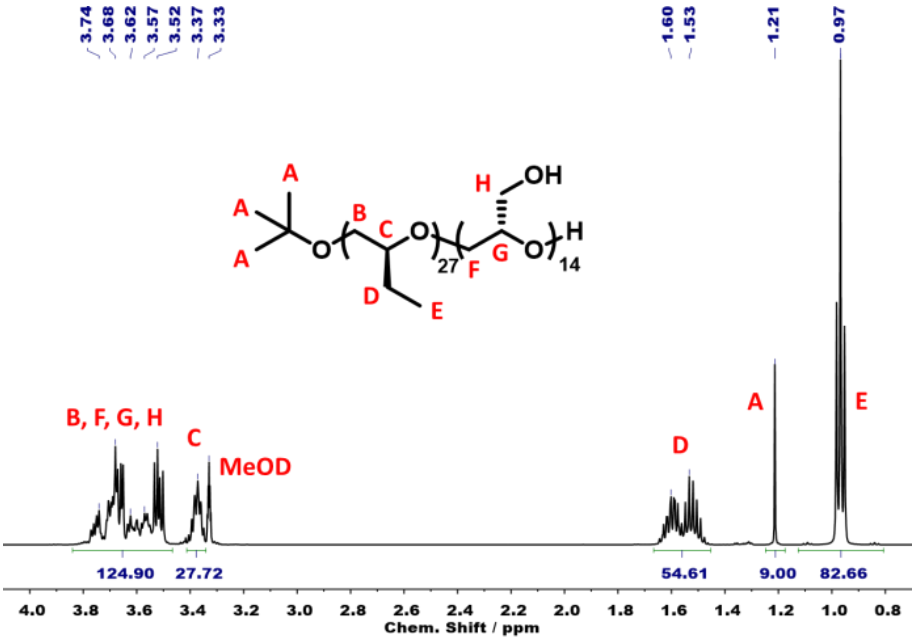

Figure 24: ^{1}H NMR spectrum of the (*S*)-BCP (*S*)-PBO$_{27}$-*b*-(*S*)-PG$_{14}$ in MeOD. Signal A was used as integration reference. The DP of the PBO block was calculated using signal D, the DP of the PG block was calculated using signals B, F, G and H and subtracting the respective protons of the PBO block.

GPC traces and their dispersities of all polymers are shown in Figure 25. The chain extension from the (*S*)-PBO precursor towards the (*S*)-BCP led to a shift to a lower elution volume. The (*S*)-PG homopolymer eluted at even lower volumes, despite having a lower molecular weight than the (*S*)-BCP, which indicates a greater solvodynamic volume of PG compared to PBO. Narrow distributions with dispersities between 1.06 and 1.08 were obtained for all nine polymers (Table 2). Similar solvodynamic volumes between polymers of the same molecular weight but with different configurations suggested that isotactic polymers did not adapt different conformations in DMF solution than atactic polymers. The formation of secondary structures such as helices in organic solvents thus seemed unlikely.

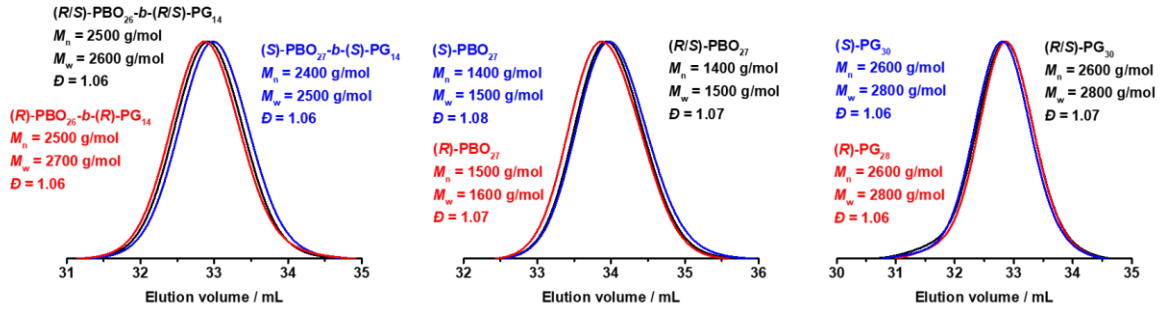

Figure 25: GPC elugrams and dispersities of the atactic and isotactic PBO-*b*-PG BCPs (left), PBO homopolymers (middle) and PG homopolymers (right) in DMF.

3.1.4.2. Quantification of meso diads

^{1}H NMR spectroscopy did not allow for a quantification of the isotactic content of the polymers, as an error-free integration of the respective signals B, C, F and G (Figure 24) was not possible. Hence, the quantitative determination was done by ^{13}C NMR spectroscopy (Figure 111 to Figure 119) as commonly done for isotactic polyethers.[194,202–206] An exemplary ^{13}C NMR spectrum of the (*R*/*S*)-BCP is displayed in Figure 26. Integration of the meso (*m*) and racemic (*r*) signals of the methylene groups adjacent to the chiral methine carbons led to the relative amount of *m* conjunctions (section 1.2.2, Figure 27).[1] For the polymers synthesised from racemic monomers, (*R*/*S*)-PBO, (*R*/*S*)-PG and both blocks of the (*R*/*S*)-BCP, meso diad contents of 48-55% *m* were found (Table 3). Those numbers indicated a statistical distribution of isotactic and syndiotactic conjunctions and confirmed the presence of atactic polymers. For the (*R*)- and (*S*)-PG homopolymers and the PG blocks of the (*R*)- and (*S*)-BCPs, 97-99% *m* was found, indicating a high excess of isotactic conjunctions. The (*R*)- and (*S*)-PBO homopolymers and the PBO blocks in the (*R*)- and (*S*)-BCPs showed slightly lower values of 88-91% *m*. Two possible explanations for the lower stereoregularity of the PBO blocks seemed reasonable: a lower *ee* of the enantiopure BO monomers (not disclosed by the manufacturer) or a more frequent attack on the tertiary epoxide carbon bearing the ethyl side group, as this provides less sterically hindrance compared to the more spacious acetal side group of the EEGE monomers. The latter effect would lead to a loss of the stereoregularity as well as to a loss of the regioregularity, *i.e.* to an inverted repeating unit (head-head or tail-tail connection).[202,205] In general, the polymerisations retained the configuration of both enantiopure monomers sufficiently well to refer to the resulting polymers as isotactic (*i.e.* stereoregular and regioregular). These results were in line with literature values of around 90% *m* for isotactic poly(propylene oxide) (PPO) synthesised in a similar manner.[194]

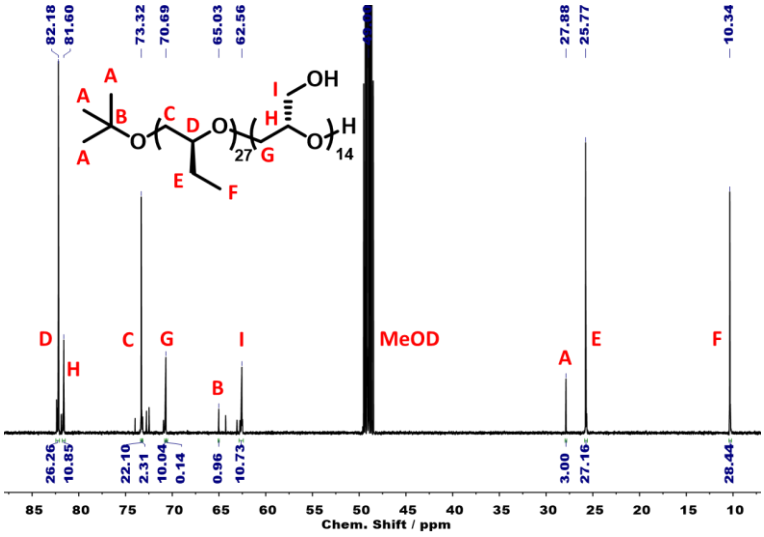

Figure 26: ^{13}C NMR spectrum of the (*S*)-BCP (*S*)-PBO$_{27}$-*b*-(*S*)-PG$_{14}$ in MeOD. The two integrals of signals C and G correspond to the meso (left integral) and racemic (right integral) diads.

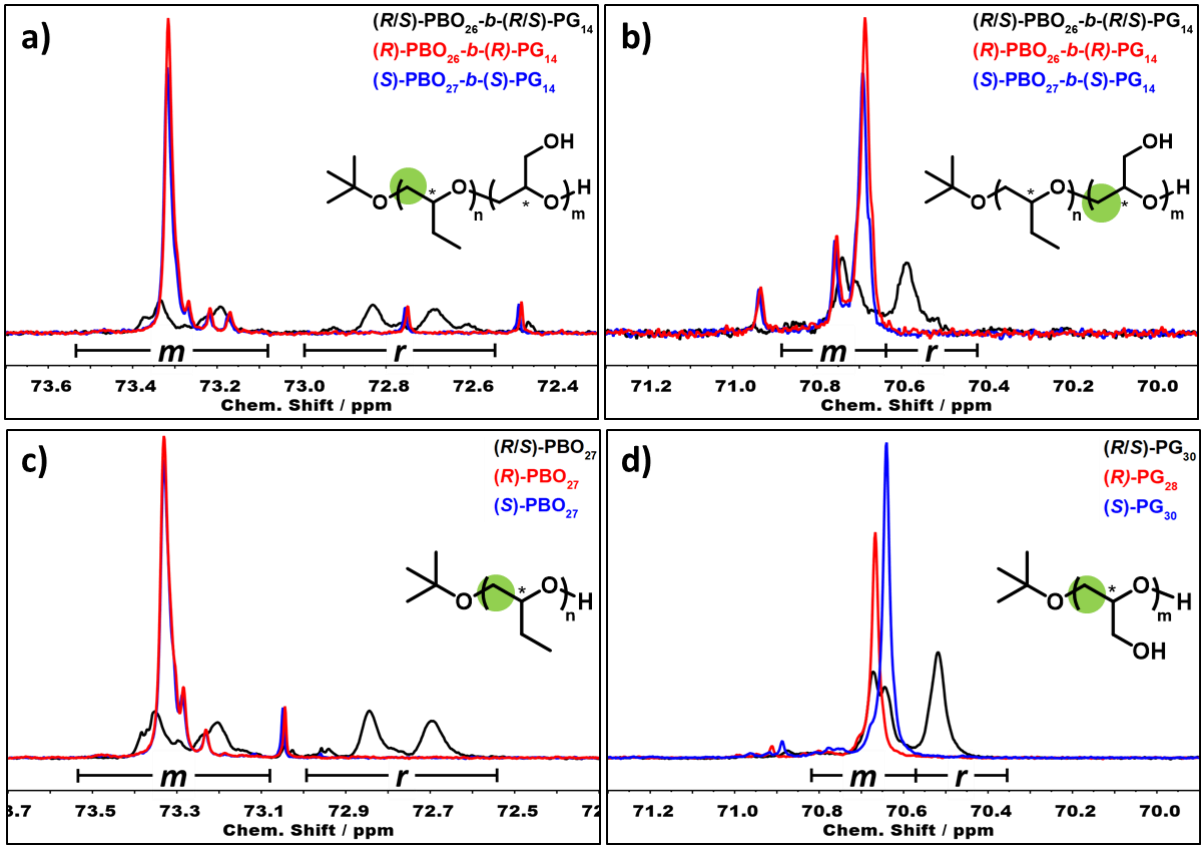

Figure 27: ^{13}C NMR signals of the methylene carbon atoms adjacent to the stereocentres, indicated in green, of the PBO and PG blocks of the atactic and isotactic polymers. a) PBO blocks of the BCPs, b) PG blocks of the BCPs, c) PBO homopolymers, d) PG homopolymers. The integrated areas correspond the meso (*m*) and racemic (*r*) diads.

Table 3: Calculation of the content of meso diads (*m*) from the integrals of the ^{13}C NMR peaks at 71 ppm (PG blocks) and 73 ppm (PBO blocks), taken from Figure 111-Figure 119.

composition	∫*m* (PBO)	∫*r* (PBO)	∫*m* (PG)	∫*r* (PG)	*m* (PBO)	*m* (PG)
(*R*/*S*)-PBO$_{26}$-*b*-(*R*/*S*)-PG$_{14}$	11.79	12.95	5.63	4.65	48%	55%
(*R*)-PBO$_{26}$-*b*-(*R*)-PG$_{14}$	21.23	2.15	9.62	0.30	91%	97%
(*S*)-PBO$_{27}$-*b*-(*S*)-PG$_{14}$	22.10	2.31	10.04	0.14	91%	99%
(*R*/*S*)-PBO$_{27}$	11.75	11.37	–	–	51%	–
(*R*)-PBO$_{27}$	21.53	2.80	–	–	88%	–
(*S*)-PBO$_{27}$	21.91	3.01	–	–	88%	–
(*R*/*S*)-PG$_{30}$	–	–	13.46	12.03	–	53%
(*R*)-PG$_{28}$	–	–	24.37	0.53	–	98%
(*S*)-PG$_{30}$	–	–	23.86	0.46	–	98%

3.1.4.3. Optical characterisation

In order to evaluate the optical properties of all compounds, polarimetry and CD spectroscopy measurements were performed. Racemic monomers and atactic polymers showed specific rotations close to 0, in contrast to enantiopure monomers and isotactic polymers (Table 4). Whilst the magnitude differed between compounds of one configuration, the direction always remained the same: all (*R*) compounds showed positive, all (*S*) compounds negative specific rotations. Similar compounds with opposite configuration showed specific rotations in the same magnitude. CD-spectra of all polymers showed absorptions only in the range between 180 and 205 nm (Figure 28). None of the atactic polymers was CD active, in contrast to isotactic polymers. Polymers with (*R*) configuration showed positive signals, whereas polymers with (*S*) configuration showed negative mirror signals of similar shape and intensity. Structurally induced phenomena such as Cotton effects were not visible, providing further evidence for the absence of any kind of secondary structure of the polymers in solution.[207] Thus, polarimetry and CD spectroscopy confirmed the presence of optically active isotactic polymers.

Table 4: Specific rotation $[\alpha]^{D}_{25}$ of the racemic and enantiopure polymers and monomers measured by polarimetry.

compound	(*R*/*S*)	(*R*)	(*S*)
PBO-*b*-PG	–1.6	+26.9	–31.2
PBO	–0.8	+32.8	–32.8
PG	+0.0	+16.0	–16.0
BO	+0.0	+7.2	–6.4
glycidol	+0.3	+11.6	–12.0
EEGE	+0.0	+9.9	–9.6
PEEGE	–0.01	+10.0	–10.1

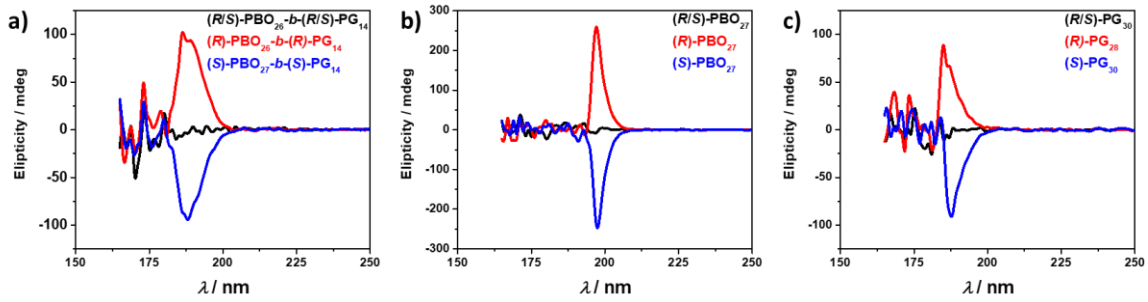

Figure 28: CD spectra of the atactic and isotactic a) BCPs, b) PBO homopolymers and c) PG homopolymers (right), measured in *n*-hexane (BCPs, PBOs) and water (PGs), respectively.

3.1.4.4. Thermal characterisation

To study the thermal properties and obtain further structural insights into the polymers, TGA and DSC measurements were performed. TGA thermograms of the BCPs showed the thermal decomposition at temperatures higher than 250 °C as a one-step process, independent of their configuration (Figure 29a). DSC measurements were performed for all BCPs and homopolymers (Figure 29b-d). Glass transitions were measured for all homopolymers, for PBO at about –75 °C, for PG at about –30 °C (Table 5). These numbers were independent of the configuration and in line with literature values for both homopolymers.[113,200,201] The thermograms of the three BCPs showed two glass transitions at about –70 °C and –30 °C (Table 5), in line with the ones measured for the respective homopolymers. The slightly lower T_g values of the PBO homopolymers compared to the PBO block in the BCPs could be explained by a less ordered chain packing because of the attached PG block and is literature-known.[142] Within the measurement accuracy, the T_g values were similar for all configurations. No first order transitions, *i.e.* melting or crystallisation, could be detected in any traces, confirming the presence of fully amorphous polymers. As for PG this is in contrast to the popular hydrophilic polyether PEG, which is semi-crystalline.[180] With respect to PBO, the low T_g and the absence of crystallinity should generally allow the insertion of membrane proteins into vesicles containing PBO as hydrophobic block. With this, the isotactic PBO blocks are in striking contrast to hydrophobic polymers that exhibit glass transition or melting above body temperature or (semi-) crystallinity depending on their tacticity or thermal history, such as PLA, PMMA, PS, PP or PPO.[25,180,185,208,209] Thus, PBO represents the poymer of choice to analyse stereospecific interactions such as membrane protein insertion into chiral, yet fully amorphous self-assembly membranes.

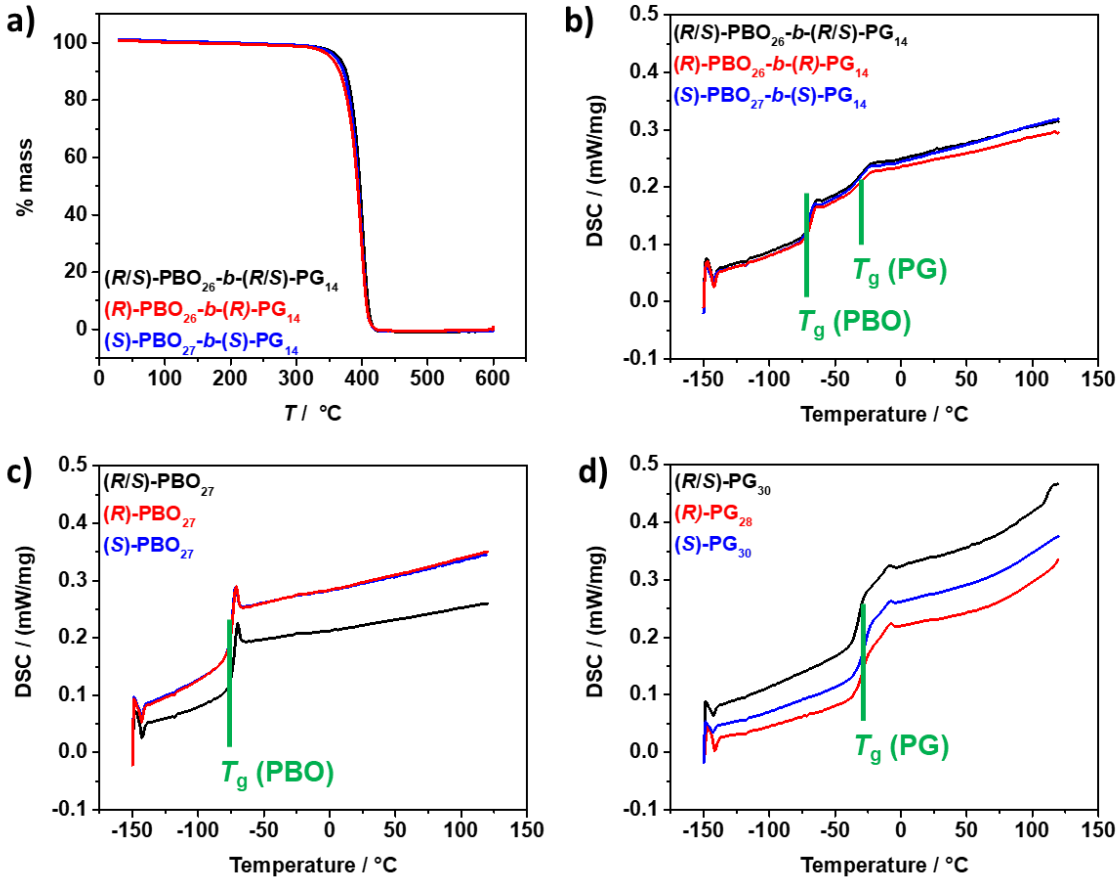

Figure 29: a) TGA thermogram of the atactic and isotactic BCPs. The mass loss of all BCPs is >99%. DSC thermograms of atactic and isotactic b) BCPs, c) PBO homopolymers and d) PG homopolymers with indicated glass transitions.

Table 5: Glass transition temperatures of atactic and isotactic polymers determined by DSC.

composition	T_g (PBO)/ °C	T_g (PG)/ °C
(*R*/*S*)-PBO$_{26}$-*b*-(*R*/*S*)-PG$_{14}$	–68	–29
(*R*)-PBO$_{26}$-*b*-(*R*)-PG$_{14}$	–69	–28
(*S*)-PBO$_{27}$-*b*-(*S*)-PG$_{14}$	–69	–29
(*R*/*S*)-PBO$_{27}$	–74	–
(*R*)-PBO$_{27}$	–75	–
(*S*)-PBO$_{27}$	–75	–
(*R*/*S*)-PG$_{30}$	–	–31
(*R*)-PG$_{28}$	–	–28
(*S*)-PG$_{30}$	–	–27

3.1.5. Synthesis and characterisation of PDMS-*b*-PMOXA

As a comparison to the above presented atactic and isotactic PBO-*b*-PG BCPs and their self-assemblies, a vesicle-forming BCP composed of PDMS-*b*-PMOXA was synthesised. The synthesis was performed in a conventional oil bath-based polymerisation following an established, yet optimised protocol (Figure 30, Figure 31, section 5.3.2).[110,111] Firstly, the PDMS precursor was synthesised in an AROP of D_3 starting from *n*-butyl lithium. After 40 h at room temperature, the polymerisation was quenched by adding chlorodimethylsilane. Subsequently, the obtained hydride end group was modified with 1-allyloxyethanol using Karstedt catalyst (Pt(dvs)), leading to monocarbinol-functionalised PDMS (PDMS-OH). ^{1}H NMR spectroscopy revealed a DP of 26 and a quantitative presence of hydroxy end groups (signals G, H and F in Figure 32). The terminal Si atom originated from the quenching and does not possess an adjacent oxygen atom, hence it would in theory not count as repeating unit. Note that here, however, it is treated and annotated as repeating unit, as the total number of Si atoms is easily accessible from signal D in the ^{1}H NMR spectrum and as it fulfills the same function as the terminal Si atom at the opposite chain end. Consequently, the stated DP of PDMS (26) corresponds to the number of silicon atoms within the chain and not the actual number of repeating units (25).

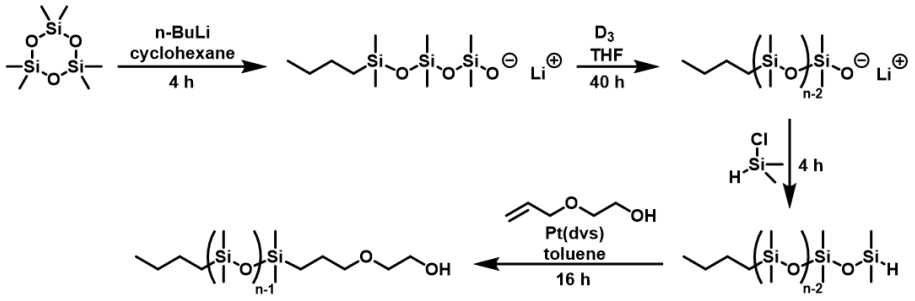

Figure 30: Reaction equation for the synthesis of monocarbinol-functionalised PDMS homopolymer.

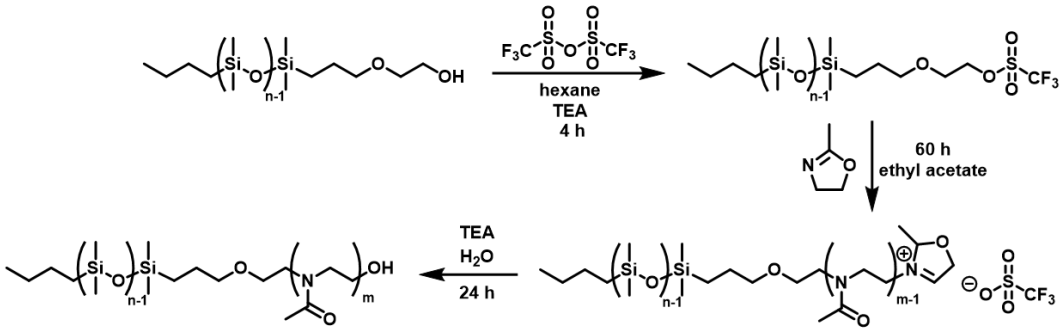

Figure 31: Reaction equation for the synthesis of PDMS-*b*-PMOXA starting from PDMS homopolymer.

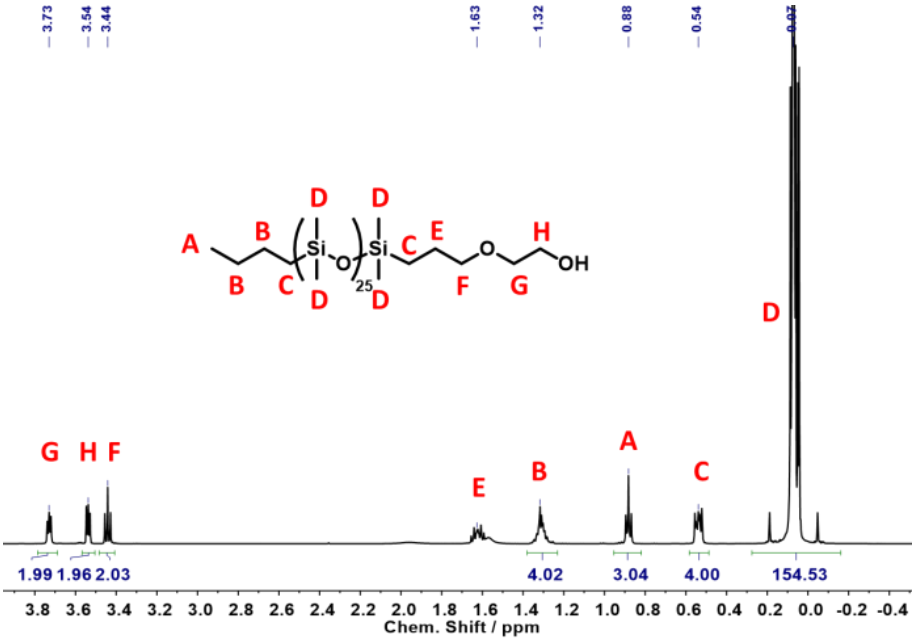

Figure 32: ^{1}H NMR spectrum of monocarbinol-functionalised PDMS homopolymer. Signal C was used as integration reference and the DP was calculated using signal D.

Chain-extension of the PDMS-OH precursor to obtain the final PDMS-*b*-PMOXA BCP was performed in a CROP of MOXA monomer. For this, PDMS-OH was activated with trifluoromethanesulfonic anhydrid (triflic anhydrid). A high conversion of 95% of the hydroxy end groups to triflates was confirmed by ^{1}H NMR spectroscopy (signal H in Figure 33). As PDMS-OTf degraded quickly in the NMR solvent an even higher triflate rate can be assumed right after activation and in inert environment. For the same reason the following MOXA polymerisation was performed immediately after activation. Storing the activated PDMS-OTf over a longer time was not possible. The polymerisation occured within 60 h at 40 °C in ethyl acetate and was quenched with a mixture of TEA and water to obtain hydroxy end groups. After precipitation of unreacted PDMS homopolymer and purification the final $PDMS_{25}$-*b*-$PMOXA_{10}$ (f = 30%) was obtained (Figure 34).

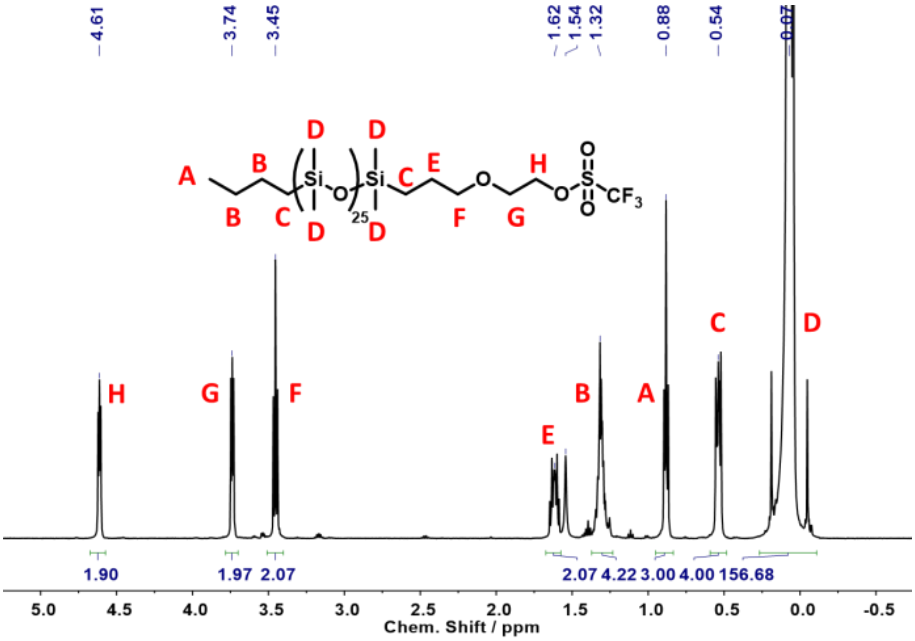

Figure 33: ^{1}H NMR spectrum of triflate-activated PDMS homopolymer.

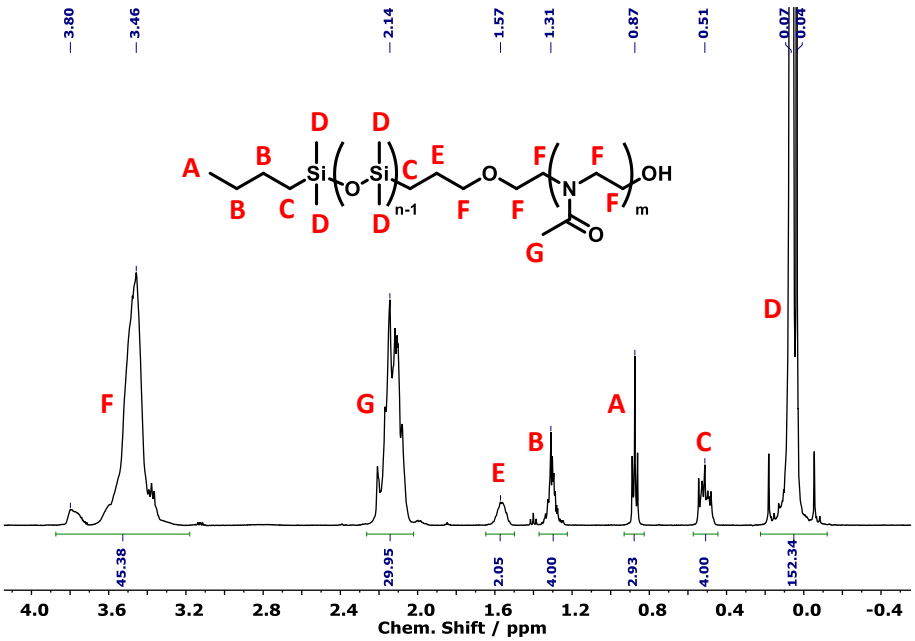

Figure 34: ^{1}H NMR spectrum of $PDMS_{25}$-*b*-$PMOXA_{10}$. Signal C was used as integration reference. The DP of PDMS was calculated using signal D, the DP of PMOXA was calculated using signal G.

GPC analysis of the $PDMS_{26}$-OH homopolymer and the $PDMS_{25}$-*b*-$PMOXA_{10}$ BCP in THF revealed monomodal distributions and dispersities of 1.17 and 1.19, respectively (Figure 35). The comparably high dispersities can be attributed to the PDMS synthesis, as the addition of one D_3 monomer leads to an increase of the DP by 3 repeating units. A high dispersity was thus expected and is literature-known for PDMS-*b*-PMOXA.[110,210]

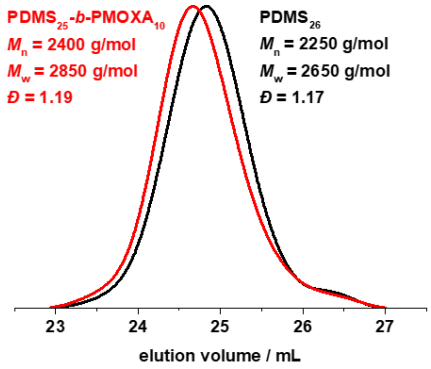

Figure 35: GPC elugrams of $PDMS_{25}$ (black) and $PDMS_{25}$-*b*-$PMOXA_{10}$ (red), measured in THF.

Thermal transitions were analysed using DSC. Two distinct glass transitions could be observed, one at −124 °C, corresponding to the PDMS block and being close to its literature value of −125 °C[120] and a second one at 17 °C, corresponding to the PMOXA block (Figure 36). First order transitions such as melting or crystallinisation were absent. The fully amorphous character and the low T_g were crucial for the membrane protein insertion performed in the present and other studies.[107,125]

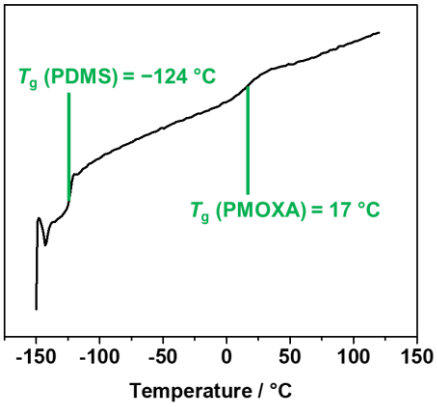

Figure 36: DSC thermogram of $PDMS_{25}$-*b*-$PMOXA_{10}$, showing two distinct glass transitions for both blocks.

3.1.6. Conclusion

The first part of the thesis presented the well-controlled and quick synthesis of atactic and isotactic PBO-*b*-PG and PDMS-*b*-PMOXA diblock copolymers. The properties of the PBO-*b*-PG BCPs, *i.e.* low dispersities, fully amorphous and biocompatible, highlight that PBO-*b*-PG is a promising BCP for self-assembly applications. Kinetic analyses confirmed the living character, high control and reproducibility of the polymerisations. Following the optimised synthetic conditions presented for the atactic PBO-*b*-

PG, a set of three similar atactic and isotactic BCPs and homopolymers was prepared, differing solely in their configurations. The quality of the polymers in terms of similarity and isotacticity was proven by different characterisation techniques such as ^{1}H and ^{13}C NMR spectroscopy, GPC, DSC, polarimetry and CD spectroscopy. In comparison to the commonly used PDMS-*b*-PMOXA, the synthesis and self-assembly of PBO-*b*-PG possessed several differences, drawbacks and advantages: the microwave-based synthesis was significantly shorter and better controlled, *i.e.* reproducibility and dispersity were enhanced. On the other hand, the batch size was limited by the size of the microwave vessels.

3.2. Self-assembly of atactic and isotactic PBO-*b*-PG and PDMS-*b*-PMOXA

This chaper will provide insights into the aqueous self-assembly of atactic and isotactic PBO-*b*-PG as well as PDMS-*b*-PMOXA. Firstly, the self-assembly of atactic PBO-*b*-PG into various nano- and microscopic structures including spherical micelles, wormlike micelles, SUVs and GUVs will be presented and analysed by a combination of light scattering, electron microscopy and fluorescence microscopy techniques. The effect of different formation methods (solvent exchange and film rehydration) for nanoscopic self-assemblies will be highlighted. Then, the observed structures will be classified in dependence on the established self-assembly theory. Subsequently, the formation of SUVs and GUVs composed of isotactic PBO-*b*-PG by solvent exchange and double emulsion microfluidics, respectively, will be presented. Eventually, the self-assembly of PDMS-*b*-PMOXA into SUVs and GUVs will be analysed.

3.2.1. Self-assembly of atactic PBO-*b*-PG

Self-assembly of atactic PBO-*b*-PG was conducted by solvent exchange to obtain pure phases of nanoscopic micelles, worms and SUVs. Solvent exchange was done by adding water to a solution of BCP in THF and removal of the organic solvent by dialysis (Figure 7). A slow addition of water (10 µL/min) together with moderate stirring (300 rpm) was essential to obtain pure self-assembly phases. Faster addition rates (40 µL/min or more) led to precipitation or impure phases. The standard protocol involved a stirring time over two nights before the dialysis was started. However, a kinetic analysis (Figure 37) indicated that already six hours after the addition of water had started, the assemblies were completely formed. Additionally, the kinetic studies proved that the removal of organic solvent did not lead to structural changes of the assemblies, neither in their sizes nor in the morphology

observed by TEM imaging. The absence of morphological changes over the next days of stirring indicated that the self-assembly process was complete and the structures were stable. All nanoscopic self-assemblies in water were analysed by TEM and DLS, the SUVs additionally with SLS and Cryo-TEM (Table 6).

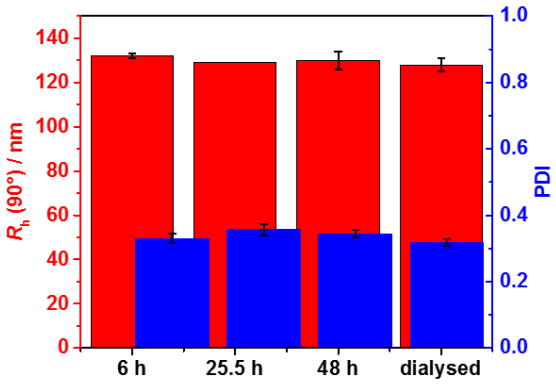

Figure 37: Hydrodynamic radii and PDIs measured by DLS of the self-assembly of PBO_{42}-*b*-PG_{21} showing an apparently finished self-assembly process already after 6 hours after the start of the addition of water.

Table 6: Composition, hydrophilic mass ratio *f* and DLS and SLS results of the self-assembled structures of the PBO-*b*-PG diblock copolymers presented in this chapter. The top three entries correspond to BCPs which form pure phases of self-assemblies and which are discussed in detail. The bottom four entries correspond to mixed phases of self-assemblies for comparison. Values determined by (a) ^{1}H-NMR, (b) DLS and (c) SLS, for vesicles after extrusion with a 200 nm membrane (d).

composition[a]	*f*-ratio[a]	structure	R_h[b] / nm	PDI[b]	R_g[c] / nm	$\rho = R_g/R_h$
PBO_{42}-*b*-PG_{77}	0.65	micelles	11.2 ± 0.6	0.40 ± 0.05	–	–
PBO_{42}-*b*-PG_{35}	0.46	worms	26.0 ± 2.0	0.33 ± 0.02	–	–
PBO_{42}-*b*-PG_{21}	0.33	SUVs	108 ± 11[d]	0.15 ± 0.05[d]	101[d]	0.93[d]
PBO_{36}-*b*-PG_{59}	0.62	mixed	20.1 ± 2.0	0.47 ± 0.01	–	–
PBO_{30}-*b*-PG_{38}	0.56	mixed	12.1 ± 0.4	0.45 ± 0.01	–	–
PBO_{50}-*b*-PG_{18}	0.27	mixed	194 ± 3	0.37 ± 0.02	–	–
PBO_{67}-*b*-PG_{14}	0.17	mixed	120 ± 6	0.31 ± 0.01	–	–

Self-assembly of PBO_{42}-*b*-PG_{77} (hydrophilic mass ratio f = 65%) led to the formation of pure phases of spherical micelles (Figure 38, Figure 94). Their radius was determined from several TEM images by measuring the surface area of the flattened micelles. The mean radius was then calculated back to be 6.2 ± 1.3 nm (Figure 39). DLS measurements, however, suggested a hydrodynamic radius of 11.2 ± 0.6 nm. The high PDI of 0.40 ± 0.05 could be explained by artefacts of diffusing dust particles as the samples were not filtered before the measurements. The discrepancy between the two radii can be explained by the different measuring techniques: TEM showed flattened self-assemblies due to the applied vacuum, also the automatic calculation of the area was based on contrast between stained micelle and background and thus likely to be inaccurate. In contrast, DLS measurements were based on the diffusion of particles in solution together with their solvating molecules. A higher radius here was

thus expected and conclusive with literature reports.[142,158] In order to compare the measured radii with theoretical numbers, the end-to-end distance R_{coil} in a random coil-like conformation as well as the maximum chain lengths $R_{contour}$ in stretched conformation of the PBO block were estimated. The calculations are shown in the appendix (section 8.1.3). R_{coil} was found to be 2.32 nm, $R_{contour}$ 15.0 nm. The radii determined by DLS and TEM laid between those theoretical values hinting that the PBO chains assembled rather in a stacked elongated than in a random coil-like conformation. Considering these arguments, the measured radii were consistent and in the expected order of magnitude.

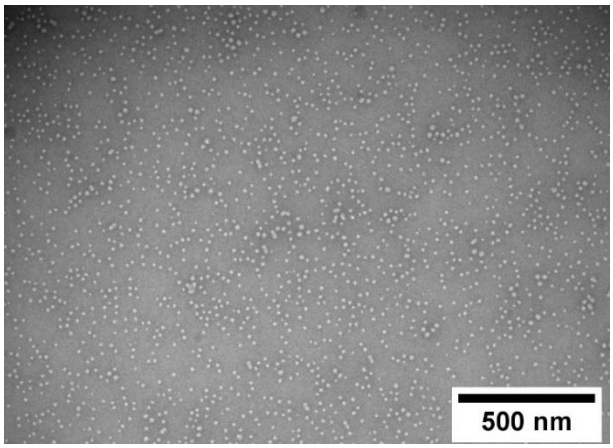

Figure 38: TEM image of the spherical micelles formed by solvent exchange from PBO_{42}-*b*-PG_{77}.

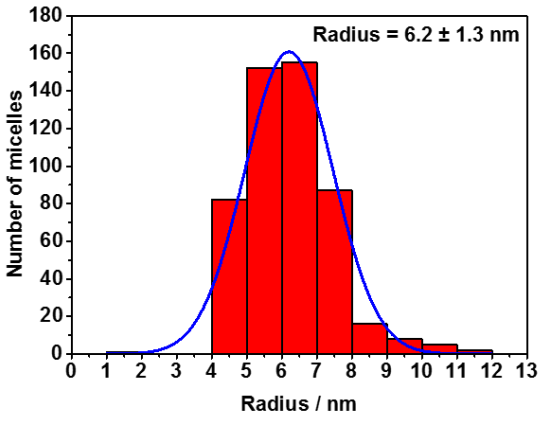

Figure 39: Histogram of the radii distribution of 506 micelles formed by solvent exchange from PBO_{42}-*b*-PG_{77}, measured from TEM images by ImageJ.

The BCP PBO_{42}-*b*-PG_{35} with f = 46% formed pure wormlike phases (Figure 40, Figure 95) with an R_h of 26.0 ± 2.0 nm and a PDI of 0.33 ± 0.02. Several worms were analysed from TEM images, revealing typical worm lengths between 100 and 700 nm and an average worm thickness of 15.9 ± 1.3 nm (Figure 41). The half of this value, 8.0 ± 0.7 nm, corresponded to a monolayer and was hence very much consistent to the radius determined for the micelles. It laid again between the theoretical lengths of the PBO block in a random coil (R_{coil} = 2.32 nm) and in a stretched conformation ($R_{contour}$ = 15.0 nm).

Also here, an elongated chain conformation was assumed, originating from the crowded environment in the membrane.

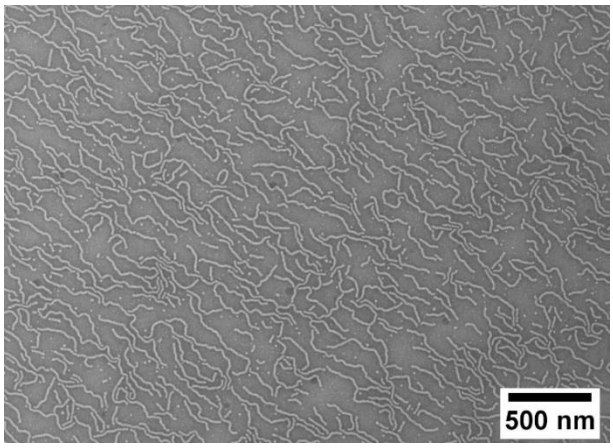

Figure 40: TEM images of wormlike micelles formed by solvent exchange from PBO_{42}-*b*-PG_{35}.

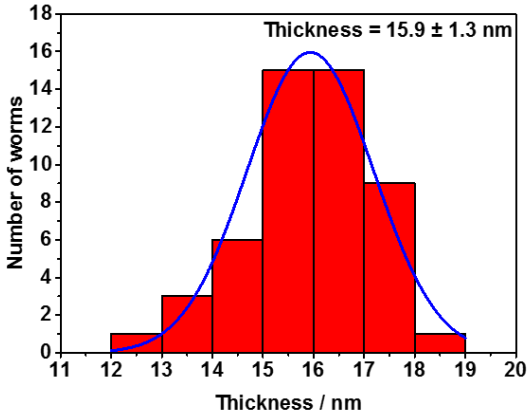

Figure 41: Histogram of the thickness distribution of 50 worms formed by solvent exchange from PBO_{42}-*b*-PG_{35}, measured from TEM images by ImageJ.

SUVs were obtained by the self-assembly of PBO_{42}-*b*-PG_{21} (f = 33%). They were formed in homogenous phases consisting solely of vesicles, but showed a large size polydispersity with a PDI of 0.34 ± 0.01. Typical diameters were between 50 and 700 nm according to TEM and Cryo-TEM images, which proved the formation of SUVs (Figure 42, Figure 43). DLS measurements revealed an R_h of 127 ± 16 nm. In order to confirm the formation of SUVs also by light scattering, SLS measurements were conducted. Following the Mie model, a radius of gyration R_g of 147 nm was calculated (Figure 44). Dividing R_g by R_h led to the particle scattering factor ρ (see section 1.3.6). For the SUVs presented here ρ was determined to be 1.16. Compared to the expected value for vesicular structures of 1.0 this higher value presumably originated from the high polydispersity, which prevented a more accurate assessment of R_g.

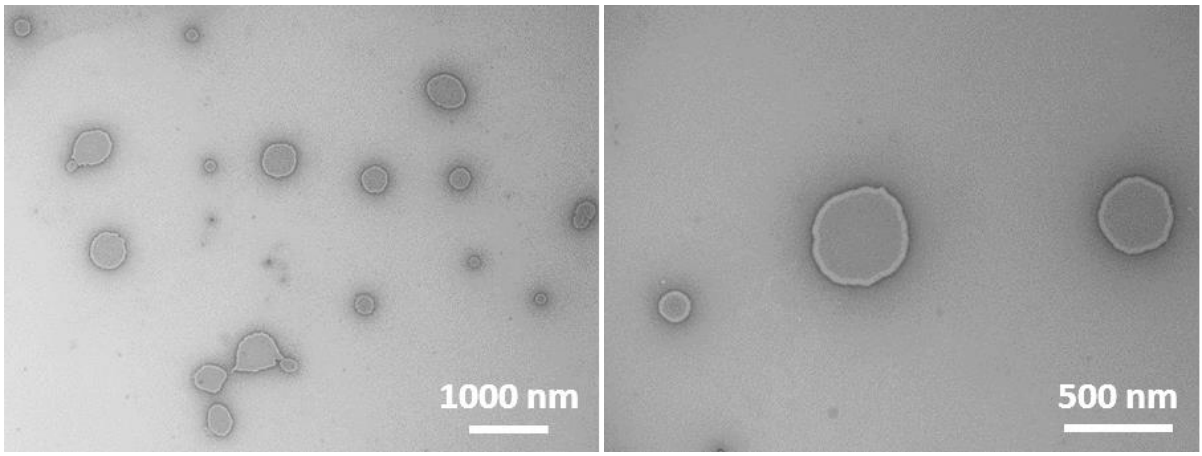

Figure 42: TEM images of SUVs before extrusion formed by solvent exchange from PBO_{42}-*b*-PG_{21}.

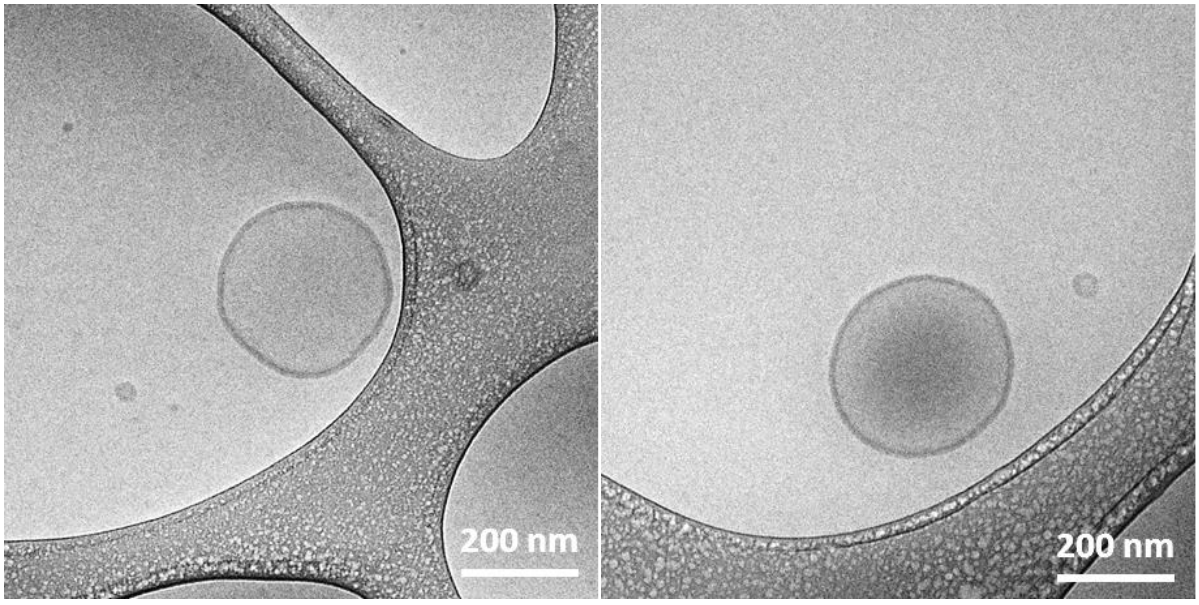

Figure 43: TEM images of SUVs before extrusion formed by solvent exchange from PBO_{42}-*b*-PG_{21}.

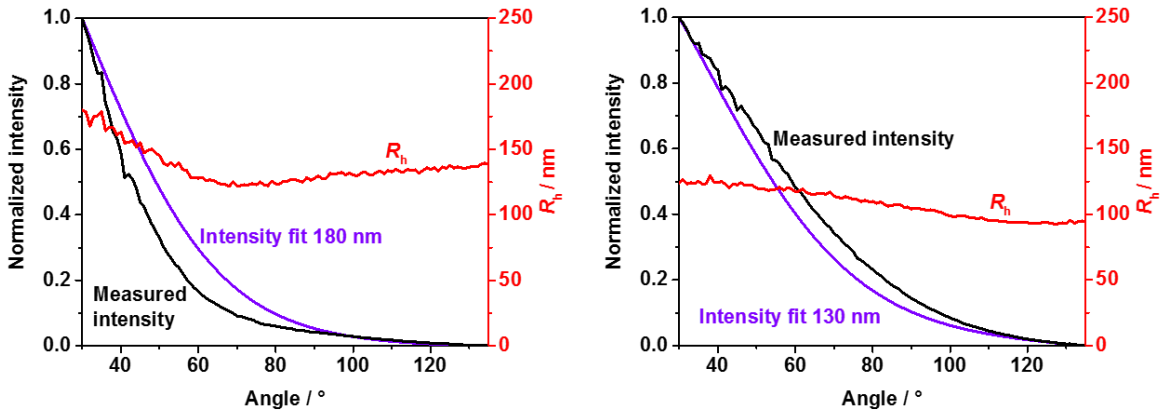

Figure 44: SLS and DLS results for SUVs formed by solvent exchange from PBO_{42}-*b*-PG_{21} before (left) and after (right) extrusion with a 200 nm membrane. The best Mie fits for the measured intensities (black) are shown in violet. When choosing the best fit, the angular range higher than 90 ° was considered as nanoscopic structures are more likely to scatter at higher angles. Also the hydrodynamic radius R_h (red) shows a plateau in this range.

In order to narrow down the size distribution and enable a more reliable characterisation, the sample was extruded through a 200 nm membrane. DLS revealed then an R_h of 108 ± 11 nm with a significantly decreased PDI of 0.15 ± 0.05 and SLS an R_g of 101 nm (Figure 44). The resulting particle scattering factor of ρ = 0.93 indicated the presence of hollow spheres with a thicker membrane, which was expected for SUVs of this size. TEM and Cryo-TEM images were used to confirm the presence of vesiclar structures. They showed homogenous phases with smaller SUVs compared to the images before extrusion (Figure 45, Figure 96). The average diameter and membrane thickness were determined by Cryo-TEM (Figure 46, Figure 97). Measuring several vesicles led to a mean diameter of 258 ± 82 nm. Despite a more uniform appearance after extrusion, the error showed that the sizes were still not completely uniform, ranging from 100 up to 450 nm. The membrane thickness was determined to be 12.5 ± 1.5 nm, measuring in total 200 spots on several SUVs. Half of this value, 6.3 ± 0.8 nm, again corresponded to a monolayer of the PBO block. The measured value was very much consistent with the theoretical numbers for coil-like and stretched conformations, assuming again a stacked elongated chain conformation. Comparing all three radii, the worms showed the most stretched conformation of all BCPs, which could be explained by the crowded environment of a linearly extended self-assembly structure with no curvature in this dimension.

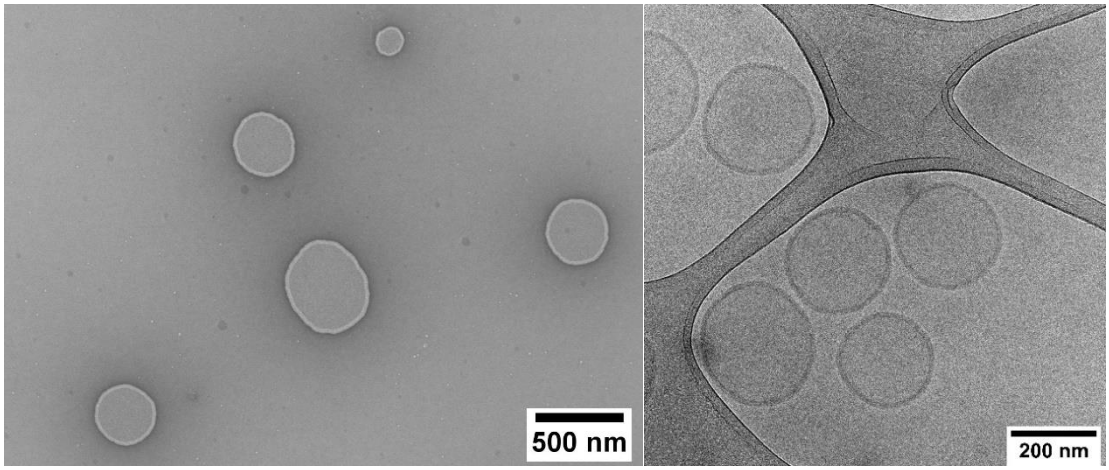

Figure 45: TEM (left) and Cryo-TEM (right) images of SUVs after extrusion with a 200 nm membrane formed by PBO_{42}-*b*-PG_{21}.

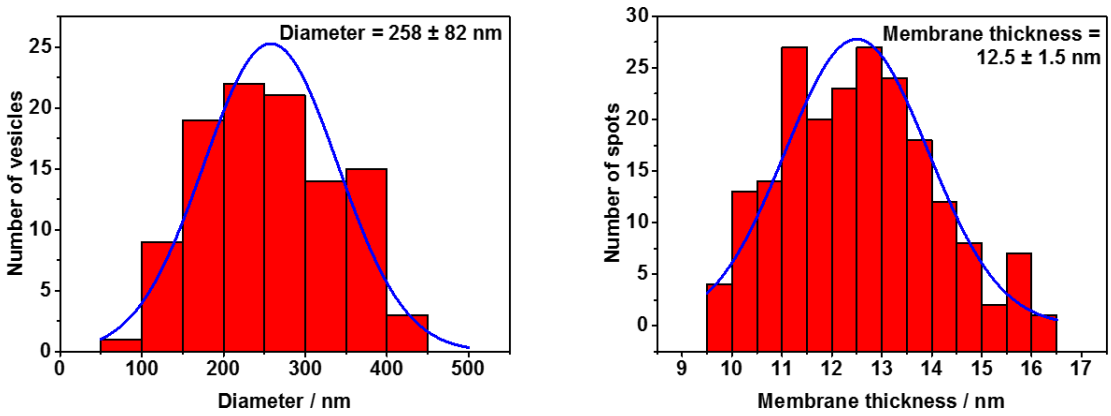

Figure 46: Histogram of the diameter distribution of 104 SUVs (left) and the membrane thickness of 200 spots on several SUVs formed by solvent exchange from PBO_{42}-*b*-PG_{21} and measured from Cryo-TEM images after extrusion with a 200 nm membrane.

In order to enable a use of the SUVs in physiological environment, the self-assembly of PBO_{42}-*b*-PG_{21} was performed not only in water, but also in PBS. Without extrusion, DLS measurements revealed an R_h of 129 ± 15 nm and a PDI of 0.35 ± 0.01; both values were similar to the values obtained in water. SLS confirmed the presence of SUVs with an R_g of 136 nm and a particle scattering factor ρ of 1.05, close to the ideal value of 1.0 for hollow spheres (Figure 47). The difference of R_g and thus ρ compared to water (R_g = 147 nm, ρ = 1.16) was probably caused by the high polydispersity of both samples again disturbing a more accurate determination of the actual values. TEM images also indicated vesicular structures with comparable morphologies and sizes as in water. Only minor aggregates and artefacts inside the flattened SUVs were visible (Figure 48). The latter ones presumably originated from elctrostatic interactions upon drying, caused by salt ions in between the unimers. In summary, both water and PBS seemed equally suitable as dispersion medium.

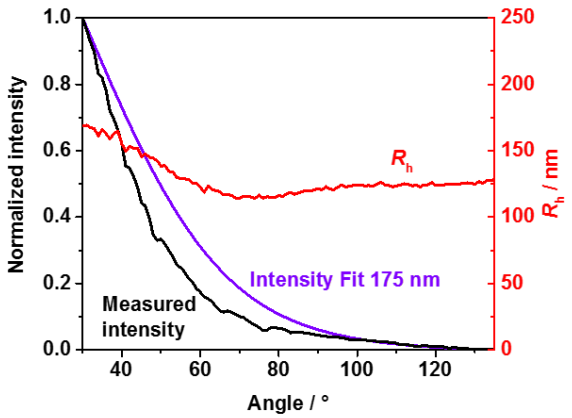

Figure 47: SLS and DLS results of SUVs formed by solvent exchange from PBO_{41}-*b*-PG_{20} in PBS without extrusion.

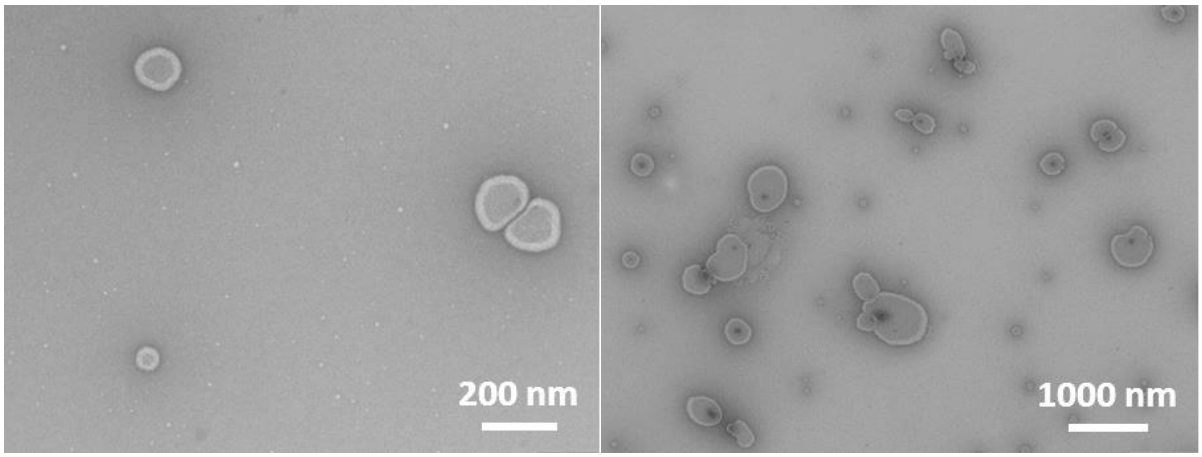

Figure 48: TEM images of SUVs formed by solvent exchange from PBO_{41}-*b*-PG_{20} in PBS without extrusion.

As expected from literature,[143] the morphology of self-assembled structures depended on the solvent used to dissolve the SUV-forming PBO_{42}-*b*-PG_{21}. Several self-assembly tests were run under the same conditions, but using other water-missible organic solvents than THF, which were able to dissolve both blocks: 1,4-dioxane, acetone, methanol, ethanol and isopropanol (Figure 49). Pure vesicular structures were obtained only in the case of THF. All other solvents showed mixed and inhomogenous phases usually consisting of SUVs, micelles, worms or undefined aggregates (Figure 50-Figure 54). It is presumed that the different solvatisation of the BCP during self-assembly as well as the solvent-water interactions determined the conformation of the unimers and curvature of the formed membrane.[211] The preferred vesicular structure governed by the surrounding solvent was apparently only preserved when THF was used, even though the residual solvent was removed afterwards.

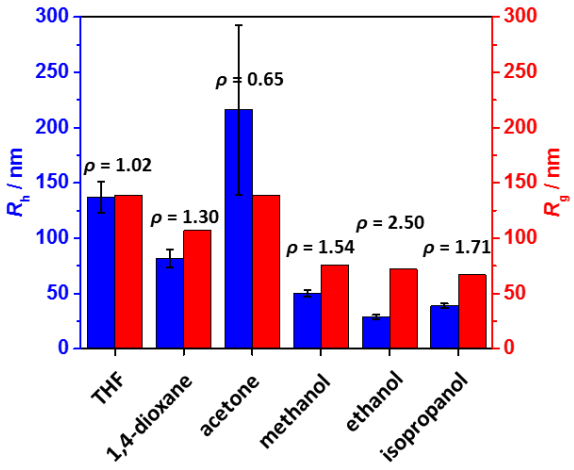

Figure 49: Light scattering results for the self-assemblies formed by solvent exchange from PBO_{42}-*b*-PG_{21} in dependence on different solvents used.

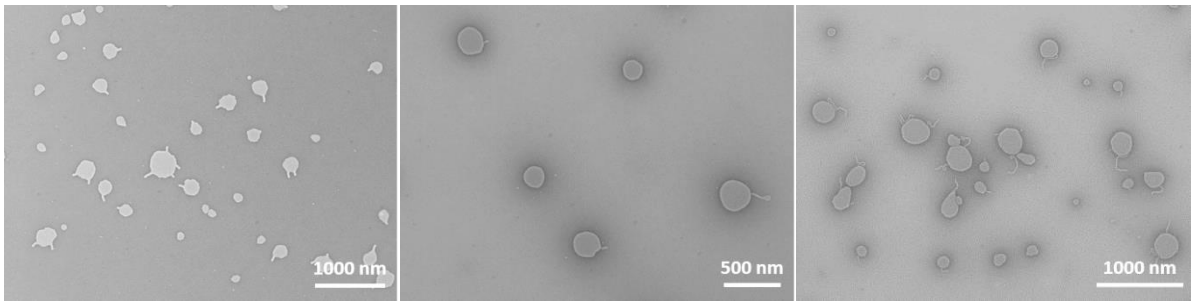

Figure 50: TEM images of the self-assemblies formed by solvent exchange from PBO_{42}-*b*-PG_{21}, dissolved in dioxane.

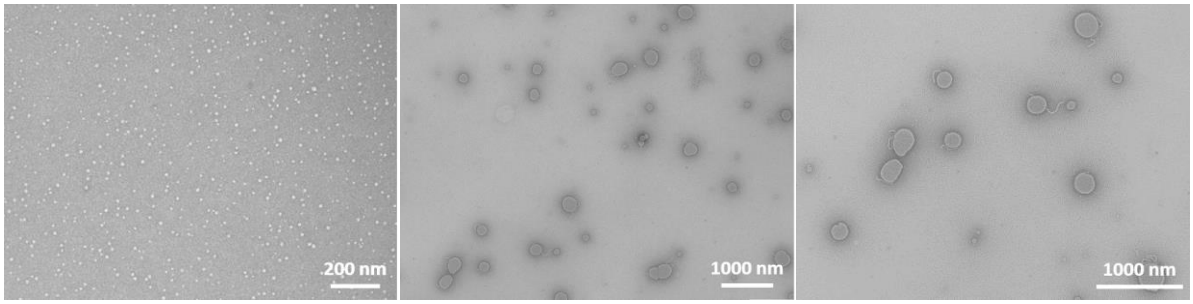

Figure 51: TEM images of the self-assemblies formed by solvent exchange from PBO_{42}-*b*-PG_{21}, dissolved in acetone.

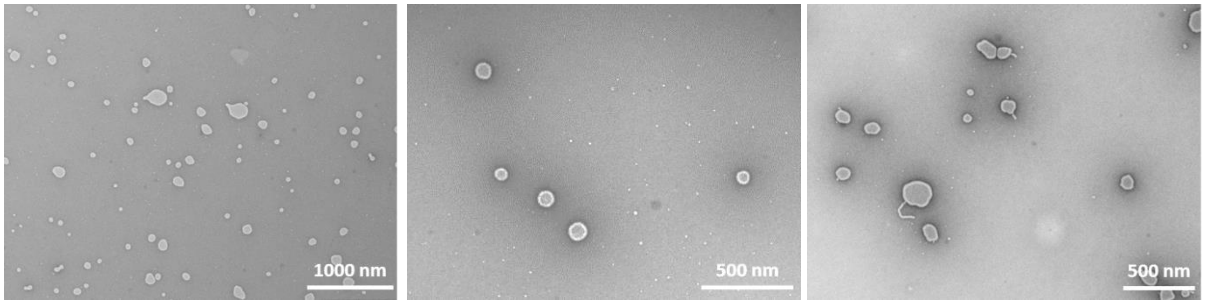

Figure 52: TEM images of the self-assemblies formed by solvent exchange from PBO_{42}-*b*-PG_{21}, dissolved in methanol.

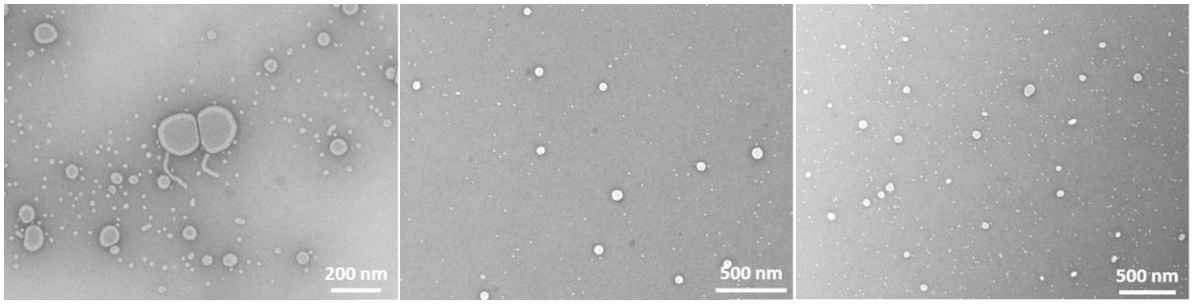

Figure 53: TEM images of the self-assemblies formed by solvent exchange from PBO_{42}-*b*-PG_{21}, dissolved in ethanol.

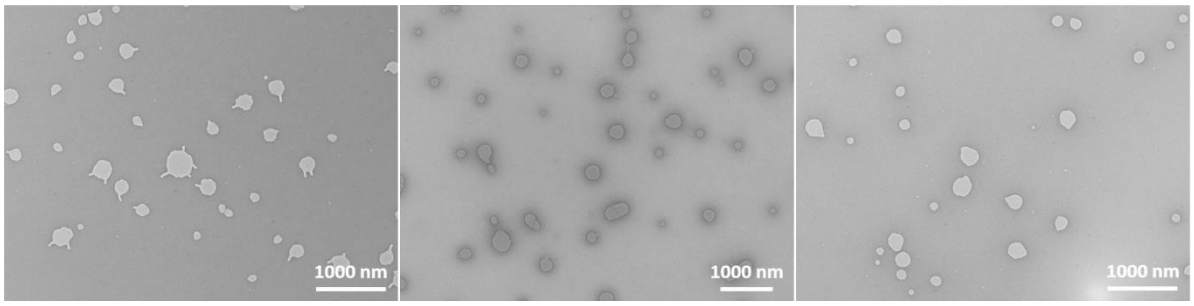

Figure 54: TEM images of the self-assemblies formed by solvent exchange from PBO_{42}-*b*-PG_{21}, dissolved in isopropanol.

Besides SUVs prepared by solvent exchange, the same BCP PBO_{42}-*b*-PG_{21} (f = 33%) was able to form microscopic GUVs by film rehydration. The BCP films were rehydrated with aqueous sucrose solution. Upon dilution with PBS, the GUVs sank down to the bottom of the vial due to the higher density of the sucrose solution in the inside of the GUVs. The isomolarity of sucrose and PBS prevented rupture of the GUVs due to a possible osmotic shock during dilution.[57] The membrane of the GUVs was fluorescently labelled using BODIPY 630/650, a hydrophobic dye which diffused mostly into the hydrophobic core of the polymer membrane, and imaged by CLSM. Mostly GUVs with diameters between 2 and 20 µm were formed, but also multilamellar or multicompartment vesicles or aggregates (Figure 55, Figure 98). These results underlined the broad variety of self-assembly structures that PBO-*b*-PG amphiphilic BCPs were able to form.

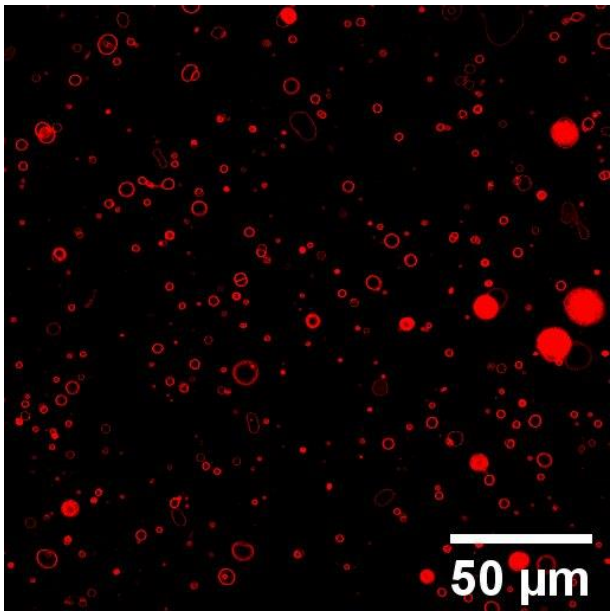

Figure 55: CLSM image of GUVs formed from PBO_{42}-*b*-PG_{21}. The membranes or polymer aggregates were stained with BODIPY 630/650, a hydrophobic, red fluorescent dye.

3.2.2. Discussion of the self-assembly results

The BCPs presented in this work displayed an ideal example of the established self-assembly theory, regarding the correlation between composition, *i.e.* hydrophilic mass fraction *f*, and self-assembled structure.[53,140,141,212] With decreasing *f*-ratio, the transition from micelles (*f* = 65%) over worms (*f* = 46%) to SUVs (*f* = 33%) was observed. The *f* values noted here exactly matched reported target values representating pure phases of micelles (> 45%), worms (< 50%) and vesicles (35% ± 10%).[60] Consequently, BCPs synthesised using adjusted PBO macroinitiators with intermediate *f*-ratios showed mixed phases (Table 6, Figure 56). For example, PBO_{36}-*b*-PG_{59} (*f* = 62%, Figure 57) formed mostly micelles with some worms or elongated micelles. PBO_{30}-*b*-PG_{38} (*f* = 56%, Figure 58) formed a mixed phase with both micelles and worms. Lower hydrophilic ratios than 33% resulted in inhomogenous vesicular phases with dimeric and deformed structures (PBO_{50}-*b*-PG_{18}, *f* = 27%, Figure 59) or solely undefined aggregates (PBO_{67}-*b*-PG_{14}, *f* = 17%, Figure 60). In particular, the comparison of the BCPs with *f* = 62% and *f* = 65% indicated that even small changes in the average composition already led to significant differences in the formed morphology. However, morphological differences between comparable BCP batches could also be explained by the possible presence of small impurities, which could have affected the chain packing during self-assembly. Due to the good control and reproducibility of the polymerisations, it was possible to exactly hit the targeted *f* values in order to systematically scan for the composition which allowed for the formation of the highly homogenous self-assembly phases presented above.

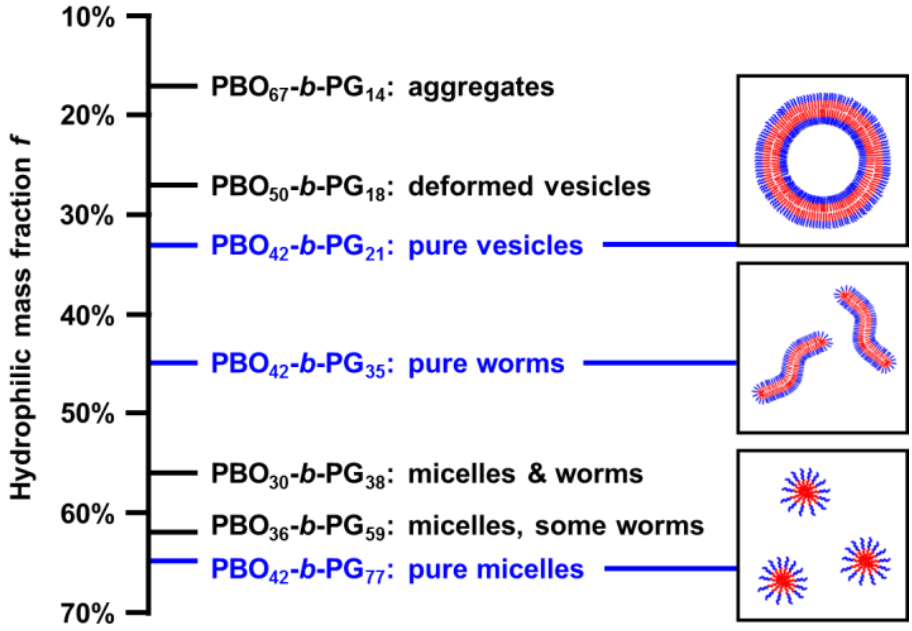

Figure 56: Self-assembly phase diagram of PBO-*b*-PG structures formed by solvent exchange: Depending on the composition and hydrophilic mass fraction *f*, pure or mixed phases are formed. The pure phases (blue) are represented by schematic sketches on the right.

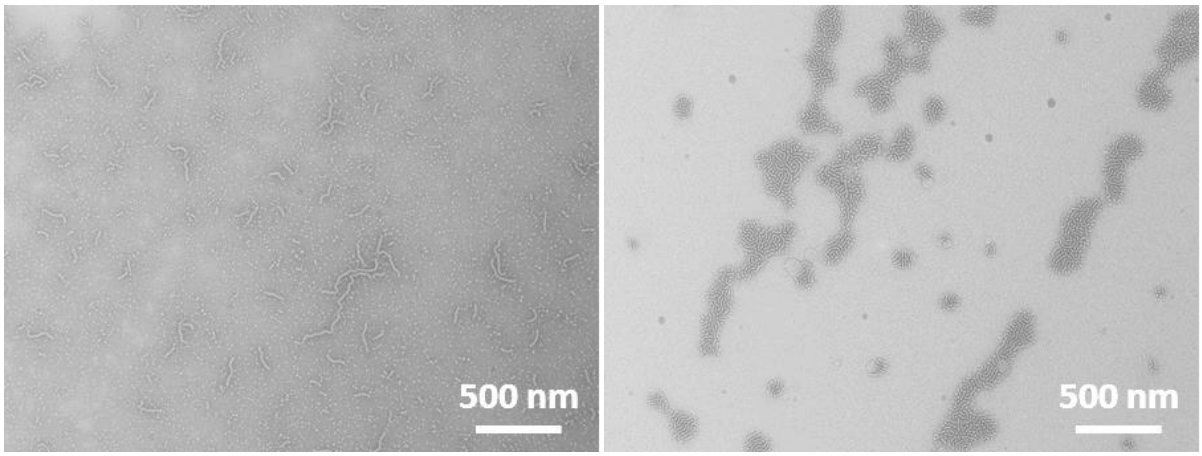

Figure 57: TEM images of the self-assemblies formed by solvent exchange from PBO_{36}-*b*-PG_{59} (f = 62%).

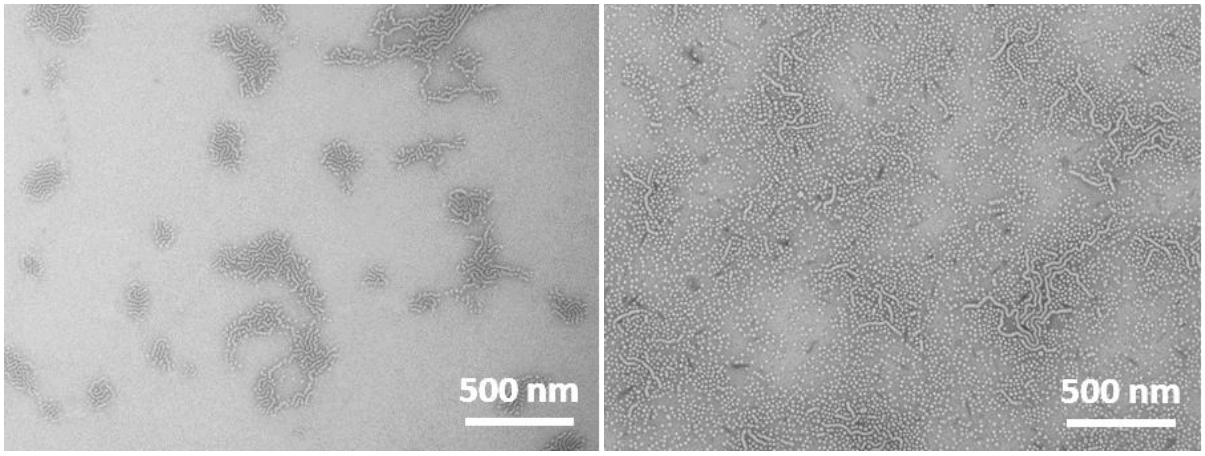

Figure 58: TEM images of the self-assemblies formed by solvent exchange from PBO_{30}-*b*-PG_{38} (f = 56%).

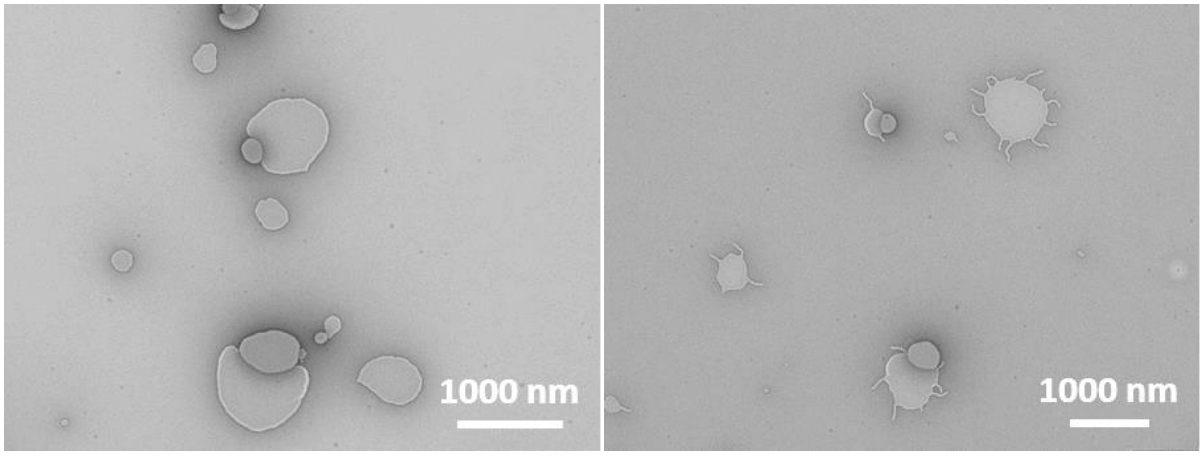

Figure 59: TEM images of the self-assemblies formed by solvent exchange from PBO_{50}-*b*-PG_{18} (f = 27%).

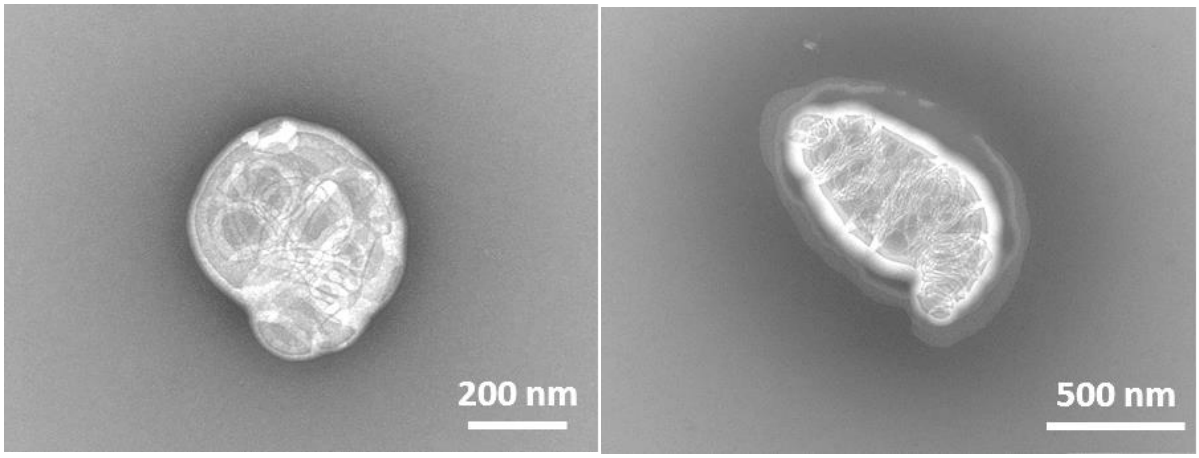

Figure 60: TEM images of the self-assemblies formed by solvent exchange from PBO_{67}-*b*-PG_{14} (*f* = 17%).

The homogeneity of micelles, worms and SUVs underlined the power of solvent exchange as self-assembly method. Both light scattering as well as TEM imaging revealed pure phases without aggregates when BCP composition, solvent and self-assembly protocol were optimised. Self-assembly of the same BCPs by film rehydration led to inhomogenous phases: in case of the vesicle-forming PBO_{42}-*b*-PG_{21} TEM images showed the presence of compound vesicles or polymer films (Figure 61a, Figure 99). These seemed to undergo a transition into vesicular structures, which was, however, not complete. Also micelles formed from PBO_{42}-*b*-PG_{77} (*f* = 65%) by film rehydration were not uniformly distributed, but partly aligned to chain-like structures, indicating an incomplete separation (Figure 61b, Figure 100). Worms in similar morphology, but distincly longer, were obtained from PBO_{42}-*b*-PG_{35} by film rehydration (Figure 61c, Figure 101). Especially in contrast to self-assemblies formed by film rehydration from PBO-*b*-PG diblock and PG-*b*-PBO-*b*-PG triblock copolymers, published by Du *et al*.,[95] the filtration of impurities such as aggregates was not necessary when applying the solvent exchange protocol discussed in here. A comparison of both studies also suggested that self-assembly *via* solvent exchange could make much more use of the defined composition of the BCPs as it led to distinct phases. As mentioned above, small differences in the hydrophilic fraction led to rather big differences in the obtained morphologies, including mixed phases. In case of film rehydration, big differences in the composition seemed to have only a minor effect on the structures formed, as Du *et al*. obtained micelles with hydrophilic block ratios between 49 and 79% and SUVs between 18 and 29%.[95] The latter numbers are rather surprising, as comparable values in the case of solvent exchange only led to impure phases and aggregates. Du *et al*. also observed the formation of mixed cylindrical and vesicular phases for a BCP with a hydrophilic fraction of 40%.[95] This was conclusive with our findings as their stated *f*-ratio was set in between the one presented in here to form vesicles and worms.

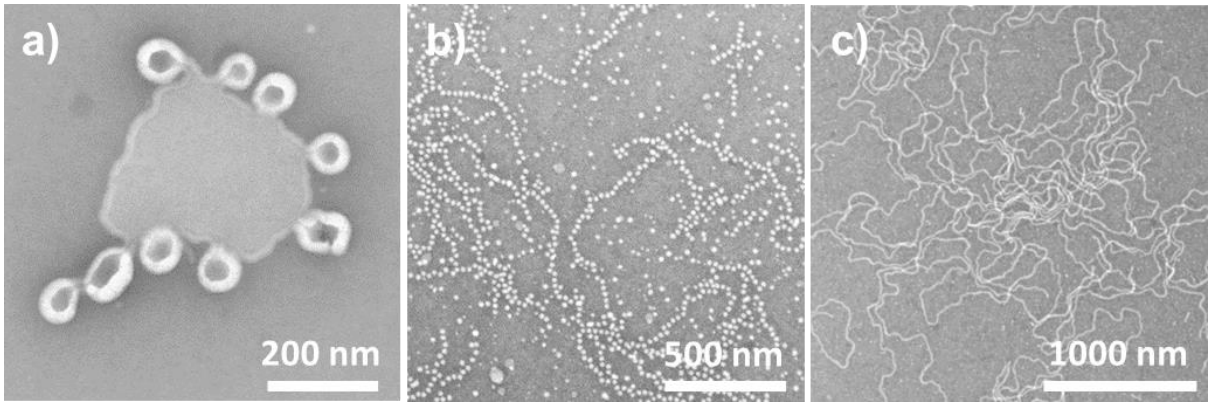

Figure 61: TEM images of the nanoscopic self-assemblies formed by film rehydration from a) PBO_{42}-*b*-PG_{21} (R_h = 713 ± 103 nm, PDI = 0.54 ± 0.39), b) PBO_{42}-*b*-PG_{77} (R_h = 63.3 ± 0.5 nm, PDI = 0.37 ± 0.01), c) PBO_{42}-*b*-PG_{35} (R_h = 68.9 ± 1.0 nm, PDI = 0.43 ± 0.01).

It can be suggested that the differences between the two formation methods were caused by the kinetics during the self-assembly process.[19,143] The following hypothesis suggested: Film rehydration as top-down method did not allow for a sufficient solubilisation of the unimer chains from a bulk material to self-assemble into a well-defined and stable structure. Not every unimer was solely removed from the film, but rather scratched off with surrounding material, leading to kinetically trapped aggregates. In contrast, solvent exchange started from completely dissolved and flexible unimer chains, which were allowed to find a favoured surrounding on a larger time scale due to the slow additon of water. As a bottom-up assembly, it enabled a more distinct morphology which represented the preferred steric surrounding for every unimer chain. This led to pure phases if all conditions were matched, but also to mixed phases for intermediate compositions together with a lower chance of only kinetically frozen aggregates.

3.2.3. Self-assembly of isotactic PBO-*b*-PG into SUVs

The three similar atactic or isotactic BCPs (chapter 3.1.3 and 3.1.4) were subjected to the optimised solvent exchange protocol established for atactic PBO-*b*-PGs (chapter 3.2.1). After self-assembly in PBS, the structures were characterised using a combination of DLS, SLS, NTA, TEM and Cryo-TEM. Extrusion finally led to small and narrowly distributed SUVs.

Before extrusion, TEM imaging revealed the presence of round shaped self-assemblies for all BCPs (Figure 62), indicating vesicular morphologies. Although a high variation in their sizes was observed, homogenous phases with few aggregates and micelles were obtained. DLS and SLS were employed to confirm the presence of SUVs (Table 7). The sizes of all self-assemblies of the three BCPs were in a similar range with hydrodynamic radii (R_h) between 73 nm and 98 nm. The R_h values decreased only slightly over the whole angle range, indicating homogenous phases and low polydispersities (Figure

120-Figure 122). Radii of gyration (R_g) between 89 nm and 97 nm were of a similar magnitude as the R_h values (Table 7). Values of the particle scattering factor ρ of 0.91 for the (*R*/*S*)-BCP, 1.29 for the (*R*)-BCP and 1.01 for the (*S*)-BCP confirmed the presence of hollow vesicles. The deviation of the calculated values from the ideal value of 1.0 could be attributed to the lack of extrusion, the polydispersity (PDIs around 0.25 for all BCPs self-assemblies) and that the average size was just in-between the Guinier and Mie regimes, preventing a more accurate determination of R_g. Every BCP was subjected to several repetition runs, where the radii typically varied by ± 20 nm, indicating that the SUVs of all three BCPs were formed reproducibly in comparable sizes, independently of their configuration.

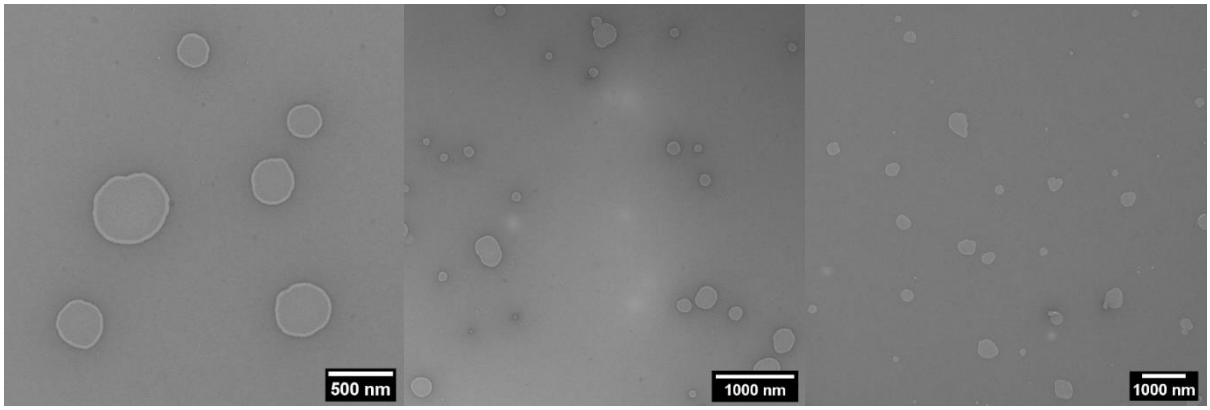

Figure 62: TEM images of SUVs composed of the (*R*/*S*)-BCP (left), the (*R*)-BCP (middle) and the (*S*)-BCP (right) before extrusion.

Table 7: Characterisation of the nanoscopic self-assemblies before and after extrusion with a 100 nm membrane. Values determined by (a) DLS, (b) SLS, (c) NTA. (d) Membrane thickness *l* determined by Cryo-TEM.

extrusion	polymer	R_h[a] / nm	PDI[a]	R_g[b] / nm	$\rho = R_g$[b] / R_h[a]	R_h[c] / nm	morphology	*l*[d] / nm
–	(*R*/*S*)-BCP	98 ± 16	0.26 ± 0.05	89 ± 5	0.91 ± 0.16	–	SUV	–
–	(*R*)-BCP	73 ± 8	0.26 ± 0.03	94 ± 3	1.29 ± 0.14	–	SUV	–
–	(*S*)-BCP	96 ± 15	0.25 ± 0.05	97 ± 5	1.01 ± 0.17	–	SUV	–
100 nm	(*R*/*S*)-BCP	59 ± 2	0.26 ± 0.05	64 ± 5	1.08 ± 0.09	56 ± 11	SUV	11.1 ± 0.8
100 nm	(*R*)-BCP	49 ± 3	0.24 ± 0.04	53 ± 8	1.08 ± 0.17	48 ± 11	SUV	11.6 ± 0.9
100 nm	(*S*)-BCP	64 ± 2	0.22 ± 0.04	69 ± 3	1.08 ± 0.06	63 ± 10	SUV	11.0 ± 1.0

After extrusion through a 100 nm membrane, TEM images indicated the presence of smaller SUVs with diameters between 50 and 200 nm in homogenous phases (Figure 63). The size variation of the SUVs had visually decreased compared to the SUVs before extrusion. According to DLS and SLS, the sizes of the SUVs were reduced to radii (R_h and R_g) between 49 and 68 nm (Table 7, Figure 123-Figure 125). The lower measurement errors after extrusion indicated that the homogeneity was increased. The PDIs, however, decreased only negligibly to values between 0.22 and 0.26. The shape parameter remained with ρ = 1.08 for all three BCPs in a range typical for vesicular structures. In addition, NTA measurements were performed to confirm the size distributions (Figure 64). In all cases, monomodal distributions with mean R_h values between 48 and 63 nm were obtained, being perfectly in line with the

DLS results (Table 7). Cryo-TEM imaging (Figure 65) again confirmed the presence of SUVs and allowed for the determination of the membrane thicknesses *l*. For all BCPs, SUVs with diameters between 45 and 200 nm were observed. The membrane thicknesses were determined to be 11.1 ± 0.8 nm for the (*R*/*S*)-BCP, 11.6 ± 0.9 nm for the (*R*)-BCP and 11.0 ± 1.0 nm for the (*S*)-BCP (Table 7). Besides some spherical micelles (Figure 66), no other morphologies were visible, highlighting the high reproducibility and similarity of all BCP SUVs in terms of size, shape and membrane thickness. Considering the measured membrane thickness and the contour length in a hypothetical stretched conformation as well as the end-to-end distance in an ideal random coil, the degree of the stretching of the PBO block could be calculated (section 8.2.4). Accordingly, in the (*R*/*S*)-BCP PBO was 51% stretched, which is a higher value than observed for more hydrophobic polymers, suggesting less intercoiling within the membrane.[6]

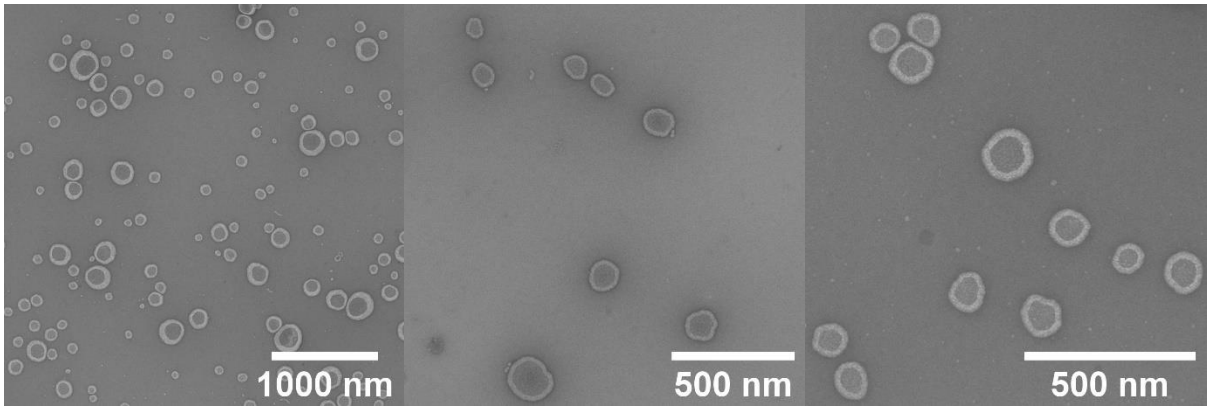

Figure 63: TEM images of SUVs composed of the (*R*/*S*)-BCP (left), the (*R*)-BCP (middle) and the (*S*)-BCP (right) after extrusion with a 100 nm membrane.

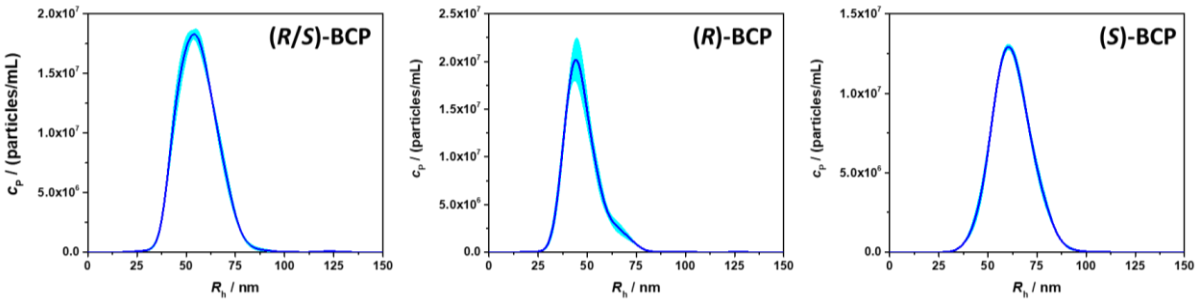

Figure 64: Size distribution of the SUVs composed of the atactic and isotactic BCPs, measured by NTA.

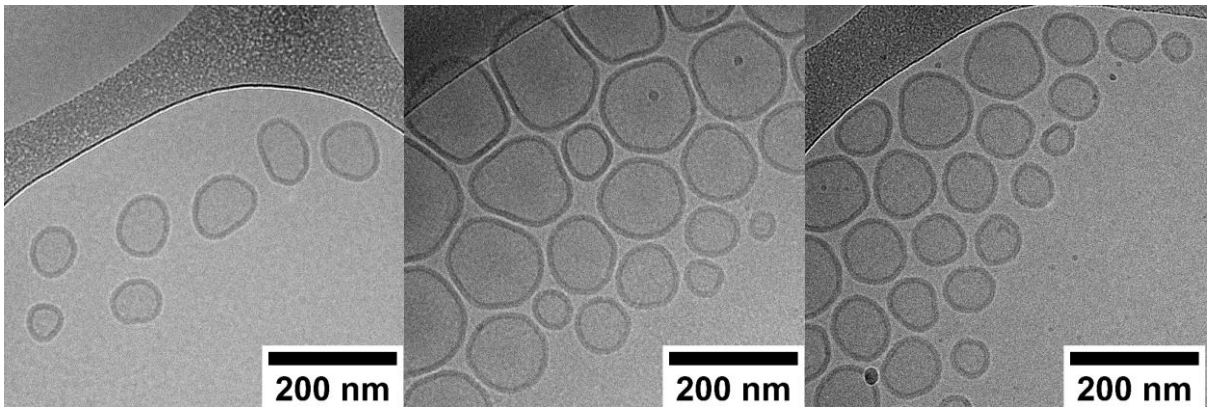

Figure 65: Cryo-TEM images of SUVs composed of the (*R*/*S*)-BCP (left), the (*R*)-BCP (middle) and the (*S*)-BCP (right) after extrusion with a 100 nm membrane.

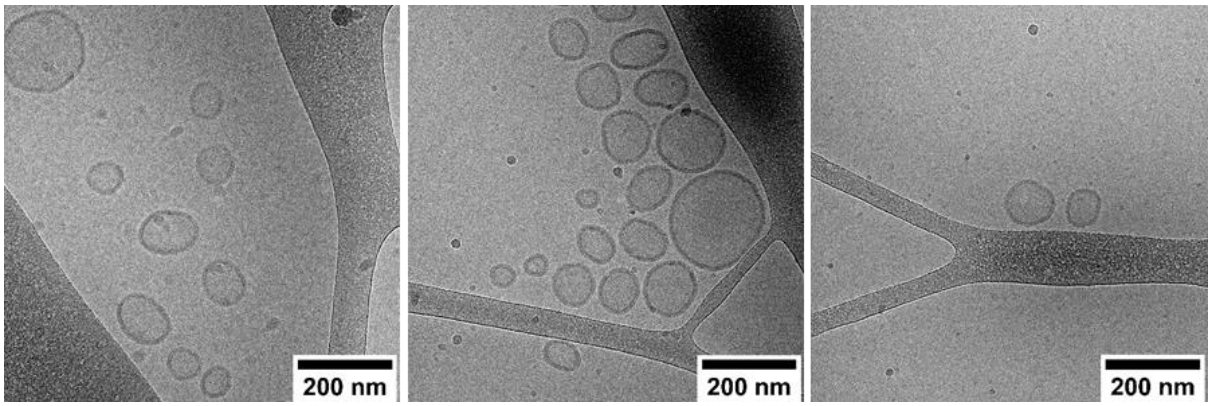

Figure 66: Cryo-TEM images of (*R*/*S*)-PBO_{26}-*b*-(*R*/*S*)-PG_{14} SUVs (left), (*R*)-PBO_{26}-*b*-(*R*)-PG_{14} SUVs (middle) and (*S*)-PBO_{27}-*b*-(*S*)-PG_{14} SUVs (right), showing SUVs and micelles.

SUVs of the (*R*/*S*)-BCP and (*S*)-BCP remained stable for at least one week at room temperature. In contrast, SUVs composed of the (*R*)-BCP ruptured and formed wormlike aggregates to a small extent (Figure 67). Due to the structural similarity of the BCPs, this instability hinted towards a correlation between the partial loss of long-term stability and the (*R*) configuration of the BCP. However, it cannot be ascribed to it unequivocally. Hence, it is assumed that SUVs composed of the (*R*)-BCP were not fully at thermodynamic equilibrium.[143]

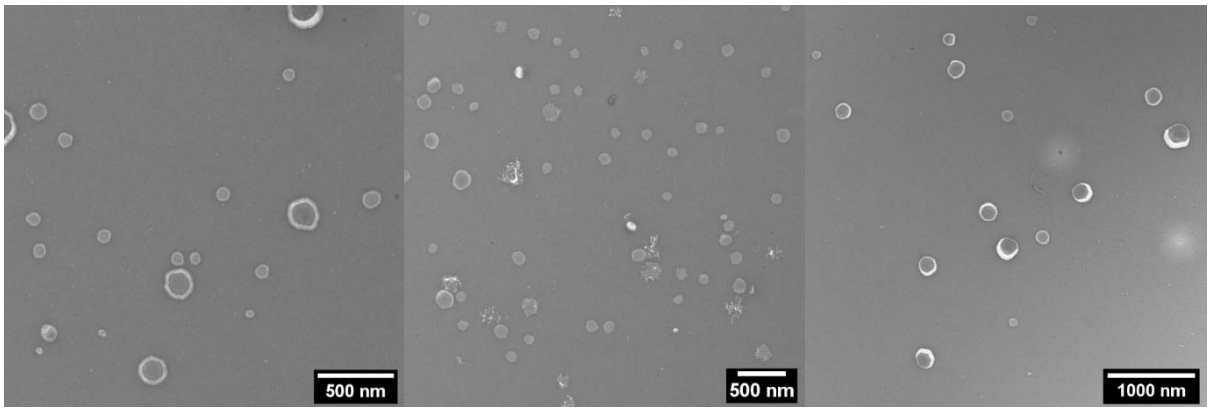

Figure 67: TEM images of (*R*/*S*)-PBO$_{26}$-*b*-(*R*/*S*)-PG$_{14}$ SUVs (left), (*R*)-PBO$_{26}$-*b*-(*R*)-PG$_{14}$ SUVs and aggregates (middle) and (*S*)-PBO$_{27}$-*b*-(*S*)-PG$_{14}$ SUVs (right) after 7 days at room temperature.

3.2.4. GUVs of isotactic PBO-*b*-PG by double emulsion microfluidics

To elucidate the ability of all three BCPs to form microscopic GUVs, a microfluidics-based approach was chosen. Compared to film rehydration,[109,178,179] GUVs formed by double emulsion microfluidics promise higher reproducibility, size uniformity and encapsulation efficiency.[125,156] The detailed description of the used microfluidics device, as well as the general concept of this method can be found elsewhere.[125] In order to prevent vesicle rupture upon evaporation of the organic solvents, optimising the contents and fluid properties (*e.g.* viscosity and density) of the inside and outside of GUVs was essential (section 5.4.2).[125]

GUVs were imaged by CLSM and exemplary micrographs of the GUVs composed of all three BCPs are shown in Figure 68a-c. The GUVs were formed in a high homogeneity with similar sizes: for the (*R*/*S*)-BCP a GUV diameter of 39.5 ± 0.5 µm was determined, for the (*R*)-BCP 37.3 ± 1.0 µm and for the (*S*)-BCP 35.4 ± 0.7 µm. Small deviations were due to necessary slight variations in the optimal flow rate. To improve the visualisation the hydrophobic dye BODIPY 630/650 was added after GUV formation. As the dye was also soluble in PBS, not only the hydrophobic membrane but also the background appeared red (Figure 68). The lumen of all GUVs remained dark and indicated the successful formation of impermeable GUVs. Differences between the three BCPs were found regarding the time needed for the formation of GUVs from double emulsions and the stability of GUVs. Less than 30 min were required for the (*R*/*S*)-BCP and the (*R*)-BCP to form GUVs. In contrast, double emulsions formed by the (*S*)-BCP were present even after three hours. While multiple (*R*/*S*)-BCP GUVs were stable over several hours, the majority of GUVs composed of the (*R*)- and (*S*)-BCPs disassembled within some minutes upon evaporation of the organic solvents. Consequently, only few GUVs of these BCPs were visible in the CLSM images Figure 68b and c.

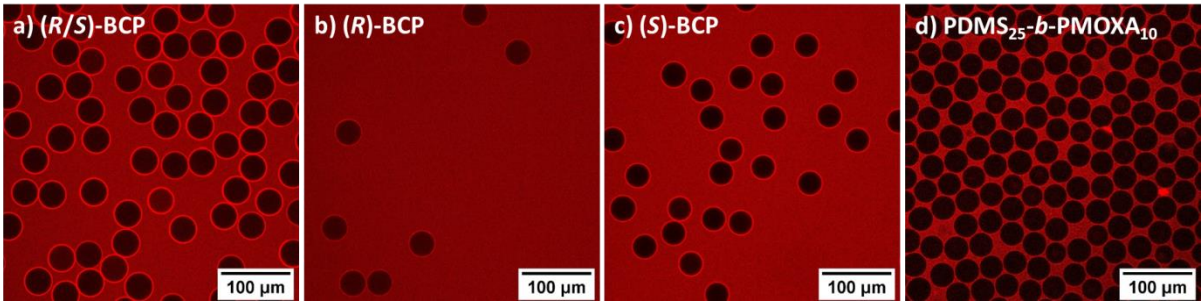

Figure 68: CLSM images of GUVs composed of a) (*R*/*S*)-PBO$_{26}$-*b*-(*R*/*S*)-PG$_{14}$, b) (*R*)-PBO$_{26}$-*b*-(*R*)-PG$_{14}$, c) (*S*)-PBO$_{27}$-*b*-(*S*)-PG$_{14}$ and d) PDMS$_{25}$-*b*-PMOXA$_{10}$ formed by double emulsion microfluidics. The red fluorescent dye BODIPY 630/650 was added after GUV formation and stained the membrane and the background, but not the lumen of the GUVs.

As a comparison for the GUV stability, GUVs composed of PDMS$_{25}$-*b*-PMOXA$_{10}$ of similar molecular weight (2850 g/mol, $Đ$ = 1.19, f = 30%, chapter 3.1.5) were produced. PDMS-*b*-PMOXA based BCPs represent the gold standard for the fabrication of SUVs and GUVs[107,109] and have recently been shown to form stable and impermeable GUVs by microfluidics.[125] GUVs composed of PDMS$_{25}$-*b*-PMOXA$_{10}$ and stained with BODIPY 630/650 are shown in Figure 68d. The diameter was similar to PBO-*b*-PG GUVs and determined to be 34.7 ± 1.7 µm. In contrast to the PBO-*b*-PG GUVs only a negligible number of PDMS-*b*-PMOXA GUVs ruptured during formation or within the next days, explaining the high concentration of GUVs in Figure 68d. The lower stability of PBO-*b*-PG GUVs was in line with the high degree of stretching of PBO within the membrane, resulting in less intercoiling that could stabilise the membrane. Increasing the membrane thickness could have improved the stability, but would have hindered the desired membrane protein insertion (chapter 3.3).[108]

3.2.5. Self-assembly of PDMS-*b*-PMOXA

Nanoscopic self-assembly of the PDMS$_{25}$-*b*-PMOXA$_{10}$ was performed by film rehydration (Figure 7). A thin BCP film was deposited and subsequently rehydrated overnight with PBS. A uniform turbidity of the sample without precipitating aggregates indicated the presence of stable dispersions even after several weeks. The self-assemblies were analysed by DLS before extrusion. An average R_h of 651 ± 298 nm was obtained. High R_h variations over the whole angle range confirmed the high polydispersity of 0.49 ± 0.01 (Figure 69).

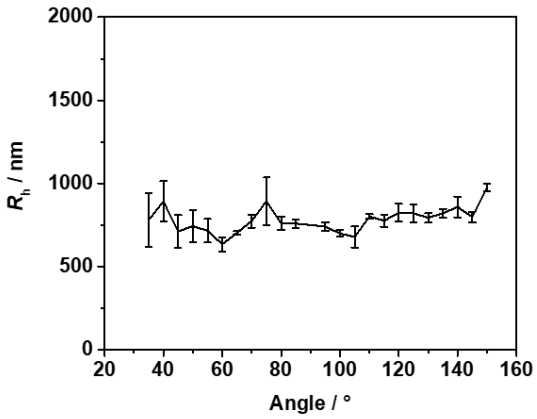

Figure 69: Angle-dependence of the hydrodynamic radius, measured by DLS, of self-assemblies from $PDMS_{25}$-*b*-$PMOXA_{10}$ before extrusion.

After extrusion with a 100 nm membrane, the self-assemblies were characterised by DLS, SLS, NTA, TEM and Cryo-TEM. DLS revealed a decreased R_h of 67 ± 1 nm, SLS an R_g of 78 ± 3 nm (Figure 70). The particle scattering factor ρ was determined to be 1.16 ± 0.05. Its deviation from the expected value of 1.0 for vesicular structures can be explained by the inaccurate determination of R_g, as the size of the self-assembly was in between the Guinier and Mie regimes. The low size variation in the DLS profile over the whole angle range indicated a decreaded polydispersity and was in line with the measured, low PDI of 0.17 ± 0.05. NTA was employed to visualise the size distribution of the self-assemblies (Figure 71). A monomodal distribution with an average R_h of 62 ± 12 nm was determined, which was in good agreement to the DLS measurements.

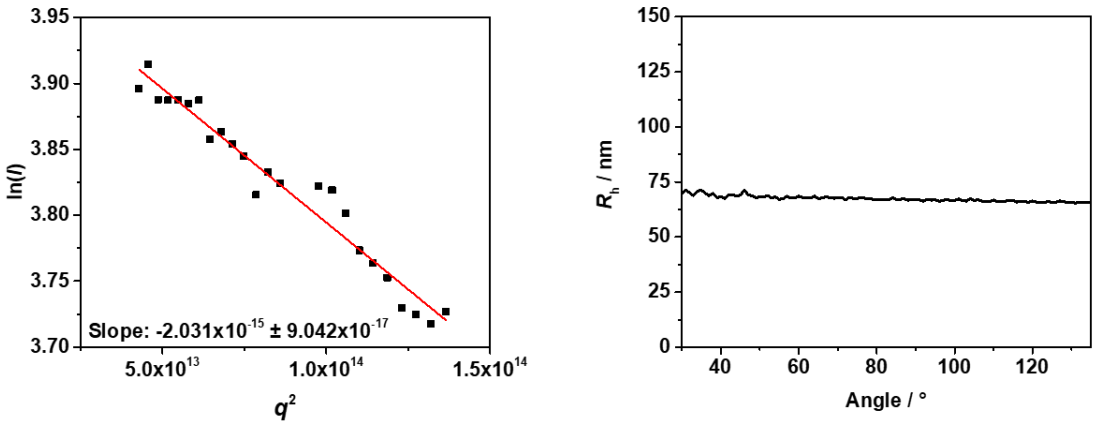

Figure 70: SLS (Guinier model) and DLS results of $PDMS_{25}$-*b*-$PMOXA_{10}$ SUVs after extrusion with a 100 nm membrane.

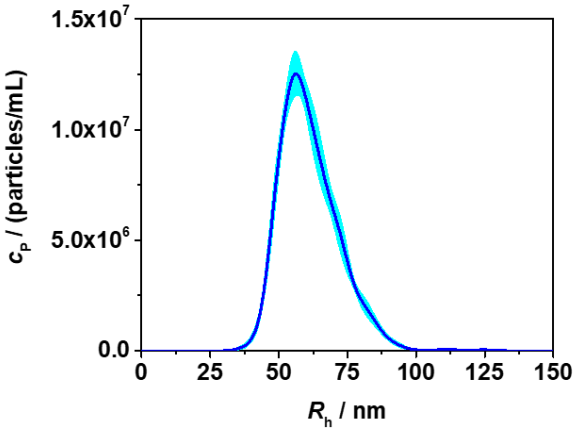

Figure 71: Size distribution of $PDMS_{25}$-*b*-$PMOXA_{10}$ SUVs after extrusion with a 100 nm membrane, measured by NTA.

TEM images of the self-assemblies showed the presence of round-shaped SUVs with apparent diameters between 20 and 300 nm (Figure 72). The bigger particles showed wrinkles and corresponded to deflated SUVs, as proved by comparison to published TEM images.[110,111] The particles below 50 nm were expected to be spherical micelles. The final confirmation of the presence of SUVs was obtained by Cryo-TEM. There, mostly round-shaped SUVs were visible, additionally some micelles and tubular assemblies (Figure 72). The membrane thickness was determined to be 12.0 ± 0.8 nm. The versatility of this $PDMS_{25}$-*b*-$PMOXA_{10}$ was shown elsewhere by reconstituting the membrane protein OmpF in its SUV membrane and encapsulating the bioluminescent enzyme luciferase inside its lumen.[107]

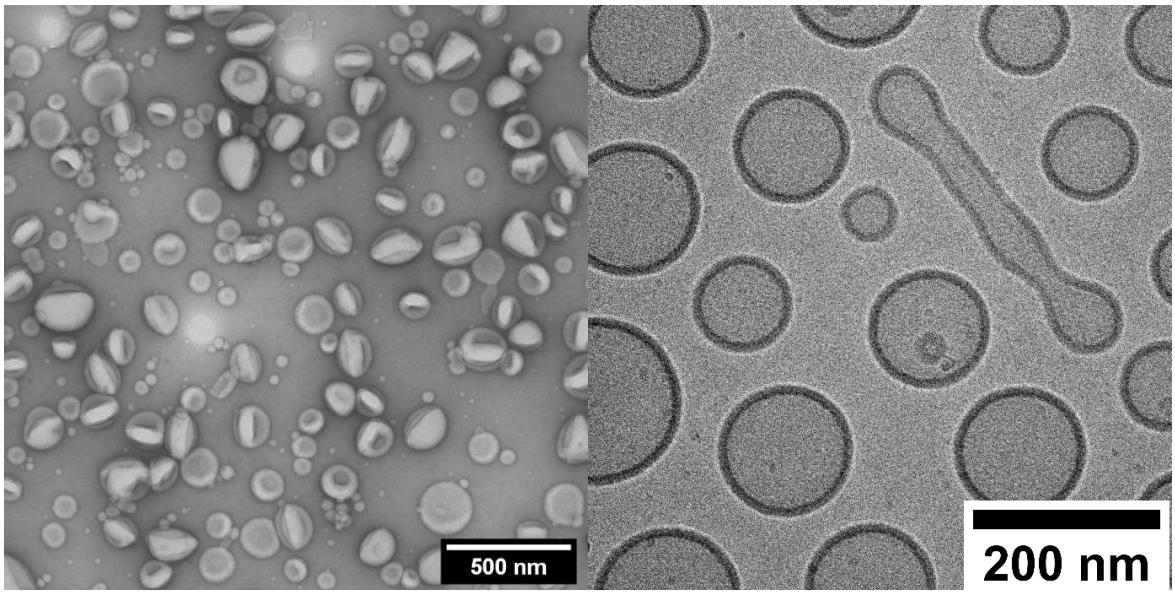

Figure 72: TEM (left) and Cryo-TEM (right) images of $PDMS_{25}$-*b*-$PMOXA_{10}$ SUVs after extrusion with a 100 nm membrane.

The same BCP was used to create microscopic GUVs by film rehydration. CLSM was employed to visualise GUVs stained with BODIPY 630/650. GUVs with diameters between 10 and 30 µm were

obtained (Figure 73). Some aggregates and multicompartment vesicles were visible as well. Compared to GUVs prepared from PBO_{42}-*b*-PG_{21} (Figure 55), the PDMS-*b*-PMOXA-based GUVs possessed about 5-10 times larger diameters and significantly less aggregates and multicompartment vesicles were visible.

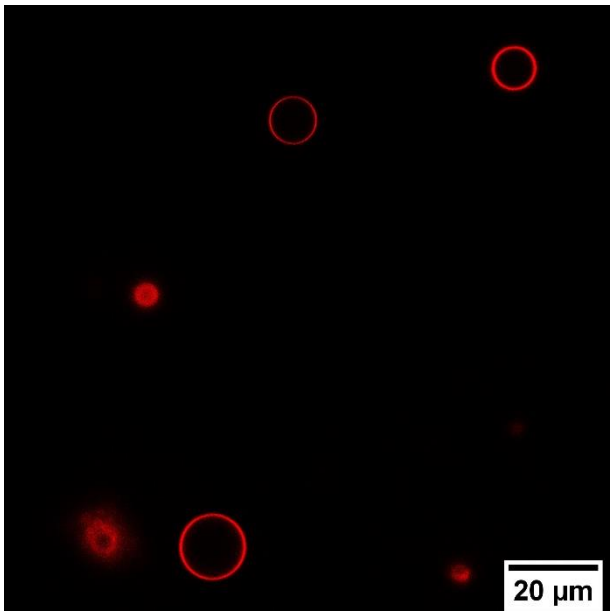

Figure 73: CLSM images of GUVs formed by $PDMS_{25}$-*b*-$PMOXA_{10}$.

3.2.6. Conclusion

In this chapter, the self-assembly of atactic PBO-*b*-PG BCPs with different compositions was presented. A library of several BCPs allowed for a systematic investigation which hydrophilic mass fraction was necessary to favour the self-assembly into homogeneous phases of SUVs, worms and spherical micelles. The self-assembly protocol was optimised by comparing different formation methods. This led to the conclusion that solvent exchange is the method of choice to prepare well-controlled PBO-*b*-PG-based nanoparticles. With this, the basis for the following investigation of the effect of stereoregularity on PBO-*b*-PG self-assemblies was set. Subjecting three highly similar atactic and isotactic BCPs to the previously established self-assembly protocol led to homogenous phases of nanoscopic SUV. The only difference observed between the self-assemblies composed of atactic and isotactic BCPs was a decreased long term stability of the (*R*)-BCP, which could be, but is not necessarily, the result of its configuration. GUVs composed of atactic and isotactic PBO-*b*-PG were obtained by a film rehydration protocol or by double emulsion microfluidics. The latter one allowed to asses highly similar GUVs in terms of size and shape. Additionally, SUVs and GUVs based on PDMS-*b*-PMOXA were prepared by film rehydration and double emulsion microfluidics.

3.3. Membrane protein reconstitution and enzyme reaction

In this chapter, the functional reconstitution of the outer membrane protein F (OmpF) will be proven by performing an enzyme reaction within the lumen of atactic PBO-*b*-PG GUVs. These results will eventually be compared to microreactors composed of PDMS-*b*-PMOXA.

The formation of GUVs (chapter 3.2.4) set the basis to prove the functional reconstitution of a membrane protein in PBO-*b*-PG membranes. Previously, the microfluidics-based approach allowed to analyse cascade reactions within GUVs equipped with membrane proteins.[125] Here, an adapted and simplified approach was employed. OmpF from *E. coli* was chosen as exemplary membrane channel porin, since it allowes the passage of molecules up to 600 Da[165] and has been reconstituted in various studies in PDMS-*b*-PMOXA SUV and GUV membranes.[107,125] As proof of concept, a model enzyme reaction based on the enzyme β-galactosidase (β-Gal) was performed (Figure 74). β-Gal cleaves the non-fluorescent substrate resorufin β-D-galactopyranoside (RGP) into D-galactose and the fluorescent dye resorufin.[175] β-Gal was added to the inner aqueous phase (IA) and encapsulated inside the GUVs. For creating the microreactor, OmpF was added to the outer aqueous phase (OA) during double emulsion formation. The negative control was run using similar IA and OA compositions but without OmpF. After GUV formation, proteinase K was added to deactivate released β-Gal, originating from a significant amount of GUVs rupturing during formation, before RGP addition or during the two hours of the experiment. Subsequently, RGP was added and the fluorescence development was recorded in a time lapse of two hours by CLSM. Due to the instability of GUVs formed by the isotactic BCP, it was only possible to run this experiment for the atactic (*R*/*S*)-BCP. Snapshots of the videos after every 30 min are displayed in Figure 75.

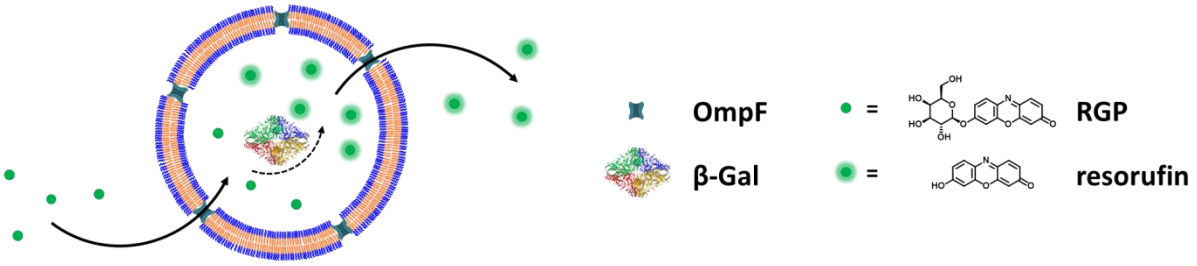

Figure 74: Schematic representation of the reaction of β-galactosidase (β-Gal) with resorufin β-D-galactopyranoside (RGP) inside OmpF equipped GUVs (microreactors) to yield the fluorescent dye resorufin. The dye accumulates within the cavity and over time diffuses out of the GUV through the OmpF pores.

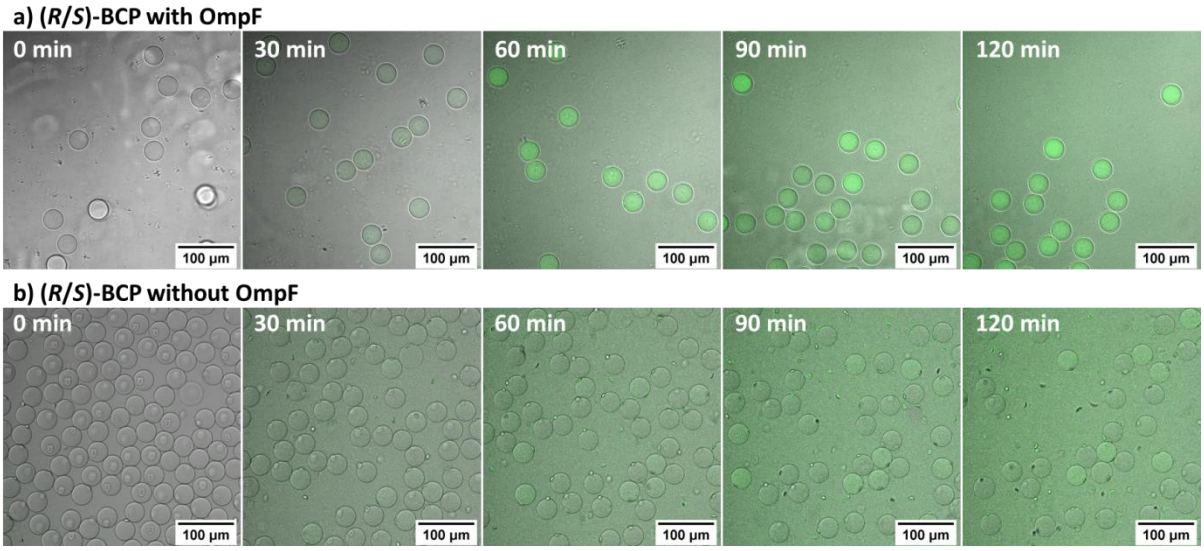

Figure 75: Snapshots of the enzyme reaction within the cavity of (*R*/*S*)-BCP GUVs a) with and b) without reconstituted membrane protein OmpF, recorded by CLSM at different time points.

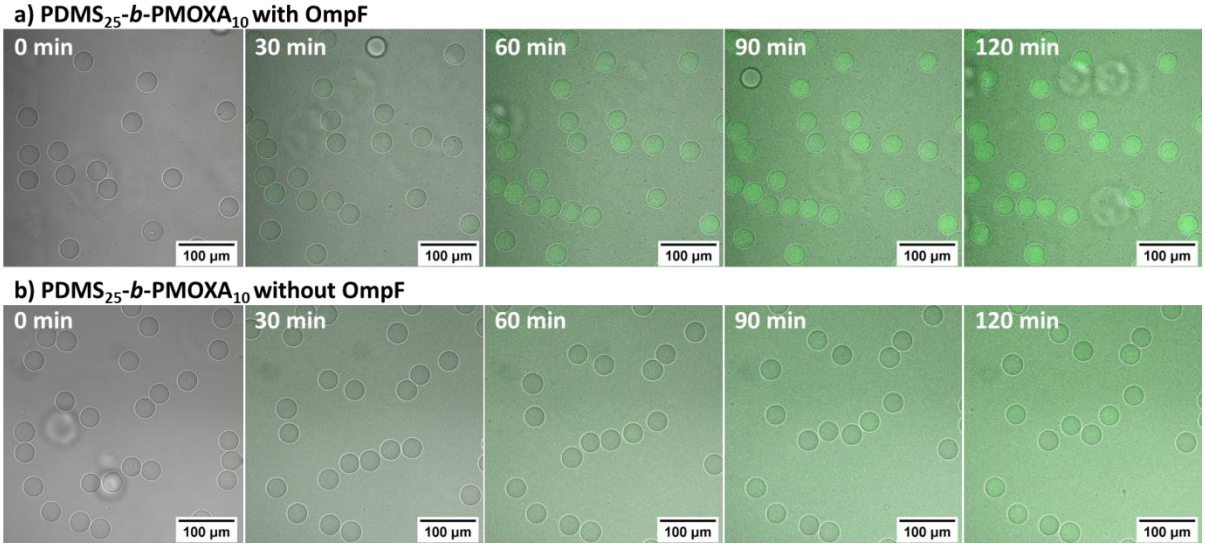

Figure 76: Snapshots of the enzyme reaction within the cavity of $PDMS_{25}$-*b*-$PMOXA_{10}$ GUVs a) with and b) without reconstituted membrane protein OmpF, recorded by CLSM at different time points.

In both cases, with and without OmpF, an increased fluorescence over time was visible inside and outside of GUVs. For the microreactor with OmpF (Figure 75a), the fluorescence inside GUVs increased significantly quicker than the background outside of GUVs, whereas for the negative control (Figure 75b), no significant difference between inside and outside intensity could be observed. In order to confirm the visual impressions, the mean fluorescence intensities on the inside and the outside of GUVs were measured every 15 min. The averaged intensities and their standard deviations are displayed in Figure 77a for the (*R*/*S*)-BCP microreactor with OmpF and for the negative control. The intensities of the negative control (inside of GUVs without OmpF, outside of GUVs without OmpF) as well as outside of GUVs with OmpF were similar for all instants of time. Solely the intensity inside GUVs with reconsitituted OmpF rose significantly above the background and reached a plateau after

75 min. This behaviour can be interpreted as follows: in case of GUVs with reconstituted OmpF, RGP diffused through the OmpF pores into the GUVs and got cleaved by β-Gal, forming the fluorescent resorufin, which accumulated inside the cavity and led to a strong increase in fluorescence. Over time, resorufin diffused out of the GUVs through the OmpF pores, leading to an increasing background fluorescence. The development of the plateau after 75 min indicated a dynamic equilibrium between RGP entering the vesicles and resorufin leaving the inner cavity. When OmpF was missing, the passage of RGP through the membrane was hindered due to the lacking OmpF pores. This behaviour is known in literature for similar microreactors equipped with OmpF.[109] The background fluorescence of the negative control originated from ruptured GUVs releasing β-Gal and inducing an enzyme reaction before being cleaved by proteinase K.

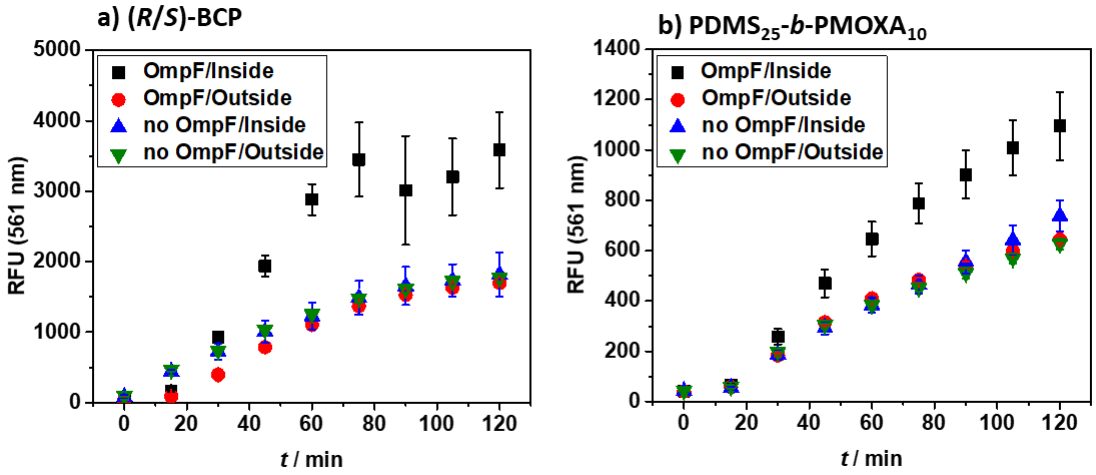

Figure 77: Fluorescence intensity development of a) (*R*/*S*)-BCP and b) $PDMS_{25}$-*b*-$PMOXA_{10}$ GUVs resulting from the reaction of resorufin β-D-galactopyranoside (RGP) with β-galactosidase (β-Gal) to yield fluorescent resorufin. The intensities measured inside GUVs containing OmpF (black squares), outside of GUVs containing OmpF (red circles), inside of GUVs without OmpF (blue triangles) and outside of GUVs without OmpF (green triangles) are displayed. Up to 15 GUVs per image were measured and the mean intensities were calculated using their standard deviations as errors.

In order to confirm the applicability of PBO-*b*-PG microreactors as platform to prove the successful membrane protein insertion, a comparison with the aforementioned $PDMS_{25}$-*b*-$PMOXA_{10}$ GUVs was drawn. The latter polymer was already employed to reconstitute OmpF in its membrane[107] and has a comparable membrane thickness (12.0 ± 0.8 nm, section 3.2.5) to the one of the (*R*/*S*)-BCP (11.1 ± 0.8 nm, section 3.2.1). The snapshots of the enzyme reaction are displayed in Figure 76. The PDMS-*b*-PMOXA based microreactors exhibited a similar behaviour as the (*R*/*S*)-BCP GUVs regarding the intensity development inside and outside of GUVs with and without OmpF (Figure 77b). In contrast to (*R*/*S*)-BCP GUVs, no plateau but rather a constant increase in the fluorescence intensity was observed for $PDMS_{25}$-*b*-$PMOXA_{10}$ GUVs. As the intensity plateau was reached earlier for (*R*/*S*)-BCP microreactors, a higher permeability was hinted for PBO-*b*-PG membranes than for PDMS-*b*-PMOXA membranes. Similarly, the negative control of (*R*/*S*)-BCP-based GUVs led to a higher background

fluorescence than in case of PDMS-*b*-PMOXA GUVs, which also indicated a higher permeability of PBO-*b*-PG membranes. This was coherent with literature as PDMS-based membranes are known to form highly impermeable membranes due to their high hydrophobicity.[109,120,124]

To conclude, both BCPs were equally able to reconstitute OmpF. Thus, the PBO-*b*-PG system sets the first basis to analyse the insertion of membrane proteins into chiral membranes composed of isotactic PBO-*b*-PG. This, in turn, could allow for significantly faster reaction rates than with membranes from PDMS-*b*-PMOXA, once the GUVs are sufficiently stable.

3.4. Chiral interaction

In this chapter, QCM-D will be employed to analyse possible chiral interaction of SUVs composed of the isotactic BCPs with chiral substances such as amino acids, phospholipids and isotactic PG homopolymers.

In order to elucidate whether membranes composed of isotactic PBO-*b*-PG exhibit chiral interaction with enantiopure compounds QCM-D measurements were performed. The measurements were based on the deposition of SUVs composed of the isotactic BCPs on gold sensors and subsequent addition of chiral molecules such as enantiopure amino acids, lipids or the isotactic PG homopolymers. Adsorption of these compounds on the SUVs and thus a mass increase on the sensor should be detected by a resonance frequency decrease according to equation (5). Specific adsorption of a stereoregular compound on the SUV membrane of one BCP tacticity and not on SUVs composed of the opposite BCP tacticity would be the proof of chiral interaction based on the configuration of the membrane forming BCP.

Firstly the protocol for SUV adsorption and data analysis was optimised, involving test runs of (*S*)- and (*R*)-BCP SUVs on plasma-activated gold sensors (Figure 78 for the (*R*)-BCP, Figure 79 for the (*S*)-BCP). After setting a stable baseline with PBS with frequencies and dissipations of ± 0.5 a dispersion of the respective SUVs was added. The decreasing frequencies of Δf between –130 and –200 Hz for the (*R*)-BCP SUVs recorded for all overtones ($f3$-$f13$ in Figure 78a) indicated a mass increase originating from adsorbing SUVs.[41,42] When a stable plateau was formed after 8 min, non-adsorbed SUVs were removed by washing with PBS which increased the frequencies slightly by approximately 5 Hz. The addition of the tenside Triton X-100 triggered a rupture of the adsorbed SUVs,[213] indicated by a strong frequency increase to –30 to –50 Hz corresponding to a mass decrease originating from BCP removal and water release from the cavities of the SUVs.[45] Thus it was confirmed that the SUVs stayed intact during adsorption and could be intentionally ruptured by addtion of Triton X-100. Subsequent washing

with PBS led to a frequency increase back to the baseline as remaining BCP and tenside was removed. The final cleaning step was done with water.

The recorded dissipations of all overtones (*D*3-*D*13, Figure 78b) gave information about the viscoelastic properties of the adsorbents.[40,46,47] The dissipations increased from the 0 ppm baseline to 17 to 27 ppm, depending on the overtone, when SUVs were added, indicating a higher elasticity as SUVs were soft and flexible. The triggered rupture of SUVs by Triton X-100 addition led to dissipation shifts as the viscoelasticity was changed. Washing with PBS decreased the dissipations back to the baseline as the original viscoelasticity of the sensor in PBS was restored.

The different frequencies and dissipations on every overtone when SUVs were adsorbed indicated that no homogenous, rigid film was deposited on the sensor. Hence, the Sauerbrey conditions were not matched by the system presented here, preventing a straight-forward calculation of layer thickness or adsorbed mass according to equation (5). Therefore the results shown here serve only as qualitative measure but do not allow for a quantification of sensor coverage, thickness and mass adsorbed on sensor or SUV. For the following analyses of chiral interaction the 7th overtone was considered.

Comparable behaviour for the (*S*)-BCP SUVs (Figure 79) proved that SUVs composed of BCPs of both configurations similarly adsorbed onto gold sensors and stayed intact until an intended rupture was triggered.

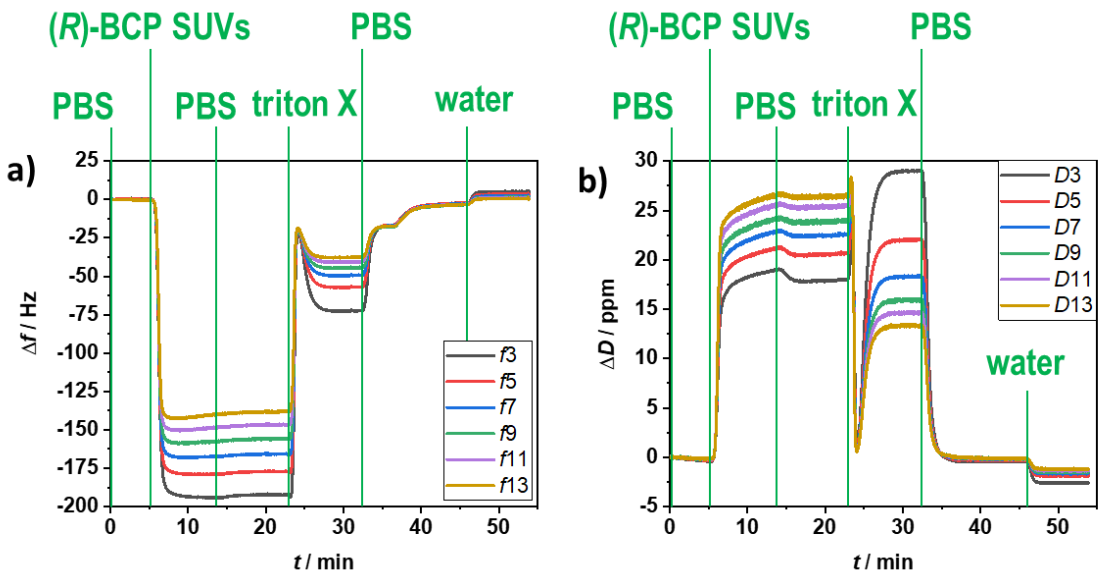

Figure 78: QCM-D results of the adsorption of (*R*)-BCP SUVs on a gold sensor. The baseline was set with PBS, afterwards a dispersion of (*R*)-BCP SUVs was added, followed by a washing step with PBS, addition of the tenside Triton X-100, washing with PBS and cleaning with water. a) Normalised frequencies of all overtones (*f*3-*f*13). b) Normalised dissipations of all overtones (*D*3-*D*13).

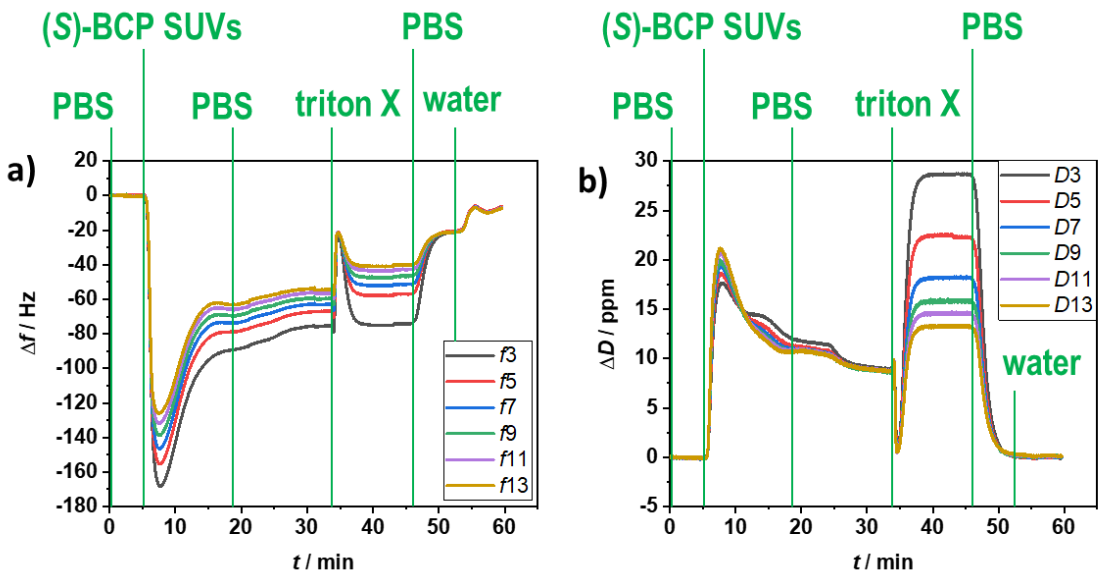

Figure 79: QCM-D results of the adsorption of (S)-BCP SUVs on a gold sensor. The baseline was set with PBS, afterwards a dispersion of (S)-BCP SUVs was added, followed by a washing step with PBS, addition of the tenside Triton X-100, washing with PBS and cleaning with water. a) Normalised frequencies of all overtones used (*f*3-*f*13). b) Normalised dissipations of all overtones used (*D*3-*D*13). The increasing frequency and decreasing dissipation after SUV addition can be attributed to a constant detachment of SUVs, which in turn could have originated from an insufficient plasma treatment of the sensor, impurities or rupture of several SUVs shortly after adsorption.

The protocol for the evaluation of possible chiral interaction involved the following steps: firstly, a baseline in PBS was set, followed by the addition of (*R*)- or (*S*)-BCP SUVs, washing with PBS, addition of the chiral compound and final washing with PBS (Figure 80 to Figure 88). As chiral compounds the enantiopure amino acids L-alanine (L-Ala), L-cysteine (L-Cys) and L-serine (L-Ser) were chosen, as well as the enantiopure phospholipids (*R*)-dipalmitoylphosphatidylcholine (DPPC) and (*R*)-palmitoyloleoylphosphatidylcholine (POPC) and the drug and flavouring (−)-menthol.

Firstly the adsorption of L-Ala on SUVs composed of the isotactic BCPs was evaluated (Figure 80). After adsorption of the SUVs and washing with PBS, L-Ala was added, leading to a frequency increase of around 30 Hz and a dissipation decrease of about 8 ppm, similarly for SUVs of both BCPs. After washing with PBS both the frequency and the dissipation went back to their levels before L-Ala adddition. Consequently, L-Ala did not adsorp on any of the samples; a chiral interaction was thus not monitored. Note that a frequency decrease/mass increase was generally also possible by adsorption of chiral compounds directly on the sensor, in case the latter was not covered completely by the SUVs.[210]

In case of L-Cys (Figure 81) and L-Ser (Figure 82) the differences between (*R*)- and (*S*)-BCP SUVs were more pronounced, the trend however remained similar: either the frequency increased constantly independently of the solution added (Figure 81) or the frequency increased but reached their previous plateau again after washing (Figure 82). The preferred adsorption of a chiral amino acid on SUVs of one BCP configuration could not be detected.

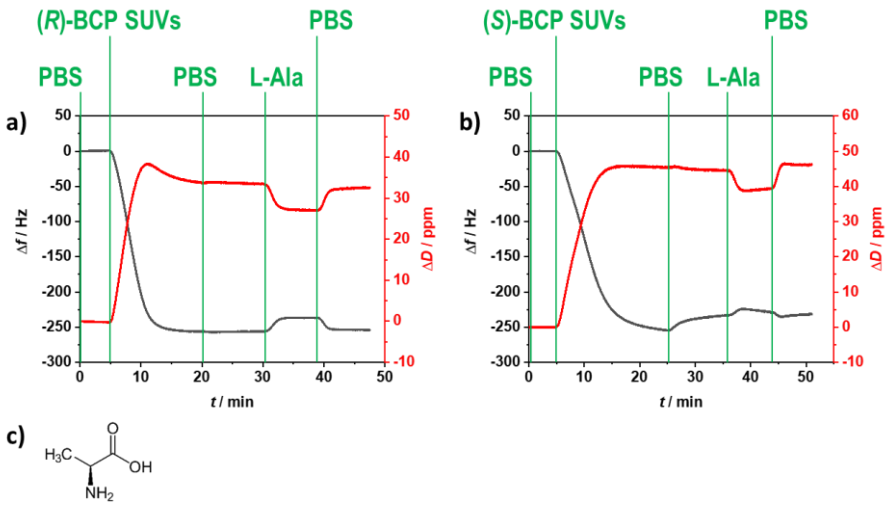

Figure 80: QCM-D results of the adsorption of a) (*R*)-BCP SUVs and b) (*S*)-BCP SUVs on a gold sensor and subsequent addition of L-Ala. The baseline was set with PBS, afterwards a dispersion of the respective SUV was added, followed by a washing step with PBS, addition of L-Ala and washing with PBS. The frequency of the 7th overtone is displayed on the left axis (black), the dissipation of the 7th overtone is displayed on the right axis (red). c) Chemical structure of L-Ala.

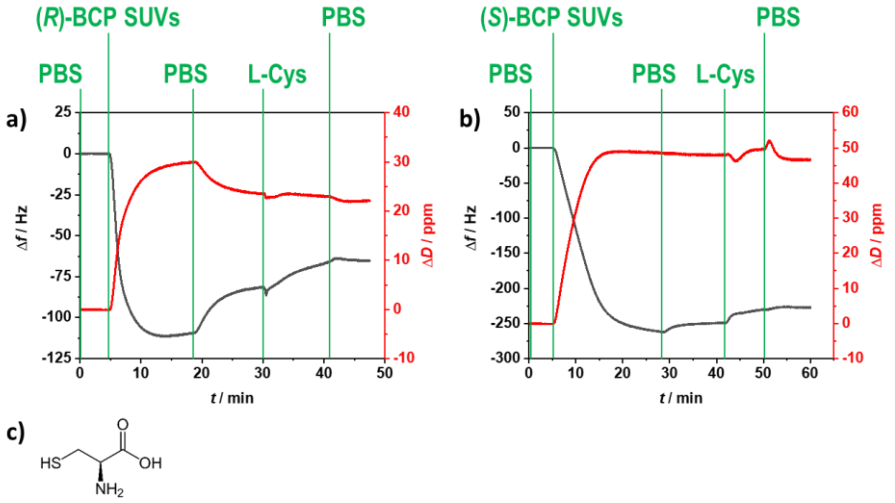

Figure 81: QCM-D results of the adsorption of a) (*R*)-BCP SUVs and b) (*S*)-BCP SUVs on a gold sensor and subsequent addition of L-Cys. The baseline was set with PBS, afterwards a dispersion of the respective SUV was added, followed by a washing step with PBS, addition of L-Cys and washing with PBS. The frequency of the 7th overtone is displayed on the left axis (black), the dissipation of the 7th overtone is displayed on the right axis (red). c) Chemical structure of L-Cys.

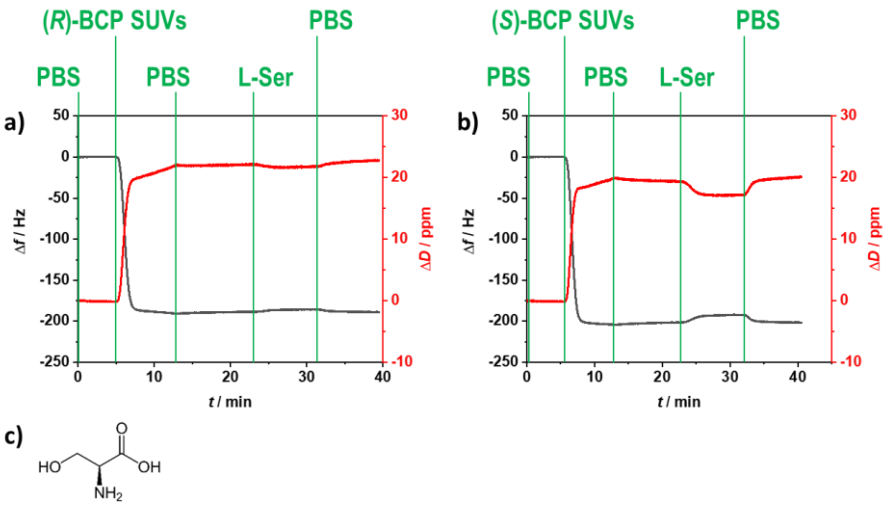

Figure 82: QCM-D results of the adsorption of a) (*R*)-BCP SUVs and b) (*S*)-BCP SUVs on a gold sensor and subsequent addition of L-Ser. The baseline was set with PBS, afterwards a dispersion of the respective SUV was added, followed by a washing step with PBS, addition of L-Ser and washing with PBS. The frequency of the 7th overtone is displayed on the left axis (black), the dissipation of the 7th overtone is displayed on the right axis (red). c) Chemical structure of L-Ser.

The adsorption of enantiopure DPPC and POPC as phospholipids is displayed in Figure 83 and Figure 84, respectively. In case of DPPC, a mass increase indicated by a frequency decrease of about 50 Hz was detected for both the (*S*)- and (*R*)-BCP SUVs. This hinted a DPPC adsorption on the SUVs or on non-covered sensor independently of the BCP configuration. For POPC no significant frequency or dissipation changes could be detected during the experiments. When adding (−)-menthol to the SUVs a mass increase was detected (Figure 85). After washing, the frequencies and dissipations in both cases returned to their values before addition. Thus, also here no specific chiral interaction could be found.

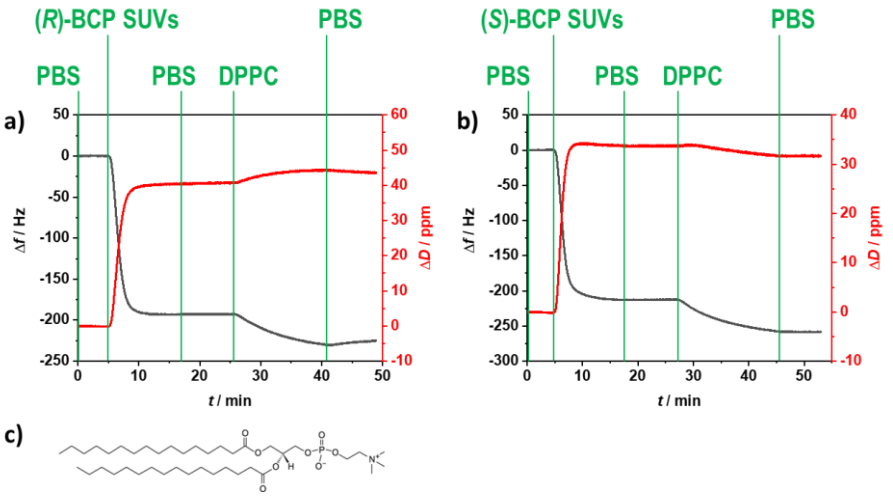

Figure 83: QCM-D results of the adsorption of a) (*R*)-BCP SUVs and b) (*S*)-BCP SUVs on a gold sensor and subsequent addition of DPPC. The baseline was set with PBS, afterwards a dispersion of the respective SUV was added, followed by a washing step with PBS, addition of DPPC and washing with PBS. The frequency of the 7th overtone is displayed on the left axis (black), the dissipation of the 7th overtone is displayed on the right axis (red). c) Chemical structure of DPPC.

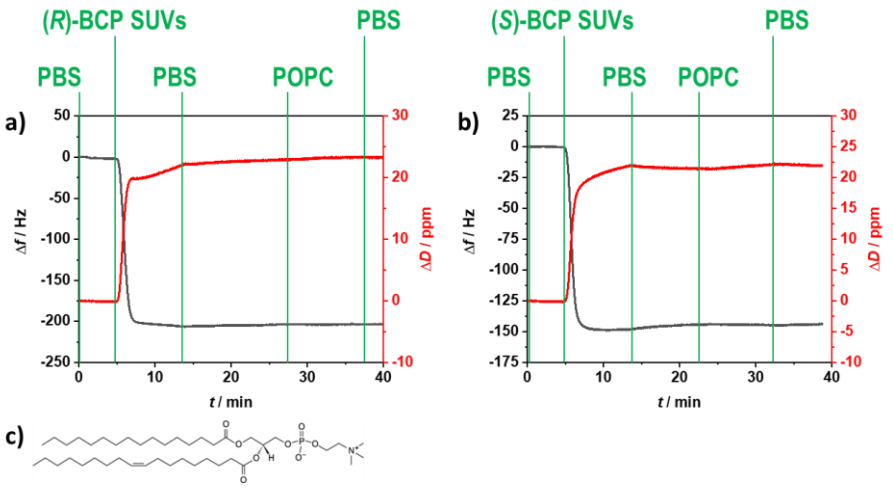

Figure 84: QCM-D results of the adsorption of a) (*R*)-BCP SUVs and b) (*S*)-BCP SUVs on a gold sensor and subsequent addition of POPC. The baseline was set with PBS, afterwards a dispersion of the respective SUV was added, followed by a washing step with PBS, addition of POPC and washing with PBS. The frequency of the 7th overtone is displayed on the left axis (black), the dissipation of the 7th overtone is displayed on the right axis (red). c) Chemical structure of POPC.

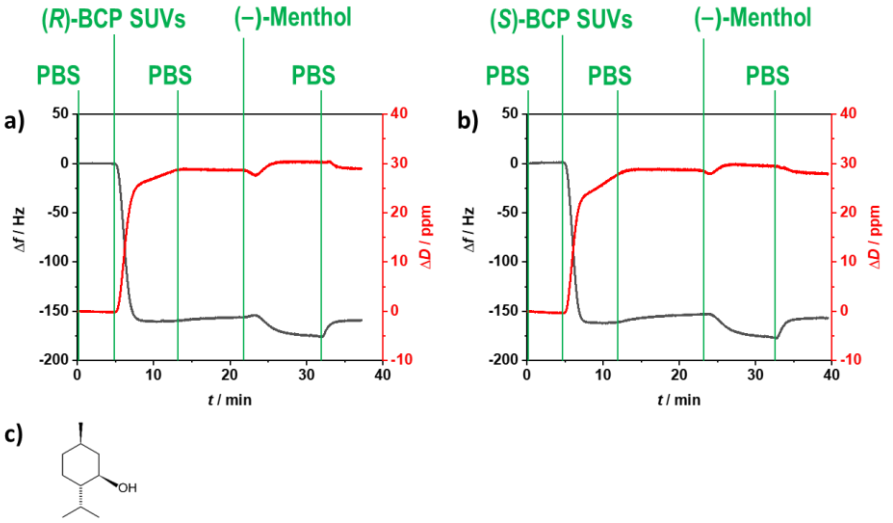

Figure 85: QCM-D results of the adsorption of a) (*R*)-BCP SUVs and b) (*S*)-BCP SUVs on a gold sensor and subsequent addition of (−)-menthol. The baseline was set with PBS, afterwards a dispersion of the respective SUV was added, followed by a washing step with PBS, addition of (−)-menthol and washing with PBS. The frequency of the 7th overtone is displayed on the left axis (black), the dissipation of the 7th overtone is displayed on the right axis (red). c) Chemical structure of (−)-menthol.

The tested enantiopure small molecules (amino acids, phospholipids and menthol) did not suggest specific chiral interaction with the SUVs composed of (*R*)- or (*S*)-BCP. A possible interaction was expected to be based on the isotactic hydrophilic block of the membrane forming BCP. Hence interaction of this PG block with dissolved PG homopolymer of similar or opposite configuration was tested (Figure 86 and Figure 87). When adding (*R*)-PG homopolymer to the SUV dispersions a slight mass increase was detected by a frequency decrease of around 10 Hz, both for the (*S*) as well as the (*R*)-BCP SUVs (Figure 86). A similar mass increase was found for the addition of (*S*)-PG homopolymer to both SUV dispersions (Figure 87). The similar behaviour for SUVs of both BCP configurations,

concluded by the frequencies and dissipations returning to their values before PG addition did not suggest a chiral interaction of SUVs with any kind of PG homopolymer.

Ultimately, in order to increase the local concentration of isotactic PG, an SUV dispersion of (*S*)-BCP was added to a dispersion of (*R*)-BCP SUVs and *vice versa* (Figure 88). A frequency increase over time was detected in both cases, independently of configuration or if SUV or washing solution was added. Again, a specific chiral interaction was not observed.

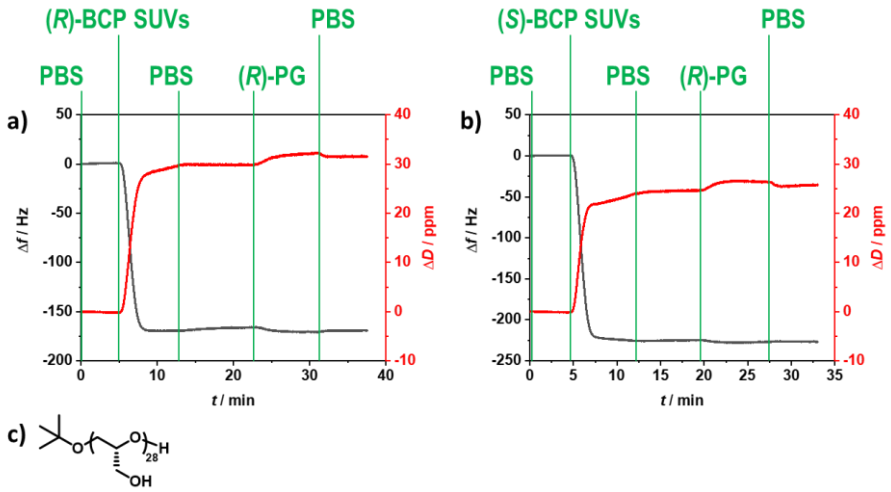

Figure 86: QCM-D results of the adsorption of a) (*R*)-BCP SUVs and b) (*S*)-BCP SUVs on a gold sensor and subsequent addition of (*R*)-PG homopolymer. The baseline was set with PBS, afterwards a dispersion of the respective SUV was added, followed by a washing step with PBS, addition of (*R*)-PG and washing with PBS. The frequency of the 7th overtone is displayed on the left axis (black), the dissipation of the 7th overtone is displayed on the right axis (red). c) Chemical structure of (*R*)-PG.

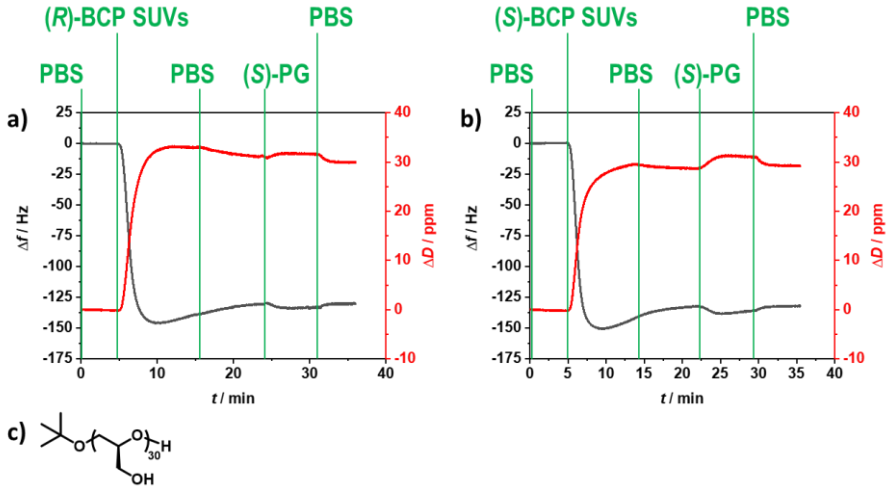

Figure 87: QCM-D results of the adsorption of a) (*R*)-BCP SUVs and b) (*S*)-BCP SUVs on a gold sensor and subsequent addition of (*S*)-PG homopolymer. The baseline was set with PBS, afterwards a dispersion of the respective SUV was added, followed by a washing step with PBS, addition of (*S*)-PG and washing with PBS. The frequency of the 7th overtone is displayed on the left axis (black), the dissipation of the 7th overtone is displayed on the right axis (red). c) Chemical structure of (*S*)-PG.

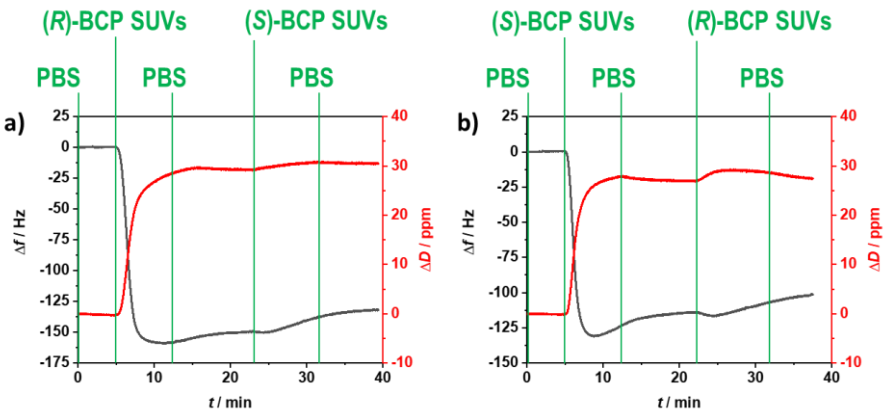

Figure 88: QCM-D results of the adsorption of a) (*R*)-BCP SUVs on a gold sensor and subsequent addition of (*S*)-BCP SUVs and b) (*S*)-BCP SUVs on a gold sensor and subsequent addition of (*R*)-BCP SUVs. The baseline was set with PBS, afterwards a dispersion of the respective SUV was added, followed by a washing step with PBS, addition of the respective SUV dispersion of opposite chirality and washing with PBS. The frequency of the 7th overtone is displayed on the left axis (black), the dissipation of the 7th overtone is displayed on the right axis (red).

In conclusion, chiral interaction of SUVs composed of isotactic BCPs with chiral substances such as amino acids, phospholipids, menthol, PG homopolymer or SUVs composed of BCPs with the opposite configuration was not detected by QCM-D. However, these results were preliminary and require further evaluation by an alternative method such as ITC. Also interaction with chiral cargo or membrane proteins needs to be analysed.

4. General Conclusion and Outlook

4.1. General Conclusion

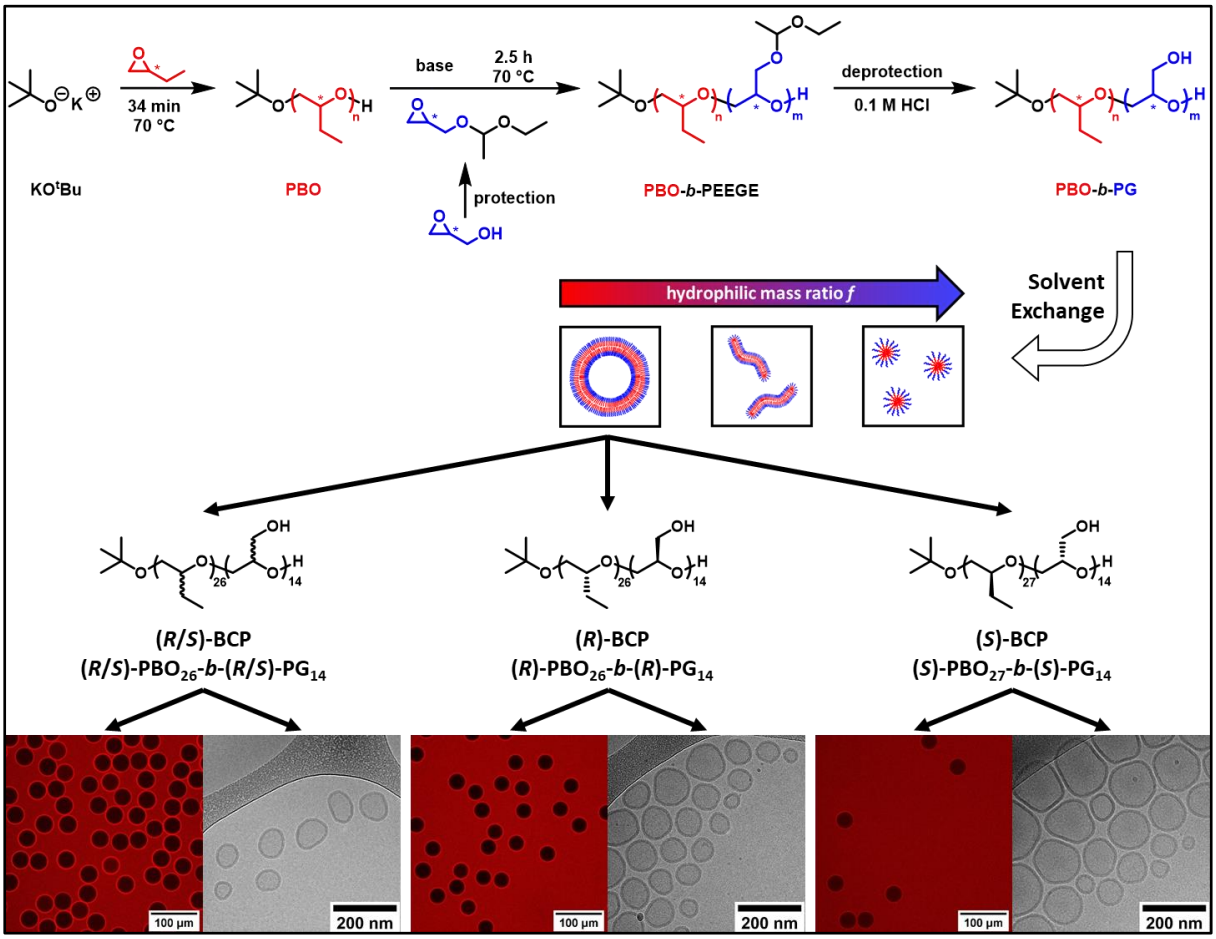

Figure 89: Summary of the results presented in this work: Sequential microwave-assisted AROP of epoxide monomers led to the formation of PBO-*b*-PG diblock copolymers. These BCPs formed, depending on their *f*-ratio, homogenous phases of nanoscopic SUVs, worms and spherical micelles in aqueous medium by solvent exchange. Applying this protocol for enantiopure monomers led to the formation of (*R*/*S*)-atactic as well as (*R*)- and (*S*)-isotactic BCPs, which were able to form SUVs by solvent exchange and GUVs by double emulsion microfluidics.

A series of atactic PBO-*b*-PG amphiphilic diblock copolymers was synthesised in microvave-assisted reactions. Kinetic measurements confirmed the high control and reproducibility of the polymerisation at significantly shorter reaction times than conventional syntheses. The amorphous character of the BCPs was proven by DSC measurements, which is essential for applications where fluid and flexible membranes are necessary. Self-assembly by solvent exchange led to the formation of well-defined structures in homogenous phases. The formed structures followed the established self-assembly theory by undergoing a transition from micelles over worms to nanoscopic vesicles (SUVs) with decreasing hydrophilic mass fraction. Also microscopic GUVs were prepared, showing the versatility of possible structures. A comparison to film rehydration revealed that stable and well-defined structures were

formed solely by solvent exchange when the appropriate conditions (solvent, composition of the BCP, self-assembly conditions) were applied. The self-assemblies presented here benefit from the high biocompatibility and flexibility of the BCPs and were obtained in pure, homogenous and reproducible phases, allowing further investigations of their biomedical and biotechnological applicability.

Based on the synthesis and self-assembly of atctic PBO-*b*-PG three highly similar BCPs were synthesised, differing solely in their configuration: one atactic (*R*/*S*)-BCP, one isotactic (*R*)-BCP and one isotactic (*S*)-BCP. All polymerisations were highly controlled and showed perfect first-order kinetics with similar reaction rates. Tacticity and optical activity were proven by polarimetry, CD spectroscopy and ^{13}C NMR spectroscopy. Despite the differences in their respective stereochemistry, all polymers possessed similar thermal and structural behaviour. It was proven that the stereoregularity did neither induce crystallinity nor the formation of secondary structures in bulk or solution. Subsequently, all BCPs were self-assembled into homogenous phases of SUVs by solvent exchange and into GUVs by double emulsion microfluidics. The potential of fully amorphous PBO-*b*-PG membranes for complex applications involving membrane proteins was highlighted by a successful and functional reconstitution of the membrane protein OmpF into (*R*/*S*)-BCP GUVs. This allowed for the creation of microreactors to perform an enzyme reaction. Stability differences between (*R*/*S*)-BCP, (*R*)-BCP and (*S*)-BCP were found for SUVs and GUVs, suggesting an influence of the tacticity of the respective BCPs. In general, SUVs composed of atactic and isotactic BCPs were stable at least over one week. However, the BCP composition needs to be further optimised to access more stable GUVs, in particular when composed of isotactic BCPs. Thus, this thesis represents the first study discriminating the effect of tacticity from crystallinity in aqueous self-assemblies of amphiphilic BCPs. Preliminary tests of a possible chiral interaction were negative, as there was no difference detected in the interaction of chiral substances with membranes composed of (*R*)- or (*S*)-BCPs.

4.2. Challenges and Outlook

In order to overcome the observed limitations and increase the applicability of the atactic and isotactic PBO-*b*-PG self-assemblies, the following points need to be considered:

- Solvent exchange involves organic solvents, which are harmful for organisms. Thus, it needs to be ensured that all traces of solvents are thoroughly removed before applying the self-assemblies in the biomedical field.
- In this regard, the presence of organic solvents during self-assembly also hinders a combination with biomolecules such as cargo or membrane proteins sensitive to organic solvents. Hence,

the use of film rehydration would be beneficial, despite resulting in less control and impure self-assembly phases.

- PBO-*b*-PG is neither stimulus-responsive nor biodegradable. For specific applications where those features are necessary, for example the controlled release of cargo upon a stimulus, a change in the chemical composition is required. That could be achieved for example by adding a cleavable linker between the blocks or side- or end-group modification.
- Post-polymerisation end-group modification is barely possible as it cannot be assured that only the terminal hydroxy group reacts while the hydroxy moieties on every PG repeating unit remain unaffected. Hence, the end-group modification needs to be performed before the cleavage step of PEEGE, and the resulting functionalisation must not be cleaved when deprotecting the PEEGE block. A simple esterification for example thus seems inappropriate as it can be cleaved in acidic environment as well.
- Double emulsion microfluidics allowed for the formation of GUVs composed of the same PDMS-*b*-PMOXA BCP that was employed for the formation of SUVs. In contrast, PBO-*b*-PG BCPs optimised for SUV formation possessed a limited suitability for GUV formation, as these GUVs ruptured within minutes to hours. Optimisation of the hydrophilic mass ratio could overcome this drawback, however at the expense of a decreased SUV stability. Additionally, increased hydrophobic interactions by using higher molecular weight BCPs could stabilise the membrane, however hindering the desired membrane protein insertion due to the increased membrane thickness. In this regard, synthesising an optimised BCP batch solely for the formation of GUVs seems beneficial.
- Particularly in comparison to PDMS-*b*-PMOXA, PBO-*b*-PG membranes seem generally less stable and more permeable for hydrophilic substances because of their elongated chain conformation and the more hydrophilic character of the BCP. Employing more hydrophobic isotactic blocks could lead to an increase in membrane stability.
- Analysing chiral interaction of (*R*)- and (*S*)-BCP SUVs with chiral cargo requires optimised methods such as ITC. The presented QCM-D results should be perceived as preliminary.

Reconstituting OmpF in GUVs composed of the isotactic BCPs was not possible in this work due to their instability. However, for future applications it will be advantageous to elucidate how the stereoregularity of the membrane forming BCPs affects the membrane pore insertion. The ability to reconsititute membrane proteins in fully amorphous isotactic PBO-*b*-PG membranes can set a basis to analyse the interplay of the membrane chirality with the passage of substrates. The stereocontrol of the membrane–forming BCP could potentially lead to an intrinsically anisotropic membrane that favours the directional insertion of transmembrane proteins and allow a unidirectional passage of substrates (Figure 90), which has so far been achieved only by employing asymmetric lipid membranes or ABC triblock copolymer membranes.[148,214] Thus lipid membranes in liposomes and cells, whose chiral

interaction with membrane pores originates from enantiopure phospholipids and asymmetric membranes could be mimicked. Although chiral recognition of a membrane composed of isotactic BCPs with chiral compounds was not found in the preliminary studies presented here, the system could potentially serve as a model to analyse chiral interaction with membrane and cargo such as enantiopure drugs.

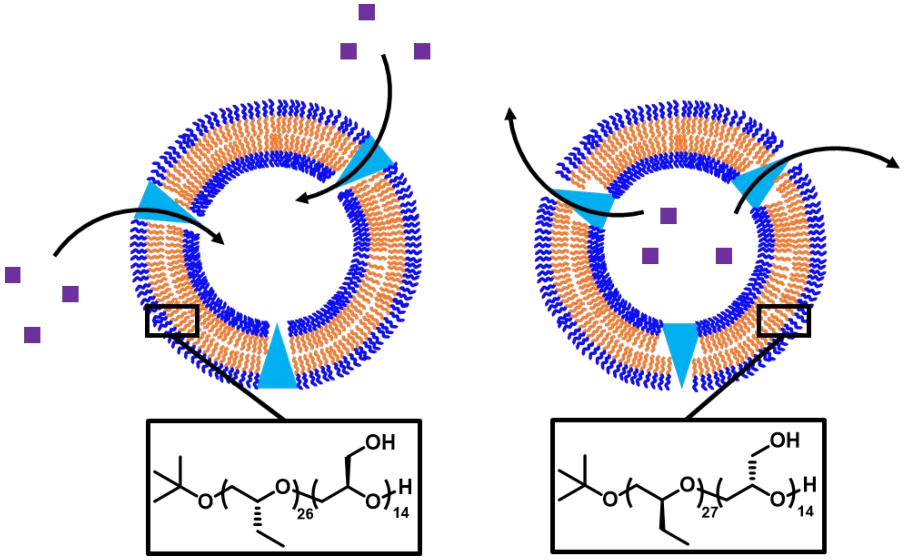

Figure 90: Schematic representation of a potential directed insertion of a membrane protein for unidirectional passage of substrates through the membrane. The membrane protein could insert in one direction in the membrane composed of the (*R*)-BCP (left) and allow a passage of substrates into the vesicle (or into the opposite direction). If the (*S*)-BCP (right) is used, the membrane protein could insert in the opposite direction and allow for a passage of substrates from the lumen to the outside of the vesicle (or into the opposite direction).

In order to elucidate if the stereocontrol of the BCPs also leads to changing macroscopic properties of the polymer membranes, force spectroscopy *via* atomic force microscopy (AFM) could be employed. This would give access to Young´s or bending moduli and would allow conclusions about elasticity and flexibility of the membranes.[161] On the other hand, fluorescence correlation spectroscopy (FCS) of dye-labelled polymer membranes could be used to track the fluidity and diffusion of isotactic BCPs within the membrane in comparison to atactic BCPs.[57] These studies, however, do not seem particularly promising as from the current perspective (membrane thickness, thermal properties, crystallinity) no macroscopic differences between atactic and isotactic PBO-*b*-PG are to expect.

5. Experimental

5.1. Materials

All glassware used for the polymerisations was dried overnight at 120 °C prior to use. *n*-Butyl lithium solution (2.5 M in hexanes), 2-allyloxyethanol (98%), platinum(0)-1,3-divinyl-1,1,3,3-tetramethyldisiloxane complex solution (in xylene, Pt ~ 2%), dimethylchlorosilane (98%), triethylamine (>99.5%), trifluoromethanesulfonic anhydride (>99%), potassium *tert*-butoxide (≥98%), 1,4,7,10,13,16-hexaoxacyclooctadecane (18-crown-6, ≥99%), racemic 1,2-butylene oxide (99%), ethyl vinyl ether (≥98%), racemic glycidol (96%), calcium hydride (CaH_2, 95%), potassium (chunks in mineral oil, 98%) and naphthalene (99%) were purchased from Sigma-Aldrich (Switzerland) and used as received. Hexamethylcyclotrisiloxane (98%), 2-methyl-2-oxazoline (98%), the enantiopure monomers (*R*)- and (*S*)-1,2-butylene oxide (98%, *ee* unknown) as well as (*R*)- and (*S*)-glycidol (97%, *ee* 98%) were purchased from Sigma-Aldrich (Switzerland), dried over CaH_2 and distilled prior to use. Dry solvents were obtained from an inert solvent purification system PureSolv MD 5 (Inert Technology, USA, THF) or from Acros Organics (Belgium). The other solvents used were in HPLC grade and purchased from JT Baker (USA), VWR (Switzerland) or Scharlau (Germany). Deionised water was obtained from a MilliQ Q-POD device (Merck, Germany). PBS buffer was prepared in house using 8 g NaCl, 0.2 g KCl, 1.44 g Na_2HPO_4 and 0.24 g KH_2PO_4 per L PBS. Potassium naphthalenide (KNaph) was prepared by adding potassium (1.19 g, 30.5 mmol, 1eq) to a stirred solution of naphthalene (4.11 g, 32.0 mmol, 1.05 eq) in dry THF (61 mL, 0.5 mol/L) under nitrogen. Racemic and enantiopure EEGE was synthesized according to the standard protocol[215] from racemic or enantiopure glycidol and EVE, dried over CaH_2. and distilled prior to use. All reactants were stored under argon or nitrogen atmosphere in a glovebox (MBraun Labstar, Germany).

5.2. Methods

Nuclear Magnetic Resonance (NMR) Spectroscopy. ^1H and ^{13}C NMR spectra were recorded at 295 K in methanol-d_4 (MeOD) or TMS-free chloroform-d_1 ($CDCl_3$) (Cambridge Isotope Laboratories, USA) on a 500 MHz Advance III NMR spectrometer (Bruker, USA). The device was equipped with a BBFO SP FB standard probe and a default number of 16 scans for the ^1H NMR spectra and 1024 scans for the ^{13}C NMR spectra was used. The water signal in MeOD (4.85 ppm) or the residual solvent peak in $CDCl_3$

(7.26 ppm) were used for calibration. Processing of the spectra was performed in MestReNova software (version 11.0, Mestrelab, Spain).

Gel Permeation Chromatography (GPC). GPC measurements were performed in HPLC grade DMF (Scharlau, Germany) at 60 °C with a flow rate of 1 mL/min. Narrowly distributed poly(methyl methacrylate) or poly(ethylene glycol) molecular weight standards were used for calibration. The Viscotek TDA 305 device (UK) was equipped with three SDV Linear S columns (5 µm, 8×300 mm, PSS, Germany), a PSS precolumn (SDV, 5 µm, 8×50 mm) and a refractive index (RI) detector. The control of the instrument and the analyses of the traces were done in WinGPC UniChrom software (version 8.20, PSS).

Polarimetry. Optical rotations were measured on a MCP 100 (Anton Paar, Austria), equipped with a 589 nm laser. The stainless steel measurement cylinder had a capacity of 0.05 mL with a path length of 2.5 mm and a diameter of 5 mm. 3 repetitive measurements were performed at 25 °C, using methanol as solvent and reference, and a monomer or polymer concentration of 50 mg/mL (5% w/v). The specific rotation is stated and was calculated from the measured optical rotation by using the following formula: $[\alpha]_D^{25} = \alpha/(l \cdot c)$ with $[\alpha]_D^{25}$ optical rotation, l path length and c concentration.

Circular Dichroism (CD) Spectroscopy. CD spectra were recorded on a J-1500 CD spectrometer (Jasco, Japan) equipped with a nitrogen purging set-up and an argon lamp. Measurements were carried out at 20° C in a 1 mm optical path length quartz cuvette (Hellma Analytics, Germany). The spectra were recorded at a sample concentration of 60 mg/mL from 600 nm to 165 nm at a scan rate of 50 nm/min. *n*-hexane was used as solvent for the BCPs and PBO homopolymers and water was used for the PG homopolymers.

Thermogravimetric Analysis (TGA). TGA measurements were performed on a TGA 5500 (TA Instruments, USA) in aluminium crucibles. 2–5 mg of the polymers were heated with a heating rate of 10 K/min from room temperature to 600 °C under nitrogen atmosphere. The thermograms were analysed using the TRIOS software (TA Instruments, version 5.1.1).

Differential Scanning Calorimetry (DSC). DSC traces were recorded on a DSC 214 Polyma (Netzsch, Austria) under nitrogen atmosphere from –150 to 120 °C with a heating and cooling rate of 10 K/min from 10 mg of sample in aluminium crucibles. The thermographs were evaluated using Netzsch Proteus software (version 7.1). The second heating curves are shown and were used to analyse the thermal transitions. The glass transition temperatures (T_g) were measured at the inflection points of every curve.

Transmission Electron Microscopy (TEM). TEM images were recorded on a CM100 transmission electron microscope (Philipps, Netherlands) at an acceleration voltage of 80 kV. Formvar-coated 200 mesh copper grids were glow discharged for 30 seconds prior to use. 15 µL of diluted (0.5 mg/mL) self-assembly dispersion were left adsorbing on the grid for one minute and afterwards blotted off with a

filter paper. Then, the grid was washed two times with 50 µL sized water drops. Afterwards, a 5 µL sized drop of 2% aqueous uranyl acetate solution was placed on the grid and blotted off immediately. A second 5 µL sized drop of uranyl acetate solution was left adsorbing for 10 seconds and eventually blotted off before imaging the sample. The size of micelles as well as the length and thickness of worms were measured in ImageJ (NIH, USA).

Cryogenic Transmission Electron Microscopy (Cryo-TEM). A Talos electron microscope (Thermo Fisher, USA) equipped with a Gatan 626 cryo-holder and CETA camera was used for Cryo-TEM imaging. 4 µL of a 4 mg/mL self-assembly dispersion was adsorbed onto a holey carbon-coated grid (Lacey, Tedpella, USA) and blotted off with Whatman 1 filter paper. The sample was vitrified into liquid ethane at –178 °C using a Leica GP plunger (Leica, Austria). Recording of the micrographs was done at an acceleration voltage of 200 kV and a nominal magnification of 57,000×. A low-dose system (20 e^- $Å^{-2}$) was used by maintaining the sample at low temperature. Diameters and membrane thicknesses of vesicles were measured using ImageJ (NIH, USA).

Dynamic and Static Light Scattering (DLS/SLS). Multi-angle light scattering data were recorded on a LS spectrometer (LS Instruments, Switzerland) which was equipped with a 633 nm He-Ne laser with 21 mW. All experiments were measured at scattering angles between 30 and 135° at 25 °C in round-bottom cuvettes (10×0.9–1.0 mm, Boro 3.3). For both DLS and SLS measurements, diluted self-assembly dispersions of 0.05 mg/mL were used without filtration. Hydrodynamic radii (R_h) were calculated by DLS as a mean value of three independant measurements over the whole angle range using second order cumulant analyses. Polydispersity indices (PDI) were calculated from the 90 ° DLS measurements. SLS data were used to calculate the radius of gyration (R_g) either by Guinier or by Mie fitting, depending on size and dispersity of the sample. When using the Guinier model, the natural logarithm of the intensity (ln$I$) was plotted against the scattering vector (q^2) in the Guinier regime (30–55 °) and fitted with a linear fit. The R_g was calculated from the slope following the equation $slope = -R_g^2/3$. When using the Mie model, the mean intensity of three repetitive measurements was plotted against the corresponding angle and fitted with a Mie scattering model (MiePlot, UK) for $\eta = 1.35$ and 5% polydispersity. The radius R was obtained from the best fit and the R_g was calculated from the hard sphere model equation $R_g^2 = (3/5)R^2$.

Nanoparticle Tracking Analysis (NTA). NTA measurements were performed on a NanoSight NS300 (Malvern Panalytical, UK) equipped with a 488 nm laser and analysed using the NTA software (version 3.4). The self-assemblies (5 mg/mL) were diluted by a factor of 10,000 with PBS solution and injected at a flow rate of 100 µL/min at room temperature. The diffusion of polymersomes was recorded over 60 s in five repetitive measurements. The hydrodynamic radii and their distributions were calculated from the diffusion using the Einstein-Stokes equation and averaged over all measurements.

Confocal Laser Scanning Microscopy (CLSM). CLSM images were recorded using a Zeiss 880 confocal laser scanning microscope (Zeiss, Germany), equipped with a Plan-Apochromat 20×/0.8 M27 objective and run by Zen Black software (Zeiss). BODIPY 630/650 dye was excited with a 633 nm He-Ne laser and resorufin was excited with a 561 nm diode pumped (DPS) laser. Images were recorded with an image size of 1024×1024 pixels, a bit depth of 16 bit and 1 Airy unit. Laser power and detector gain were kept constant for all measurements in order to enable fluorescence intensity comparisons between different images. Editing of the images and measuring the diameters of GUVs was done with the ImageJ software (NIH, USA), whereas fluorescence intensities were measured in Zen Blue software (Zeiss).

Quartz Crystal Microbalance with Dissipation monitoring (QCM-D). SUV adsorption on solid support was monitored by QCM-D on a Q-Sense E1 (Biolin Scientific, Sweden) using QSoft401 software. A gold QCM-D sensor (Q-Sense QSX 301, Biolin Scientific) was plasma-activated for 15 min immediately prior to use. Changes in the resonance frequency (Δf) and the dissipation (ΔD) were simultaneously recorded at 3rd, 5th, 7th, 11th and 13th overtone at room temperature. The data shown correspond to the 7th overtone. A Reglo Digital peristaltic pump (Ismatec, Switzerland) was used for sample injection. A typical protocol involved the following steps: Establishing a baseline in PBS at 100 µL/min; SUV adsorption (1 mg/mL) at 50 µL/min; washing with PBS at 100 µL/min; addition of a chiral compound (5 mg/mL for amino acids and PG homopolymers, 0.5 mg/mL for phospholipids, 1 mg/mL for (−)-menthol and SUVs) at 50 µL/min; washing with PBS at 100 µL/min. Subsequently the sensor was cleaned with water and ethanol. Data analysis was done in QSense Dfind software (version 1.2.7).

5.3. Syntheses

5.3.1. PBO-*b*-PG

Microwave-assisted synthesis. PBO and PG based polymers were synthesised on a Biotage Initiator System (Biotage, Sweden) equipped with Robot Eight. The temperature was monitored with an infrared sensor. The polymerisations were performed at a low absorption level after prestirring for 10 seconds at room temperature.

Synthesis of 1-ethoxy ethyl vinyl ether (EEGE). Racemic and enantiopure EEGE was synthesised following the common standard protocol.[215] Racemic or enantiopure glycidol (40.0 g, 0.54 mol, 1 eq) was dissolved in ethyl vinyl ether (EVE, 150 g, 2.08 mol, 3.85 eq), followed by the addition of *para*-

toluene sulfonic acid monohydrate (1.03 g, 5.40 mmol, 0,01 eq) over 15 min under ice cooling. The solution was stirred overnight while allowing to heat up to room temperature. The crude product mixture was washed three times with saturated aqueous sodium hydrogencarbonate solution. The organic phase was dried with magnesium sulfate and remaining EVE was evaporated on a rotary evaporator. The product was distilled in vacuum and the fraction evaporating at 65–72 °C (0.27 mbar) was collected (57.4 g, 0.39 mol, yield: 73%) and dried over calcium hydride before storing it under argon.

EEGE: ^{1}H-NMR (500 MHz, $CDCl_3$, 295 K, δ, ppm): 1.18 (t, 3H, -CH_2-CH_3), 1.30 (m, 3H, -CH-CH_3), 2.56–2.65 (m, 1H, epoxy-C$H_{2,\ cis}$), 2.78 (m, epoxy-C$H_{2,\ trans}$), 3.13 (m, 1H, epoxy-C*H*), 3.38–3.81 (m, 4H, -CH_2-O-CH(CH_3)-O-CH_2-CH_3), 4.74 (m, 1H, O-C*H*(CH_3)-O-).

Synthesis of poly(butylene oxide) (PBO). The synthesis is described for the racemic (*R*/*S*)-PBO_{27}. The isotactic (*S*)-PBO_{27} and (*R*)-PBO_{27} were synthesised similarly, using the same protocol and scales, by replacing the racemic (*R*/*S*)-BO by the respective enantiopure analogues. Potassium *tert*. butoxide solution (KO^{t}Bu, 0.25 mol/L in 1,4-dioxane, 9.25 mL, 2.31 mmol, 1 eq) was transferred into a 20 mL microwave vessel equipped with a magnetic stirrer in a glovebox under nitrogen. Afterwards, a solution of 18-crown-6 (0.50 mol/L in 1,4-dioxane, 2.31 mL, 1.16 mmol, 0.5 eq) was added. The vessel was closed and removed from the glovebox together with a syringe filled with racemic 1,2-butylene oxide ((*R*/*S*)-BO, 5.00g, 6.03 mL, 69.3 mmol, 30 eq). After adding (*R*/*S*)-BO to the reaction mixture through the septum of the lid, the microwave-assisted reaction was immediately started. A stepwise temperature increase was necessary in order to prevent the system from shutdown due to the slow heating rate caused by the high volume of the reaction solution. The following temperature program was applied: First heating step (two minutes at 50 °C), second heating step (two minutes at 60 °C), third heating step (30 min at 70 °C). After cooling to room temperature, methanol (2 mL) was added and stirred overnight in order to quench the reaction and to obtain hydroxy end groups. Subsequently, the solvents and unreacted monomer were evaporated using a rotary evaporator. The hydrophobic polymer, dissolved in *n*-hexane (100 mL), was washed with methanol (100 mL) in order to remove hydrophilic side products. The bottom, methanol enriched phase was then extracted three more times with *n*-hexane (each 100 mL). The combined *n*-hexane phases were then concentrated on a rotary evaporator. After drying overnight in high vacuum (0.05 mbar) the polymer was characterised and stored in a glovebox under nitrogen. 4.60 g (92%, M_n(NMR) = 2000 g/mol, 1.51 mmol, $Đ$(GPC) = 1.08) of colourless, viscous (*R*/*S*)-PBO_{27} were obtained.

(*R*/*S*)-PBO_{27}: ^{1}H-NMR (500 MHz, MeOD, 295 K, δ, ppm): 0.99 (m, 82H, -CH_2-CH_3), 1.23 (s, 9H, (H_3C)$_3$C-O-), 1.50–1.72 (m, 53H, -CH_2-CH_3), 3.39 (m, 27H, -CH_2-C*H*(CH_2-CH_3)-O-), 3.52 (m, 27H, -CHH_{cis}-CH(CH_2-CH_3)-O-), 3.67 (m, 26H, -CHH_{trans}-CH(CH_2-CH_3)-O-).

(*S*)-PBO_{27}: ^{1}H-NMR (500 MHz, MeOD, 295 K, δ, ppm): 0.99 (m, 84H, -CH_2-CH_3), 1.23 (s, 9H, (H_3C)$_3$C-O-), 1.50–1.72 (m, 55H, -CH_2-CH_3), 3.39 (m, 26H, -CH_2-CH(CH_2-CH_3)-O-), 3.54 (m, 26H, -CHH_{cis}-CH(CH_2-CH_3)-O-), 3.68 (m, 25H, -CHH_{trans}-CH(CH_2-CH_3)-O-).

(*R*)-PBO_{27}: ^{1}H-NMR (500 MHz, MeOD, 295 K, δ, ppm): 0.99 (m, 83H, -CH_2-CH_3), 1.23 (s, 9H, (H_3C)$_3$C-O-), 1.50–1.72 (m, 54H, -CH_2-CH_3), 3.39 (m, 26H, -CH_2-CH(CH_2-CH_3)-O-), 3.54 (m, 26H, -CHH_{cis}-CH(CH_2-CH_3)-O-), 3.67 (m, 25H, -CHH_{trans}-CH(CH_2-CH_3)-O-).

Synthesis of poly(butylene oxide)-*block*-poly(glycidol) (PBO-*b*-PG). The synthesis is described for the all-racemic (*R*/*S*)-PBO_{26}-*b*-(*R*/*S*)-PG_{14}. The isotactic (*S*)-PBO_{27}-*b*-(*S*)-PG_{14} and (*R*)-PBO_{26}-*b*-(*R*)-PG_{14} were synthesised similarly, using the same protocol and scales, by replacing the racemic (*R*/*S*)-EEGE by the respective enantiopure analogues. (*R*/*S*)-PBO_{27} (0.65 g, 0.32 mmol, 1 eq) was transferred into a 5 mL microwave vessel equipped with a magnetic stirrer in a glovebox under nitrogen. Then, 1,4-dioxane (2.61 mL) was added and the vessel was closed and shaken. Potassium naphthalenide (KNaph, 0.5 mol/L in THF, 0.64 mL, 0.32 mmol, 1 eq) was added to the solution dropwise under shaking through the septum of the lid. The equivalence point of the titration was determined visually by a dark green color of the solution that remained for at least two minutes. After stirring for another five minutes, the reaction vessel and a syringe filled with (*R*/*S*)-EEGE (0.64 g, 0.79 mL, 4.83 mmol, 15 eq) were removed from the glovebox. The monomer was added through the lid and the microwave-assisted polymerisation was immediately started. After running the reaction for 2.5 h at 70 °C, the vessel was cooled to room tempertaure and the polymerisation was quenched overnight by adding methanol (0.5 mL). The solvents were evaporated using a rotary evaporator and the acetal protecting groups of the crude copolymer were cleaved in 0.1M HCl in ethanol (20 mL) for 3 h. The acidic solution was then neutralised using 1 M NaOH in ethanol. After partly removing the solvent on a rotary evaporator, the same volume MilliQ water was added. The copolymer solution was then transferred into a regenerated cellulose dialysis membrane with a MWCO of 1 kDa (RC6, Spectra Por, USA) and dialysed for two days against a 1:1 water:ethanol mixture. After five exchanges of the solvent mixture, two more dialysis steps against pure water were performed. Eventually, the copolymer dispersion was lyophilised overnight. 922 mg (95%, M_n(NMR) = 3000 g/mol, 0.31 mmol, $Đ$(GPC) = 1.06) of colourless solid (*R*/*S*)-PBO_{27}-*b*-(*R*/*S*)-PG_{14} were obtained.

(*R*/*S*)-PBO_{26}-*b*-(*R*/*S*)-PG_{14}: ^{1}H-NMR (500 MHz, MeOD, 295 K, δ, ppm): 0.97 (m, 79H, -CH_2-CH_3), 1.21 (s, 9H, (H_3C)$_3$C-O-), 1.45–1.69 (m, 52H, -CH_2-CH_3), 3.37 (m, 25H, -CH_2-CH(CH_2-CH_3)-O-), 3.46–3.85 (m, 123H, -CH_2-CH(CH_2-CH_3)-O-, -CH_2-CH(CH_2-OH)-O-).

(*S*)-PBO_{27}-*b*-(*S*)-PG_{14}: ^{1}H-NMR (500 MHz, MeOD, 295 K, δ, ppm): 0.97 (m, 83H, -CH_2-CH_3), 1.21 (s, 9H, (H_3C)$_3$C-O-), 1.45–1.69 (m, 55H, -CH_2-CH_3), 3.37 (m, 28H, -CH_2-CH(CH_2-CH_3)-O-), 3.46–3.85 (m, 125H, -CH_2-CH(CH_2-CH_3)-O-, -CH_2-CH(CH_2-OH)-O-).

(*R*)-PBO$_{26}$-*b*-(*R*)-PG$_{14}$: ^{1}H-NMR (500 MHz, MeOD, 295 K, δ, ppm): 0.97 (m, 79H, -CH$_2$-C*H*$_3$), 1.21 (s, 9H, (*H*$_3$C)$_3$C-O-), 1.45–1.69 (m, 52H, -C*H*$_2$-CH$_3$), 3.37 (m, 25H, -CH$_2$-C*H*(CH$_2$-CH$_3$)-O-), 3.46–3.85 (m, 123H, -C*H*$_2$-CH(CH$_2$-CH$_3$)-O-, -C*H*$_2$-C*H*(C*H*$_2$-OH)-O-).

Synthesis of poly(glycidol) (PG). The synthesis is described for the racemic (*R*/*S*)-PG$_{30}$. The isotactic (*S*)-PG$_{30}$ and (*R*)-PG$_{28}$ were synthesised similarly, using the same protocol and scales, by replacing the racemic (*R*/*S*)-EEGE by the respective enantiopure analogues. Potassium *tert*. butoxide solution (KO^{t}Bu, 0.25 mol/L in 1,4-dioxane, 0.73 mL, 0.18 mmol, 1 eq) was transferred into a 5 mL microwave vessel equipped with a magnetic stirrer in a glovebox under nitrogen. The vessel was closed and removed from the glovebox together with a syringe filled with (*R*/*S*)-EEGE (0.80 g, 0.90 mL, 5.48 mmol, 30 eq). The monomer was added through the lid and the microwave-assisted polymerisation was immediately started. After running the reaction for 2.5 h at 70 °C, the vessel was cooled to room tempertaure and the polymerisation quenched overnight by adding methanol (0.5 mL). The solvents were evaporated using a rotary evaporator and the acetal protecting groups of the crude polymer were cleaved in 0.1M HCl in ethanol (10 mL) for 3 h. The acidic solution was then neutralised using 1 M NaOH in ethanol. The solution was then transferred into a regenerated cellulose dialysis membrane with a MWCO of 1 kDa (RC6, Spectra Por, USA) and dialysed for two days against ethanol with four exchanges of the solvent and eventually dried in vacuum. 350 mg (88%, M_n(NMR) = 2300 g/mol, 0.15 mmol, $Đ$(GPC) = 1.07) of colourless waxy (*R*/*S*)-PG$_{30}$ were obtained.

(*R*/*S*)-PG$_{30}$: ^{1}H-NMR (500 MHz, MeOD, 295 K, δ, ppm): 1.24 (s, 9H, (*H*$_3$C)$_3$C-O-), 3.52–3.93 (m, 150H, -C*H*$_2$-C*H*(C*H*$_2$-OH)-O-).

(*S*)-PG$_{30}$: ^{1}H-NMR (500 MHz, MeOD, 295 K, δ, ppm): 1.23 (s, 9H, (*H*$_3$C)$_3$C-O-), 3.52–3.93 (m, 148H, -C*H*$_2$-C*H*(C*H*$_2$-OH)-O-).

(*S*)-PG$_{28}$: ^{1}H-NMR (500 MHz, MeOD, 295 K, δ, ppm): 1.24 (s, 9H, (*H*$_3$C)$_3$C-O-), 3.52–3.93 (m, 141H, -C*H*$_2$-C*H*(C*H*$_2$-OH)-O-).

5.3.2. PDMS-*b*-PMOXA

Synthesis of monocarbinol-functionalised poly(dimethyl siloxane) (PDMS-OH). Hexamethyl-cyclotrisiloxane (D$_3$) (100 g, 0.450 mol) was put into a 250 mL one-neck round-bottom flask and dried over calcium hydride at 75 °C. After two days, D$_3$ was distilled under vacuum into a 250 mL three-neck round bottom flask with a yield of 90.32 g (0.406 mol, 13 eq). Dried cyclohexane (150 mL) was added, followed by dropwise addition of *n*-butyl lithium solution (12 mL, 30 mmol, 2.5 M in hexane, 1 eq). After stirring for 4 h, dried tetrahydrofuran (15 mL) was added and the reaction was left stirring for

38.5 h at room temperature. The polymerisation was quenched by addition of dimethylchlorosilane (9.46 g, 11.1 mL, 100 mmol, 3.2 eq). After 4 h of stirring, the solution was filtered through a glass frit to remove the precipitated lithium chloride salt. Then, the solvents were evaporated using a rotary evaporator and unreacted D_3 was removed *via* subsequent vacuum distillation. The remaining hydride-terminated PDMS-H (58.35 g, 31.5 mmol) was dissolved in dried toluene (80 mL), followed by the addition of 2-allyloxyethanol (3.76 g, 3.94 mL, 33.1 mmol) and platinum(0)-1,3-divinyl-1,1,3,3-tetramethyldisiloxane complex solution (Pt(dvs), in xylene, 35.9 µL). The flask was equipped with a reflux condenser and stirred overnight at 110 °C. Afterwards, toluene was removed using a rotary evaporator and the crude monocarbinol-functionalised PDMS-OH was dissolved in dichloromethane (100 mL). Activated charcoal was added, the solution stirred for 30 min and filtrated through Celite S. Finally the solvent was evaporated to yield $PDMS_{26}$-OH as a colorless oil (55.07 g, 55%, M_n(NMR) = 2000 g/mol, 27.5 mmol, $Đ$(GPC) = 1.17).

PDMS-H: ^{1}H-NMR (500 MHz, $CDCl_3$, 295 K, δ, ppm): 0.07 (m, 150H, -Si(CH_3)$_2$-), 0.53 (m, 2H, -Si-CH_2-), 0.88 (t, 3H, -CH_2-CH_3), 1.32 (m, 4H, -Si-CH_2-CH_2-CH_3), 4.70 (m, 1H, -Si-*H*).

PDMS-OH: ^{1}H-NMR (500 MHz, $CDCl_3$, 295 K, δ, ppm): 0.07 (m, 155H, -Si(CH_3)$_2$-), 0.53 (m, 4H, -Si-CH_2-), 0.88 (t, 3H, -CH_2-CH_3), 1.32 (m, 4H, -Si-CH_2-CH_2-CH_3), 1.63 (m, 2H, -Si-CH_2-CH_2-CH_2-O-), 3.44 (m, 2H, -Si-CH_2-CH_2-CH_2-O-), 3.54 (m, 2H, -O-CH_2-CH_2-OH), 3.73 (m, 2H, -O-CH_2-CH_2-OH).

Synthesis of poly(dimethyl siloxane)-*block*-poly(2-methyl-2-oxazoline) (PDMS-*b*-PMOXA). PDMS-OH (10 g, 4.89 mmol, 1 eq) was put into a 250 mL three-neck round-bottom flask and dried overnight at 100 °C under vacuum. After addition of dried hexane (85 mL) and dried and distilled triethylamine (0.643 g, 0.886 mL, 6.36 mmol, 1.3 eq) the solution was cooled with an ice/sodium chloride/acetone bath and stirred for 15 min. Then trifluormethanesulfonic anhydride (triflic anhydride, 1.66 g, 0.987 mL, 5.87 mmol, 1.2 eq) in hexane (15 mL) was added dropwise over 30 min under cooling. After 4 h stirring, the solution was filtered through a glass frit under inert atmosphere to remove the precipitated triflate salt. After evaporation of the solvent, the triflate-activated PDMS-OTf was obtained. Subsequently, dried ethylacetate (100 mL) and 2-methyl-2-oxazline (4.58 g, 4.56 mL, 53.8 mmol, 11 eq) were added and the solution was heated to 40 °C. After 63 h, the solution was cooled to room temperature and water (5 mL) and trimethylamine (5 mL) were added in parallel to quench the reaction. After 6 h, the solvents were evaporated using a rotary evaporator. The purification of the crude copolymer was done by dissolving in 300 mL methanol and subsequent centrifugation (4000 rpm, 1664 rfc, 10 min) to remove the remaining precipitated PDMS homopolymer. The solvent from the supernatant was evaporated and the copolymer (13.91 g) was dissolved in a 1:1 mixture of ethanol and water and dialysed against ethanol:water (1:1, 2 L in total). This solvent mixture was changed 5 times within two days, followed by a last dialysis step against water (2 L). The precipitated copolymer in water was lyophilised. The obtained purified copolymer (11.82 g) was not able to undergo self-assembly

into vesicular structures. Therefore, it was extracted in a 1:1 mixture of methanol and hexane (each 200 mL). The solvent from the bottom methanol-enriched phase was evaporated and the purified, vesicle-forming $PDMS_{25}$-*b*-$PMOXA_{10}$ was obtained as a slightly yellow gel (10.74 g, 74%, M_n = 2850 g/mol, 3.77 mmol, $Đ$(GPC) = 1.19).

PDMS-OTf: ^{1}H-NMR (500 MHz, $CDCl_3$, 295 K, δ, ppm): 0.07 (m, 157H, -Si(CH_3)$_2$-), 0.54 (m, 4H, -Si-CH_2-), 0.88 (t, 3H, -CH_2-CH_3), 1.32 (m, 4H, -Si-CH_2-CH_2-CH_3), 1.62 (m, 2H, -Si-CH_2-CH_2-CH_2-O-), 3.45 (m, 2H, -Si-CH_2-CH_2-CH_2-O-), 3.74 (m, 2H, -O-CH_2-CH_2-OH), 4.61 (m, 2H, -O-CH_2-CH_2-OTf).

PDMS-*b*-PMOXA: ^{1}H-NMR (500 MHz, $CDCl_3$, 295 K, δ, ppm): 0.07 (m, 152H, -Si(CH_3)$_2$-), 0.51 (m, 4H, -Si-CH_2-), 0.87 (t, 3H, -CH_2-CH_3), 1.31 (m, 4H, -Si-CH_2-CH_2-CH_3), 1.57 (m, 2H, -Si-CH_2-CH_2-CH_2-O-), 2.14 (m, 30H, -N-CO-CH_3), 3.46 (m, 43H, -O-CH_2-CH_2-N-CH_2-CH_2-N-), 3.80 (m, 2H, -N-CH_2-CH_2-OH).

5.4. Self-assembly

5.4.1. Nanoscale self-assembly

Solvent exchange. Self-assembly into nanoscopic self-assemblies was done at a concentration of 5 mg/mL at room temperature. 10 mg of the copolymer were dissolved in 0.4 mL THF in a 5 mL flask. 1.6 mL water or phosphate-buffered saline (PBS) were added under stirring at 300 rpm at an addition rate of 10 µL/min. After stirring overnight, the organic solvent was removed by dialysis against water or PBS using a regenerated cellulose membrane (MWCO 1 kDa, RC6, Spectra Por, USA). Water or PBS was exchanged four times within two days. If required, the SUVs were extruded using an Avanti Mini Extruder (USA) equipped with a 100 or 200 nm polycarbonate membrane in 15 passages.

Film rehydration. PBO-*b*-PG self-assembly into nanoscopic structures was done by dissolving 8 mg of the BCP in a 5 mL flask. 0.5 mL ethanol were added and the solvent was evaporated on a rotary evaporator at 40 °C, 40 rpm and 140 mbar until a dry polymer film was obtained. The film was rehydrated by adding 2 mL water and stirring for two days at room temperature at 600 rpm. PDMS-*b*-PMOXA self-assembly into nanoscopic structures was done similarly, however starting from 5 mg BCP dissolved in 1 mL ethanol and rehydrating with 1 mL PBS overnight. If required, the SUVs were extruded using an Avanti Mini Extruder (USA) equipped with a 100 nm polycarbonate membrane in 15 passages.

5.4.2. GUV formation

Film rehydration. Self-assembly into macroscopic GUVs was done *via* film rehydration. 50 µL of a 4 mg/mL polymer solution in ethanol were transferred into a plasma-activated glass vial. The film was deposited within 1 h by evaporating the solvent in a vacuum oven. Aqueous sucrose solution (700 µL, 300 mM) was added into the vial and the film was rehydrated by pipetting five times slowly up and down using an Eppendorf pipette. The dispersion was left standing overnight. Then, 200 µL of the polymer dispersion were transfered into a plasma-activated 8-well chamber plate and diluted with 200 µL PBS buffer. Bodipy dye solution (4 µL, 100 µM) was added, the dispersion was mixed slowly by pipetting up and down and afterwards imaged by CLSM.

Double emulsion microfluidics. Microscopic GUVs were assembled from double-emulsion templates created by microfluidics. Water-oil-water double emulsions were generated in a six-way junction microfluidic chip,[125] with defined flow rates using a three-module precision syringe pump (low pressure NEMESYS, Cetoni). A PBS solution containing 20 wt/v% poly(ethylene glycol) (PEG, 3000 Da) and 300 mM sucrose was used as inner aqueous phase (IA). This phase was enveloped by the polymer organic phase (PO), consisting of 4 mg/mL of the specific BCP dissolved in the solvent mixture, 3:2 hexane:cholorform (V:V), and subsequently broken up into double emulsions by the outer aqueous phase (OA), composed of 5 wt/v% poly(vinyl alcohol) (PVA, 18-23 kDa), 300 mM NaCl and 0.5 % (w/V) Pluronic® F-68. The flow rates for double emulsion formation were generally set to 2 µL/min (IA), 1 µl/min (PO) and 50 µL/min (OA), but optimised for every batch, and live imaging of this process was followed using a high-speed digital microscope (Meros, Dolomite). 198 µL of a double emulsion sample and 2 µL of a 100 µM aqueous BODIPY 630/650 solution were tranferred into a Nunc Lab-Tek eight-well chamber plate (Thermo Fisher Scientific, USA) and incubated at room temperature for 20 min. Within this time, GUVs were created from double emulsions, which settled to the bottom of the well for futher CLSM imaging.

5.5. Enzyme Reaction

OmpF expression. Wild-type OmpF was produced according to a modification of a previously published protocol:[168] Overnight precultures of E. coli BL21 (DE3) omp8[216] were grown in 6 mL lysogeny broth (LB) with 100 mg/L ampicillin at 37 °C and 150 rpm. 1 L of main culture (Terrific Broth (TB) with 100 mg/L ampicillin in 2.5 L Thomson Ultra Yield® flasks) was inoculated with 2x6 mL overnight culture and grown up to an OD_{600} of 1─2 (37 °C, 300 rpm). Isopropyl β-D-1-thiogalactopyranoside (IPTG) was added to a final concentration of 0.5 mM for induction of expression.

Expression cultures were further grown at 20 °C overnight (ca. 16 hrs.). For prevention of excess foam formation during expression, a drop of Antifoam 204 (Sigma-Aldrich) was added. Cells were harvested by centrifugation (20 min, 4 °C, 27500 rcf), then pellets were resuspended in lysis buffer kept on ice (10 mL lysis buffer per 1 g of pellet; 20 mM Tris-HCl, 2.5 mM $MgCl_2$, 1 mM $CaCl_2$) and subsequently homogenised by high-pressure homogenisation for 3 runs at max. 1100 bars (EmulsiFlex®-C3, Avestin, Inc.). A spatula tip of RNase A and DNase I (Roche Diagnostics GmbH), respectively, were added to the lysis suspension for a 30 min incubation at 37 °C. Sonication was conducted on ice for 10x (2 mins pulse 2 sec with 1 min breaks, amplitude 50). 1 mL 20% SDS per 10 mL of lysate was added for a 1 h incubation at 60°C. Membrane fragments were separated by centrifugation at 50,000 rcf at 20 °C. Pellets were washed with 2x3 mL 20 mM phosphate buffer, resuspended with a Dounce homogeniser in 0.125% octyl glucopyranoside (OG) in 20 mM phosphate buffer (3 mL per 1 g of pellet), incubated 1 h at 37 °C and centrifuged for 40 mins at RT. The last step was repeated using 3% OG in 20 mM phosphate buffer (1.5 mL per 1 g of pellet). The supernatant was analysed for concentration and purity of OmpF. Concentration was determined by UV/Vis spectroscopy (Nanodrop 2000c Spectrophotometer, Thermo Scientific) and calculated by Lambert-Beer's law ($\varepsilon_{OmpF,\ monomer}$ =54200 M^{-1} cm^{-1} or $\varepsilon_{OmpF,\ trimer}$=162630 M^{-1} cm^{-1}, $M_{OmpF,\ monomer}$=37.085 kDa).[217] Purity was determined by the 260/280 absorbance ratio (≤ 0.6, for absence of nucleic acid contamination) and by SDS-PAGE (12% gel, Figure 126).

OmpF dialysis. For preparation of OmpF reconstitution into polymer membranes, dialysis was conducted as previously published,[109] using Spectrum™ Spectra/Por™ Float-A-Lyzer™ G2 dialysis tubes (1 ml, 20 kDa MWCO). Alternatively, after the first dialysis step against 0.05% OG overnight, the first dialysis step against pure PBS was conducted over night, whereas the second dialysis step against PBS was conducted for 2 h, according to the standard protocol. If necessary, the dialysed OmpF in PBS was concentrated using the Spectra/Gel™ Absorbent. The final OmpF solution was either used freshly after dialysis, or stored at 4° C maximum over night for usage at the next day.

Formation of the microreactor. For the enzymatic microreactors, β-galactosidase (β-Gal) at a concentration of 0.25 mg/mL was added to the IA and 20 µL of the Outer membrane protein F (OmpF) solution at 69.5 ± 0.3 µM monomer concentration was added to 1 mL of the OA. For the negative control, no OmpF was added to the OA. The procedures for expression and purification of OmpF can be found in the Supporting Information. 180 µL of the GUV dispersion were transferred into a Nunc Lab-Tek eight-well chamber plate (Thermo Fisher Scientific, USA) and 10 µL of a proteinase K solution (1 mg/mL) was added. After 20 min, 10 µL of a β-D-galactopyranoside solution (RGP, 53 mM) was added and a CLSM timelapse over 2 h was started, recording one image per minute.

6. Publications related to this thesis

- S. Di Leone, M. Kyropoulou, J. Köchlin, **R. Wehr**, W. Meier, C. Palivan; *Soft Matter*, *submitted*
- **R. Wehr**, E. dos Santos, M. Muthwill, V. Chimisso, J. Gaitzsch, W. Meier; *Polym. Chem.*, **2021**, 12, 5377-5389
- C. Meyer, C. Schoenenberger, **R. Wehr**, D. Wu, C. Palivan; *Macromol. Biosci*., **2021**, 2100249
- C. Meyer, I. Craciun, C. Schoenenberger, **R. Wehr**, C. Palivan; *Nanoscale*, **2021**, 13, 66–70
- E. dos Santos, A. Belluati, D. Necula, D. Scherrer, C. Meyer, **R. Wehr**, E. Lörtscher, C. Palivan, W. Meier; *Adv. Mater*., **2020**, 32, 2004804
- **R. Wehr**, J. Gaitzsch, D. Daubian, C. Fodor, W. Meier; *RSC Adv*., **2020**, 10, 22701–22711
- S. Di Leone, S. Yorulmaz-Avsar, A. Belluati, **R. Wehr**, C. Palivan, W. Meier; *J. Phys. Chem. B*, **2020**, 124, 4454–4465
- M. Garni, **R. Wehr**, S. Yorulmaz-Avsar, C. John, C. Palivan, W. Meier; *Eur. Polym. J*., **2019**, 112, 346–364

7. References

1 G. Odian, *Principles of Polymerization*, John Wiley & Sons, Inc., Hoboken, NJ, USA, 2004.

2 N. Hadjichristidis, M. Pitsikalis and H. Iatrou, in *Block Copolymers I*, Springer-Verlag, Berlin/Heidelberg, pp. 1–124.

3 H. Feng, X. Lu, W. Wang, N. G. Kang and J. W. Mays, *Polymers (Basel).*, 2017, **9**, 494–524.

4 E. Konishcheva, D. Daubian, J. Gaitzsch and W. Meier, *Helv. Chim. Acta*, 2018, **101**, e1700287.

5 J. Herzberger, K. Niederer, H. Pohlit, J. Seiwert, M. Worm, F. R. Wurm and H. Frey, *Chem. Rev.*, 2016, **116**, 2170–2243.

6 D. Daubian, A. Fillion, J. Gaitzsch and W. Meier, *Macromolecules*, 2020, **53**, 11040–11050.

7 U. Capasso Palmiero, M. Sponchioni, N. Manfredini, M. Maraldi and D. Moscatelli, *Polym. Chem.*, 2018, **9**, 4084–4099.

8 J. Gaitzsch, M. Delahaye, A. Poma, F. Du Prez and G. Battaglia, *Polym. Chem.*, 2016, **7**, 3046–3055.

9 V. Agrahari and V. Agrahari, *Drug Discov. Today*, 2018, **23**, 1139–1151.

10 T. Meguro, S. Yoshida, K. Igawa, K. Tomooka and T. Hosoya, *Org. Lett.*, 2018, **20**, 4126–4130.

11 M. Szwarc, M. Levy and R. Milkovich, *J. Am. Chem. Soc.*, 1956, **78**, 2656–2657.

12 M. Szwarc, *Nature*, 1956, **178**, 1168–1169.

13 R. P. Quirk and B. Lee, *Polym. Int.*, 1992, **27**, 359–367.

14 A. D. Jenkins, P. Kratochvíl, R. F. T. Stepto and U. W. Suter, *Pure Appl. Chem.*, 1996, **68**, 2287–2311.

15 B. Tieke, *Makromolekulare Chemie*, Wiley-VCH, 3rd edn., 2014.

16 M. D. Lechner, K. Gehrke, E. H. Nordmeier and B. Tieke, *Makromolekulare Chemie*, Wiley-VCH, Berlin, Heidelberg, 3rd edn., 2014.

17 R. Hoogenboom and U. S. Schubert, *Macromol. Rapid Commun.*, 2007, **28**, 368–386.

18 R. Hoogenboom, U. S. Schubert and F. Wiesbrock, *Microwave-assisted Polymer Synthesis*, Springer International Publishing, 1st edn., 2016.

19 D. Daubian, J. Gaitzsch and W. Meier, *Polym. Chem.*, 2020, **11**, 1237–1248.

20 P. Priecel and J. A. Lopez-Sanchez, *ACS Sustain. Chem. Eng.*, 2019, **7**, 3–21.

21 D. Stevenson and I. D. Wilson, Eds., *Chiral Separations*, Springer US, Boston, MA, 1988.

22 T. J. Leitereg, D. G. Guadagni, J. Harris, T. R. Mon and R. Teranishi, *Nature*, 1971, **230**, 455–456.

23 L. A. Nguyen, H. He and C. Pham-Huy, *Int. J. Biomed. Sci.*, 2006, **2**, 85–100.

24 M. Cai, J. Gao and H. Wang, in *Membrane Biophysics*, Springer Singapore, Singapore, 2018, pp. 1–20.

25 D. W. van Krevelen and K. te Nijenhuis, *Properties of Polymers*, Elsevier, 4th edn., 2009.

26 A. Berthod, *Anal. Chem.*, 2006, **78**, 2093–2099.

27 J. C. Lang and D. W. Armstrong, *Curr. Opin. Colloid Interface Sci.*, 2017, **32**, 94–107.

28 X. Zhao, S. Q. Zang and X. Chen, *Chem. Soc. Rev.*, 2020, **49**, 2481–2503.

29 Y. Imamura, T. Fujita, Y. Kobayashi and S. Yamago, *Polym. Chem.*, 2020, **11**, 7042–7049.

30 H. Li, R. M. Shakaroun, S. M. Guillaume and J. F. Carpentier, *Chem. - A Eur. J.*, 2020, **26**, 128–138.

31 J. K. Awino and Y. Zhao, *Org. Biomol. Chem.*, 2017, **15**, 4851–4858.

32 J. Shen and Y. Okamoto, *Chem. Rev.*, 2016, **116**, 1094–1138.

33 X. Han, L. He, Q. Zhong, T. E. Beesley and D. W. Armstrong, *Chromatographia*, 2006, **63**, 13–23.

34 J. C. Worch, H. Prydderch, S. Jimaja, P. Bexis, M. L. Becker and A. P. Dove, *Nat. Rev. Chem.*, 2019, **3**, 514–535.

35 L. C. Preiss, L. Werber, V. Fischer, S. Hanif, K. Landfester, Y. Mastai and R. Muñoz-Espí, *Adv. Mater.*, 2015, **27**, 2728–2732.

36 L. Werber, L. C. Preiss, K. Landfester, R. Muñoz-Espí and Y. Mastai, *Chirality*, 2015, **27**, 613–618.

37 D. Prozeller, S. Morsbach and K. Landfester, *Nanoscale*, 2019, **11**, 19265–19273.

38 T. Wiseman, S. Williston, J. F. Brandts and L.-N. Lin, *Anal. Biochem.*, 1989, **179**, 131–137.

39 A. T. A. Jenkins, T. Neumann and A. Offenhäusser, *Langmuir*, 2001, **17**, 265–267.

40 A. R. Ferhan, J. A. Jackman and N. J. Cho, *Phys. Chem. Chem. Phys.*, 2017, **19**, 2131–2139.

41 E. Reimhult, F. Höök and B. Kasemo, *J. Chem. Phys.*, 2002, **117**, 7401–7404.

42 C. A. Keller and B. Kasemo, *Biophys. J.*, 1998, **75**, 1397–1402.

43 G. Liu and G. Zhang, *QCM-D Studies on Polymer Behavior at Interfaces*, Springer Berlin Heidelberg, Berlin, Heidelberg, 2013.

44 G. Sauerbrey, *Zeitschrift für Phys.*, 1959, **155**, 206–222.

45 M. Kyropoulou, S. Yorulmaz Avsar, C.-A. Schoenenberger, C. G. Palivan and W. P. Meier, *Nanoscale*, 2021, **13**, 6944–6952.

46 E. Reimhult, F. Höök and B. Kasemo, *Langmuir*, 2003, **19**, 1681–1691.

47 J. E. Bartenstein, X. Liu, K. Lange, P. M. Claesson and W. H. Briscoe, *J. Colloid Interface Sci.*, 2018, **512**, 260–271.

48 G. Van Meer, D. R. Voelker and G. W. Feigenson, *Nat. Rev. Mol. Cell Biol.*, 2008, **9**, 112–124.

49 T. Harayama and H. Riezman, *Nat. Rev. Mol. Cell Biol.*, 2018, **19**, 281–296.

50 A. Akbarzadeh, R. Rezaei-sadabady, S. Davaran, S. W. Joo and N. Zarghami, *Nanoscale Res. Lett.*, 2013, **8**, 1–9.

51 T. T. H. Thi, E. J. A. Suys, J. S. Lee, D. H. Nguyen, K. D. Park and N. P. Truong, *Vaccines*, 2021, **9**, 1–29.

52 K. Kita-Tokarczyk, J. Grumelard, T. Haefele and W. Meier, *Polymer (Guildf).*, 2005, **46**, 3540–3563.

53 M. Garni, R. Wehr, S. Y. Avsar, C. John, C. Palivan and W. Meier, *Eur. Polym. J.*, 2019, **112**, 346–364.

54 V. Percec, D. A. Wilson, P. Leowanawat, C. J. Wilson, A. D. Hughes, M. S. Kaucher, D. A. Hammer, D. H. Levine, A. J. Kim, F. S. Bates, K. P. Davis, T. P. Lodge, M. L. Klein, R. H. DeVane, E. Aqad, B. M. Rosen, A. O. Argintaru, M. J. Sienkowska, K. Rissanen, S. Nummelin and J. Ropponen, *Science (80-.).*, 2010, **328**, 1009–1014.

55 A. Najer, D. Wu, M. G. Nussbaumer, G. Schwertz, A. Schwab, M. C. Witschel, A. Schäfer, F. Diederich, M. Rottmann, C. G. Palivan, H.-P. Beck and W. Meier, *Nanoscale*, 2016, **8**, 14858–14869.

56 I. Yildirim, T. Bus, M. Sahn, T. Yildirim, D. Kalden, S. Hoeppener, A. Traeger, M. Westerhausen, C. Weber and U. S. Schubert, *Polym. Chem.*, 2016, **7**, 6064–6074.

57 F. Itel, M. Chami, A. Najer, S. Lörcher, D. Wu, I. A. Dinu and W. Meier, *Macromolecules*, 2014, **47**, 7588–7596.

58 B. M. Discher, Y. Y. Won, D. S. Ege, J. C. M. Lee, F. S. Bates, D. E. Discher and D. A. Hammer, *Science (80-.).*, 1999, **284**, 1143–1146.

59 F. Itel, A. Najer, C. G. Palivan and W. Meier, *Nano Lett.*, 2015, **15**, 3871–3878.

60 D. E. Discher and A. Eisenberg, *Science (80-.).*, 2002, **297**, 967–973.

61 C. Nardin, T. Hirt, J. Leukel and W. Meier, *Langmuir*, 2000, **16**, 1035–1041.

62 J. Du and S. P. Armes, *J. Am. Chem. Soc.*, 2005, **127**, 12800–12801.

63 H. Lomas, I. Canton, S. MacNeil, J. Du, S. P. Armes, A. J. Ryan, A. L. Lewis and G. Battaglia, *Adv. Mater.*, 2007, **19**, 4238–4243.

64 J. Gaitzsch, D. Appelhans, L. Wang, G. Battaglia and B. Voit, *Angew. Chemie Int. Ed.*, 2012, **51**, 4448–4451.

65 S. Moreno, B. Voit and J. Gaitzsch, *Colloid Polym. Sci.*, 2021, **299**, 309–324.

66 C. E. Meyer, J. Liu, I. Craciun, D. Wu, H. Wang, M. Xie, M. Fussenegger and C. G. Palivan, *Small*, 2020, **16**, 1–15.

67 E. Rideau, R. Dimova, P. Schwille, F. R. Wurm and K. Landfester, *Chem. Soc. Rev.*, 2018, **47**, 8572–8610.

68 G.-Z. Yin and X.-M. Yang, *J. Polym. Res.*, 2020, **27**, 38.

69 E. V. Konishcheva, U. E. Zhumaev, M. Kratt, V. Oehri and W. Meier, *Macromolecules*, 2017, **50**, 7155–7168.

70 P. Dimitrov, A. Porjazoska, C. P. Novakov, M. Cvetkovska and C. B. Tsvetanov, *Polymer (Guildf).*, 2005, **46**, 6820–6828.

71 M. E. J. Vleugels, M. E. De Zwart, J. R. Magana, B. A. G. Lamers, I. K. Voets, E. W. Meijer, K. Petkau-Milroy and A. R. A. Palmans, *Polym. Chem.*, 2020, **11**, 7170–7177.

72 M. Garni, S. Thamboo, C. A. Schoenenberger and C. G. Palivan, *Biochim. Biophys. Acta - Biomembr.*, 2017, **1859**, 619–638.

73 L. P. D. Ratcliffe, K. J. Bentley, R. Wehr, N. J. Warren, B. R. Saunders and S. P. Armes, *Polym. Chem.*, 2017, **8**, 5962–5971.

74 H. Che, S. Cao and J. C. M. Van Hest, *J. Am. Chem. Soc.*, 2018, **140**, 5356–5359.

75 X. Hu, Y. Zhang, Z. Xie, X. Jing, A. Bellotti and Z. Gu, *Biomacromolecules*, 2017, **18**, 649–673.

76 K. Knop, R. Hoogenboom, D. Fischer and U. S. Schubert, *Angew. Chemie - Int. Ed.*, 2010, **49**, 6288–6308.

77 C. Fruijtier-Pölloth, *Toxicology*, 2005, **214**, 1–38.

78 R. Webster, E. Didier, P. Harris, N. Siegel, J. Stadler, L. Tilbury and D. Smith, *Drug Metab. Dispos.*, 2007, **35**, 9–16.

79 F. M. Veronese and G. Pasut, *Drug Discov. Today*, 2005, **10**, 1451–1458.

80 P. J. Photos, L. Bacakova, B. Discher, F. S. Bates and D. E. Discher, *J. Control. Release*, 2003, **90**, 323–334.

81 S. Schöttler, G. Becker, S. Winzen, T. Steinbach, K. Mohr, K. Landfester, V. Mailänder and F. R. Wurm, *Nat. Nanotechnol.*, 2016, **11**, 372–377.

82 A. Pitto-Barry and N. P. E. Barry, *Polym. Chem.*, 2014, **5**, 3291–3297.

83 P. Zhang, F. Sun, S. Liu and S. Jiang, *J. Control. Release*, 2016, **244**, 184–193.

84 I. Hamad, A. C. Hunter, J. Szebeni and S. M. Moghimi, *Mol. Immunol.*, 2008, **46**, 225–232.

85 Q. Yang and S. K. Lai, *Wiley Interdiscip. Rev. Nanomedicine Nanobiotechnology*, 2015, **7**, 655–677.

86 S. M. Moghimi, A. C. Hunter, C. M. Dadswell, S. Savay, C. R. Alving and J. Szebeni, *Biochim. Biophys. Acta - Mol. Basis Dis.*, 2004, **1689**, 103–113.

87 T. Ishida and H. Kiwada, *Int. J. Pharm.*, 2008, **354**, 56–62.

88 V. Kumar and D. S. Kalonia, *AAPS PharmSciTech*, 2006, **7**, E47.

89 M. Barz, R. Luxenhofer, R. Zentel and M. J. Vicent, *Polym. Chem.*, 2011, **2**, 1900–1918.

90 A. Birke, J. Ling and M. Barz, *Prog. Polym. Sci.*, 2018, **81**, 163–208.

91 A. Thomas, S. S. Müller and H. Frey, *Biomacromolecules*, 2014, **15**, 1935–1954.

92 M. Gosecki, M. Gadzinowski, M. Gosecka, T. Basinska and S. Slomkowski, *Polymers (Basel).*, 2016, **8**, 1–25.

93 D. Taton, A. Le Borgne, M. Sepulchre and N. Spassky, *Macromol. Chem. Phys.*, 1994, **195**, 139–148.

94 E. J. Vandenberg, *J. Polym. Sci. Polym. Chem. Ed.*, 1985, **23**, 915–949.

95 H. Du, F. A. De Oliveira, L. J. C. Albuquerque, G. Tresset, E. Pavlova, C. Huin, P. Guégan and F. C. Giacomelli, *Langmuir*, 2020, **36**, 1266–1278.

96 N. Toncheva-Moncheva, P. Bakardzhiev, S. Rangelov, B. Trzebicka, A. Forys and P. D. Petrov, *Macromolecules*, 2019, **52**, 3435–3447.

97 Ł. Otulakowski, M. Gadzinowski, S. Slomkowski, T. Basinska, A. Forys, A. Dworak and B. Trzebicka, *Eur. Polym. J.*, 2018, **99**, 72–79.

98 B. Stoyanova, C. Novakov, C. B. Tsvetanov and S. Rangelov, *Macromol. Chem. Phys.*, 2016, **217**, 2380–2390.

99 S. Halacheva, S. Rangelov, C. Tsvetanov and V. M. Garamus, *Macromolecules*, 2010, **43**, 772–781.

100 P. Dimitrov, A. Utrata-Wesołek, S. Rangelov, W. Wałach, B. Trzebicka and A. Dworak, *Polymer (Guildf).*, 2006, **47**, 4905–4915.

101 S. Rangelov, S. Halacheva, V. M. Garamus and M. Almgren, *Macromolecules*, 2008, **41**, 8885–8894.

102 F. Marquardt, C. Stöcker, R. Gartzen, E. Heine, H. Keul and M. Möller, *Polymers (Basel).*, 2018, **10**, 96.

103 M. Imran Ul-Haq, B. F. L. Lai, R. Chapanian and J. N. Kizhakkedathu, *Biomaterials*, 2012, **33**, 9135–9147.

104 G. Gunkel, M. Weinhart, T. Becherer, R. Haag and W. T. S. Huck, *Biomacromolecules*, 2011, **12**, 4169–4172.

105 M. Grube, M. N. Leiske, U. S. Schubert and I. Nischang, *Macromolecules*, 2018, **51**, 1905–1916.

106 R. Hoogenboom, *Angew. Chemie - Int. Ed.*, 2009, **48**, 7978–7994.

107 C. E. Meyer, I. Craciun, C. A. Schoenenberger, R. Wehr and C. G. Palivan, *Nanoscale*, 2021, **13**, 66–70.

108 A. Belluati, V. Mikhalevich, S. Yorulmaz Avsar, D. Daubian, I. Craciun, M. Chami, W. P. Meier and C. G. Palivan, *Biomacromolecules*, 2020, **21**, 701–715.

109 M. Garni, T. Einfalt, R. Goers, C. G. Palivan and W. Meier, *ACS Synth. Biol.*, 2018, **7**, 2116–2125.

110 S. Egli, M. G. Nussbaumer, V. Balasubramanian, M. Chami, N. Bruns, C. Palivan and W. Meier, *J. Am. Chem. Soc.*, 2011, **133**, 4476–4483.

111 D. Wu, M. Spulber, F. Itel, M. Chami, T. Pfohl, C. G. Palivan and W. Meier, *Macromolecules*, 2014, **47**, 5060–5069.

112 S. Lörcher and W. Meier, *Eur. Polym. J.*, 2017, **88**, 575–585.

113 C. Gerstl, G. J. Schneider, W. Pyckhout-Hintzen, J. Allgaier, D. Richter, A. Alegría and J. Colmenero, *Macromolecules*, 2010, **43**, 4968–4977.

114 C. Booth, D. Attwood and C. Price, *Phys. Chem. Chem. Phys.*, 2006, **8**, 3612–3622.

115 L. Kunze, S. Y. Tseng, R. Schweins, T. Sottmann and H. Frey, *Langmuir*, 2019, **35**, 5221–5231.

116 L. Wang, J. Yao, X. Zhang, Y. Zhang, C. Xu, R. J. Lee, G. Yu, B. Yu and L. Teng, *Colloids Surfaces B Biointerfaces*, 2018, **161**, 464–470.

117 E. Villar-Alvarez, E. Figueroa-Ochoa, S. Barbosa, J. F. A. Soltero, P. Taboada and V. Mosquera, *RSC Adv.*, 2015, **5**, 52105–52120.

118 A. Cambón, J. Brea, M. I. Loza, C. Alvarez-Lorenzo, A. Concheiro, S. Barbosa, P. Taboada and V. Mosquera, *Mol. Pharm.*, 2013, **10**, 3232–3241.

119 G. Battaglia and A. J. Ryan, *J. Phys. Chem. B*, 2006, **110**, 10272–10279.

120 M. P. Wolf, G. B. Salieb-Beugelaar and P. Hunziker, *Prog. Polym. Sci.*, 2018, **83**, 97–134.

121 A. Victor, J. Ribeiro and F. F. Araújo, *J. Mech. Eng. Biomech.*, 2019, **4**, 1–9.

122 H. Steinfink, B. Post and I. Fankuchen, *Acta Crystallogr.*, 1955, **8**, 420–424.

123 M. Fauquignon, E. Ibarboure, S. Carlotti, A. Brûlet, M. Schmutz and J.-F. Le Meins, *Polymers (Basel).*, 2019, **11**, 2013.

124 A. Belluati, I. Craciun, J. Liu and C. G. Palivan, *Biomacromolecules*, 2018, **19**, 4023–4033.

125 E. C. dos Santos, A. Belluati, D. Necula, D. Scherrer, C. E. Meyer, R. P. Wehr, E. Lörtscher, C. G. Palivan and W. Meier, *Adv. Mater.*, 2020, **32**, 1–13.

126 C. L. Elkins and T. E. Long, *Macromolecules*, 2004, **37**, 6657–6659.

127 J. Bauer, N. Hüsing and G. Kickelbick, *J. Polym. Sci. Part A Polym. Chem.*, 2002, **40**, 1539–1551.

128 H. Kazama, Y. Tezuka and K. Imai, *Polym. J.*, 1987, **19**, 1091–1100.

129 B. Van Genabeek, B. F. M. De Waal, M. M. J. Gosens, L. M. Pitet, A. R. A. Palmans and E. W. Meijer, *J. Am. Chem. Soc.*, 2016, **138**, 4210–4218.

130 B. Van Genabeek, B. F. M. De Waal, B. Ligt, A. R. A. Palmans and E. W. Meijer, *ACS Macro Lett.*, 2017, **6**, 674–678.

131 N. S. Cameron, M. K. Corbierre and A. Eisenberg, *Can. J. Chem.*, 1999, **77**, 1311–1326.

132 H. Shen and A. Eisenberg, *Angew. Chemie*, 2000, **39**, 3310–3312.

133 E. Rakhmatullina, T. Braun, M. Chami, V. Malinova and W. Meier, *Langmuir*, 2007, **23**, 12371–12379.

134 O. Terreau, L. Luo and A. Eisenberg, *Langmuir*, 2003, **19**, 5601–5607.

135 D. M. Cooke and A.-C. Shi, *Macromolecules*, 2006, **39**, 6661–6671.

136 D. J. Adams, M. F. Butler and A. C. Weaver, *Langmuir*, 2006, **22**, 4534–4540.

137 W. Zhang, L. Shi, Y. An, L. Gao, K. Wu, R. Ma and B. He, *Phys. Chem. Chem. Phys.*, 2004, **6**, 109.

138 R. T. Pearson, N. J. Warren, A. L. Lewis, S. P. Armes and G. Battaglia, *Macromolecules*, 2013, **46**, 1400–1407.

139 Y. Jiang, T. Chen, F. Ye, H. Liang and A.-C. Shi, *Macromolecules*, 2005, **38**, 6710–6717.

140 J. Gaitzsch, X. Huang and B. Voit, *Chem. Rev.*, 2016, **116**, 1053–1093.

141 A. Blanazs, S. P. Armes and A. J. Ryan, *Macromol. Rapid Commun.*, 2009, **30**, 267–277.

142 C. Lebleu, L. Rodrigues, J. M. Guigner, A. Brûlet, E. Garanger and S. Lecommandoux, *Langmuir*, 2019, **35**, 13364–13374.

143 M. Dionzou, A. Morère, C. Roux, B. Lonetti, J. D. Marty, C. Mingotaud, P. Joseph, D. Goudounèche, B. Payré, M. Léonetti and A. F. Mingotaud, *Soft Matter*, 2016, **12**, 2166–2176.

144 D. A. Christian, S. Cai, D. M. Bowen, Y. Kim, J. D. Pajerowski and D. E. Discher, *Eur. J. Pharm. Biopharm.*, 2009, **71**, 463–474.

145 Y.-Y. Won, A. K. Brannan, H. T. Davis and F. S. Bates, *J. Phys. Chem. B*, 2002, **106**, 3354–3364.

146 P. V. Pawar, S. V. Gohil, J. P. Jain and N. Kumar, *Polym. Chem.*, 2013, **4**, 3160.

147 J. Zhou, R. Ni and Y. Chau, *RSC Adv.*, 2017, **7**, 17997–18000.

148 J. Gaitzsch, S. Hirschi, S. Freimann, D. Fotiadis and W. Meier, *Nano Lett.*, 2019, **19**, 2503–2508.

149 L. P. D. Ratcliffe, M. J. Derry, A. Ianiro, R. Tuinier and S. P. Armes, *Angew. Chemie - Int. Ed.*, 2019, **58**, 18964–18970.

150 J. E. Bartenstein, J. Robertson, G. Battaglia and W. H. Briscoe, *Colloids Surfaces A Physicochem. Eng. Asp.*, 2016, **506**, 739–746.

151 P. Walde, K. Cosentino, H. Engel and P. Stano, *ChemBioChem*, 2010, **11**, 848–865.

152 M. Lomora, F. Itel, I. A. Dinu and C. G. Palivan, *Phys. Chem. Chem. Phys.*, 2015, **17**, 15538–15546.

153 J. Thiele, D. Steinhauser, T. Pfohl and S. Förster, *Langmuir*, 2010, **26**, 6860–6863.

154 D. F. do Nascimento, L. R. Arriaga, M. Eggersdorfer, R. Ziblat, M. de F. V. Marques, F. Reynaud, S. A. Koehler and D. A. Weitz, *Langmuir*, 2016, **32**, 5350–5355.

155 E. Amstad, *Chimia (Aarau).*, 2017, **71**, 334–341.

156 E. Amstad, S. H. Kim and D. A. Weitz, *Angew. Chemie - Int. Ed.*, 2012, **51**, 12499–12503.

157 L. Brown, S. L. McArthur, P. C. Wright, A. Lewis and G. Battaglia, *Lab Chip*, 2010, **10**, 1922.

158 J. Habel, A. Ogbonna, N. Larsen, S. Cherré, S. Kynde, S. R. Midtgaard, K. Kinoshita, S. Krabbe, G. V. Jensen, J. S. Hansen, K. Almdal and C. Hèlix-Nielsen, *RSC Adv.*, 2015, **5**, 79924–79946.

159 W. Burchard, *Light Scatt. from Polym.*, 2007, 1–124.

160 S. U. Egelhaaf and P. Schurtenberger, *J. Phys. Chem.*, 1994, **98**, 8560–8573.

161 K. Jaskiewicz, M. M. Makowski, M. Kappl, K. Landfester and A. Kroeger, *Langmuir*, 2012, 2–4.

162 A. Czajka and S. P. Armes, *Chem. Sci.*, 2020, **11**, 11443–11454.

163 O. Jalmar, L. François-Moutal, A.-J. García-Sáez, M. Perry, T. Granjon, F. Gonzalvez, E. Gottlieb, J. Ayala-Sanmartin, B. Klösgen, P. Schwille and P. X. Petit, *PLoS One*, 2013, **8**, e55250.

164 Y. Men, F. Peng, Y. Tu, J. C. M. van Hest and D. A. Wilson, *Polym. Chem.*, 2016, **7**, 3977–3982.

165 G. Kefala, C. Ahn, M. Krupa, L. Esquivies, I. Maslennikov, W. Kwiatkowski and S. Choe, *Protein Sci.*, 2010, **19**, 1117–1125.

166 J. Habel, M. Hansen, S. Kynde, N. Larsen, S. R. Midtgaard, G. V. Jensen, J. Bomholt, A. Ogbonna, K. Almdal, A. Schulz and C. Hélix-Nielsen, *Membranes (Basel).*, 2015, **5**, 307–351.

167 M. Lomora, M. Garni, F. Itel, P. Tanner, M. Spulber and C. G. Palivan, *Biomaterials*, 2015, **53**, 406–414.

168 M. Grzelakowski, O. Onaca, P. Rigler, M. Kumar and W. Meier, *Small*, 2009, **5**, 2545–2548.

169 M. Antonietti and S. Förster, *Adv. Mater.*, 2003, **15**, 1323–1333.

170 L. Messager, J. Gaitzsch, L. Chierico and G. Battaglia, *Curr. Opin. Pharmacol.*, 2014, **18**, 104–111.

171 N. Chuard, G. Gasparini, D. Moreau, S. Lörcher, C. Palivan, W. Meier, N. Sakai and S. Matile, *Angew. Chemie - Int. Ed.*, 2017, **56**, 2947–2950.

172 C. Sanson, C. Schatz, J.-F. Le Meins, A. Soum, J. Thévenot, E. Garanger and S. Lecommandoux, *J. Control. Release*, 2010, **147**, 428–435.

173 L. Wang, L. Chierico, D. Little, N. Patikarnmonthon, Z. Yang, M. Azzouz, J. Madsen, S. P. Armes and G. Battaglia, *Angew. Chemie Int. Ed.*, 2012, **51**, 11122–11125.

174 T. Einfalt, R. Goers, I. A. Dinu, A. Najer, M. Spulber, O. Onaca-Fischer and C. G. Palivan, *Nano Lett.*, 2015, **15**, 7596–7603.

175 R. B. Liebherr, A. Hutterer, M. J. Mickert, F. C. Vogl, A. Beutner, A. Lechner, H. Hummel and H. H. Gorris, *Anal. Bioanal. Chem.*, 2015, **407**, 7443–7452.

176 T. Einfalt, D. Witzigmann, C. Edlinger, S. Sieber, R. Goers, A. Najer, M. Spulber, O. Onaca-Fischer, J. Huwyler and C. G. Palivan, *Nat. Commun.*, 2018, **9**, 1127.

177 M. Marguet, C. Bonduelle and S. Lecommandoux, *Chem. Soc. Rev.*, 2013, **42**, 512–529.

178 A. Belluati, S. Thamboo, A. Najer, V. Maffeis, C. von Planta, I. Craciun, C. G. Palivan and W. Meier, *Adv. Funct. Mater.*, , DOI:10.1002/adfm.202002949.

179 S. Thamboo, A. Najer, A. Belluati, C. von Planta, D. Wu, I. Craciun, W. Meier and C. G. Palivan, *Adv. Funct. Mater.*, 2019, **29**, 1–12.

180 W. Shi, A. J. McGrath, Y. Li, N. A. Lynd, C. J. Hawker, G. H. Fredrickson and E. J. Kramer, *Macromolecules*, 2015, **48**, 3069–3079.

181 H. F. Wang, K. C. Yang, W. C. Hsu, J. Y. Lee, J. T. Hsu, G. M. Grason, E. L. Thomas, J. C. Tsai and R. M. Ho, *Proc. Natl. Acad. Sci. U. S. A.*, 2019, **116**, 4080–4089.

182 N. Petzetakis, A. P. Dove and R. K. O'Reilly, *Chem. Sci.*, 2011, **2**, 955–960.

183 N. Petzetakis, D. Walker, A. P. Dove and R. K. O'Reilly, *Soft Matter*, 2012, **8**, 7408–7414.

184 L. Sun, N. Petzetakis, A. Pitto-Barry, T. L. Schiller, N. Kirby, D. J. Keddie, B. J. Boyd, R. K. O'Reilly and A. P. Dove, *Macromolecules*, 2013, **46**, 9074–9082.

185 K. Petkau-Milroy, A. Ianiro, M. M. L. Ahn, J. R. Magana, M. E. J. Vleugels, B. A. G. Lamers, R. Tuinier, I. K. Voets, A. R. A. Palmans and E. W. Meijer, *ACS Macro Lett.*, 2020, **9**, 38–42.

186 A. Das, K. Petkau-Milroy, G. Klerks, B. Van Genabeek, R. P. M. Lafleur, A. R. A. Palmans and E. W. Meijer, *ACS Macro Lett.*, 2018, **7**, 546–550.

187 Z. Li, R. Liu, B. Mai, S. Feng, Q. Wu, G. Liang, H. Gao and F. Zhu, *Polym. Chem.*, 2013, **4**, 954–960.

188 H. Liang, Q. Zhou, Y. Long, W. Wei, S. Feng, G. Liang and F. Zhu, *RSC Adv.*, 2018, **8**, 12752–12759.

189 R. Wehr, J. Gaitzsch, D. Daubian, C. Fodor and W. Meier, *RSC Adv.*, 2020, **10**, 22701–22711.

190 R. Wehr, E. C. dos Santos, M. S. Muthwill, V. Chimisso, J. Gaitzsch and W. Meier, *Polym. Chem.*, 2021, **12**, 5377–5389.

191 J. Ding, C. Price and C. Booth, *Eur. Polym. J.*, 1991, **27**, 891–894.

192 J. Ding, F. Heatley, C. Price and C. Booth, *Eur. Polym. J.*, 1991, **27**, 895–899.

193 J. Allgaier, C. H. Hövelmann, Z. Wei, M. Staropoli, W. Pyckhout-Hintzen, N. Lühmann and S. Willbold, *RSC Adv.*, 2016, **6**, 6093–6106.

194 A. J. McGrath, W. Shi, C. G. Rodriguez, E. J. Kramer, C. J. Hawker and N. A. Lynd, *Polym. Chem.*, 2015, **6**, 1465–1473.

195 A. L. Brocas, C. Mantzaridis, D. Tunc and S. Carlotti, *Prog. Polym. Sci.*, 2013, **38**, 845–873.

196 M. Hans, H. Keul and M. Moeller, *Polymer (Guildf).*, 2009, **50**, 1103–1108.

197 A. A. Toy, S. Reinicke, A. H. E. Müller and H. Schmalz, *Macromolecules*, 2007, **40**, 5241–5244.

198 M. Siebert, H. Keul and M. Möller, *Des. Monomers Polym.*, 2010, **13**, 547–563.

199 M. Erberich, H. Keul and M. Möller, *Macromolecules*, 2007, **40**, 3070–3079.

200 F. Wurm, J. Nieberle and H. Frey, *Macromolecules*, 2008, **41**, 1184–1188.

201 F. Wurm, U. Kemmer-Jonas and H. Frey, *Polym. Int.*, 2009, **58**, 989–995.

202 F. C. Schilling and A. E. Tonelli, *Macromolecules*, 1986, **19**, 1337–1343.

203 B. Wu, C. J. Harlan, R. W. Lenz and A. R. Barron, *Macromolecules*, 1997, **30**, 316–318.

204 B. Antelmann, M. H. Chisholm, S. S. Iyer, J. C. Huffman, D. Navarro-Llobet, M. Pagel, W. J. Simonsick and W. Zhong, *Macromolecules*, 2001, **34**, 3159–3175.

205 M. H. Chisholm and D. Navarro-Llobet, *Macromolecules*, 2002, **35**, 2389–2392.

206 M. A. B. Block and S. Hecht, *Macromolecules*, 2008, **41**, 3219–3227.

207 G. Liu, X. Li, J. Sheng, P.-Z. Li, W. K. Ong, S. Z. F. Phua, H. Ågren, L. Zhu and Y. Zhao, *ACS Nano*, 2017, **11**, 11880–11889.

208 Y. Wang, S. S. Funari and J. F. Mano, *Macromol. Chem. Phys.*, 2006, **207**, 1262–1271.

209 J. A. Faucher, *J. Polym. Sci. Part B Polym. Lett.*, 1965, **3**, 143–145.

210 S. Di Leone, S. Di Leone, S. Y. Avsar, A. Belluati, R. Wehr, C. G. Palivan and W. Meier, *J. Phys. Chem. B*, 2020, **124**, 4454–4465.

211 S. Galindo-Rodriguez, E. Allémann, H. Fessi and E. Doelker, *Pharm. Res.*, 2004, **21**, 1428–1439.

212 A. Blanazs, A. J. Ryan and S. P. Armes, *Macromolecules*, 2012, **45**, 5099–5107.

213 R. Górecki, F. Antenucci, K. Norinkevicius, L. Elmstrøm Christiansen, S. T. Myers, K. Trzaskuś and C. Hélix-Nielsen, *Langmuir*, 2021, **37**, 2079–2090.

214 R. Stoenescu, A. Graff and W. Meier, *Macromol. Biosci.*, 2004, **4**, 930–935.

215 A. O. Fitton, J. Hill, D. E. Jane and R. Millar, *Synthesis (Stuttg).*, 1987, **1987**, 1140–1142.

216 A. Prilipov, P. S. Phale, P. Van Gelder, J. P. Rosenbusch and R. Koebnik, *FEMS Microbiol. Lett.*, 1998, **163**, 65–72.

217 R. Chen, C. Krämer, W. Schmidmayr, U. Chen-Schmeisser and U. Henning, *Biochem. J.*, 1982, **203**, 33–43.

218 J. E. Mark and P. J. Flory, *J. Am. Chem. Soc.*, 1965, **87**, 1415–1423.

8. Appendix

8.1. Synthesis and self-assembly of atactic PBO-*b*-PG

8.1.1. BCP characterisation

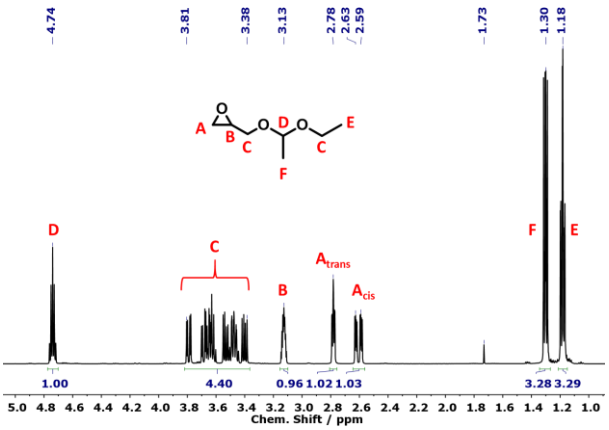

Figure 91: ^{1}H NMR spectrum of racemic EEGE in $CDCl_3$.

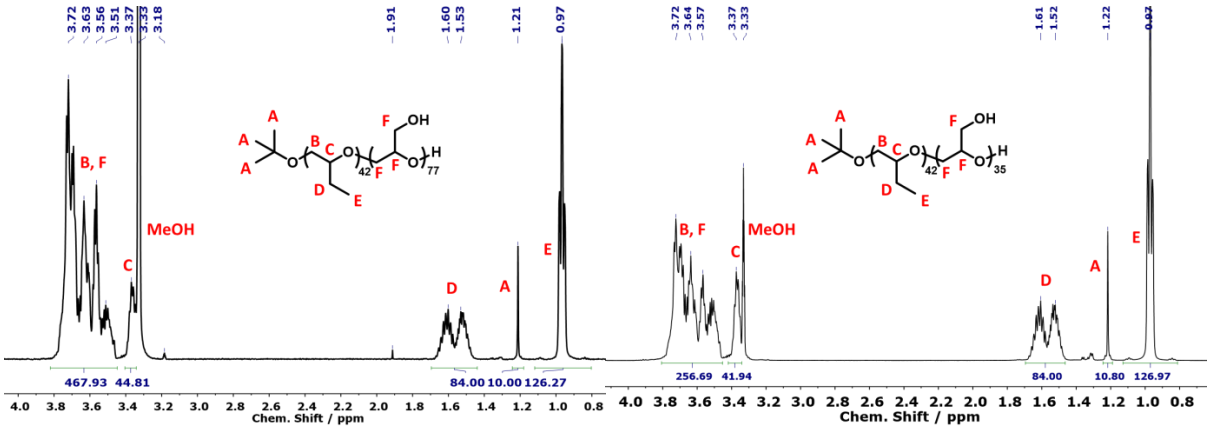

Figure 92: ^{1}H NMR spectrum of PBO_{42}-*b*-PG_{77} (left) and PBO_{42}-*b*-PG_{35} (right) in MeOD.

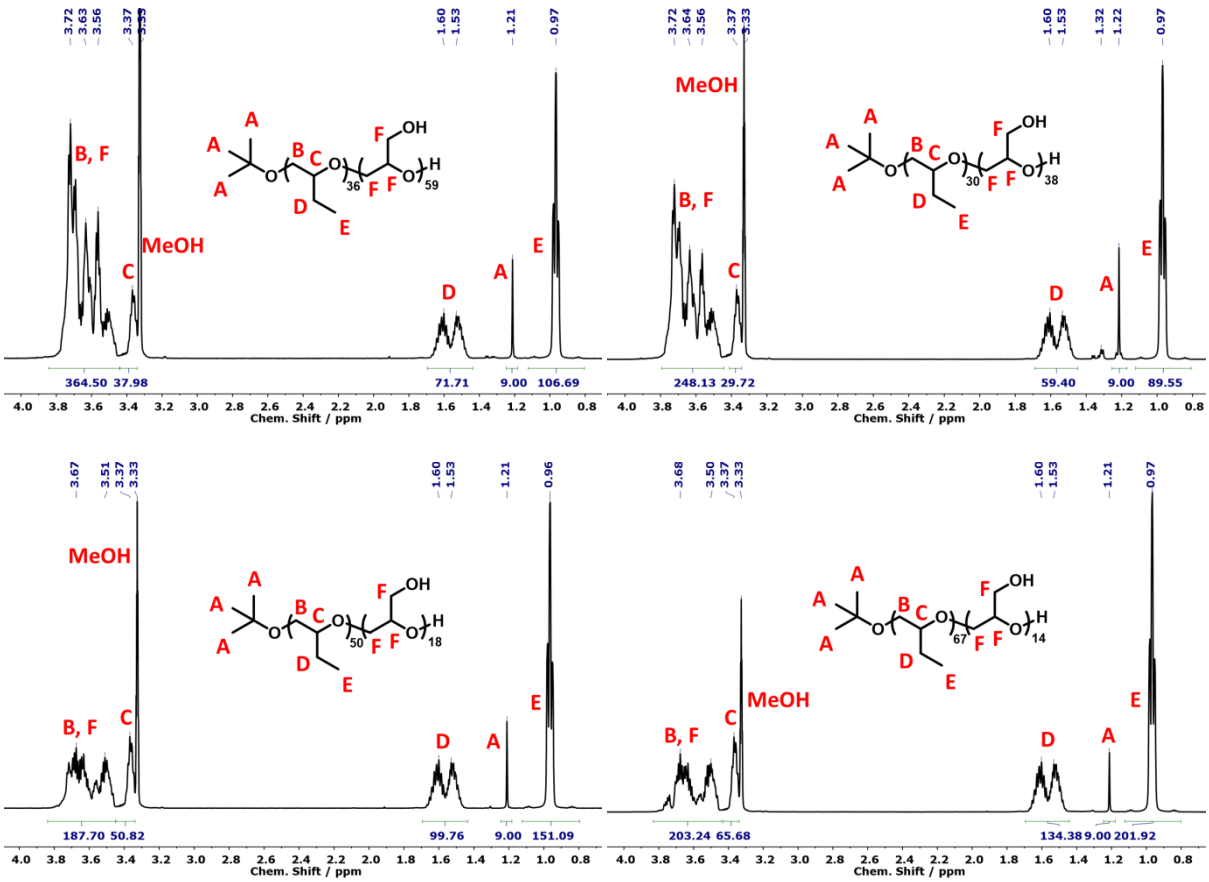

Figure 93: ^{1}H NMR spectra of PBO_{36}-*b*-PG_{59} (top left), PBO_{30}-*b*-PG_{38} (top right), PBO_{50}-*b*-PG_{18} (bottom left) and PBO_{67}-*b*-PG_{14} (bottom right) in MeOD.

8.1.2. Self-assembly characterisation

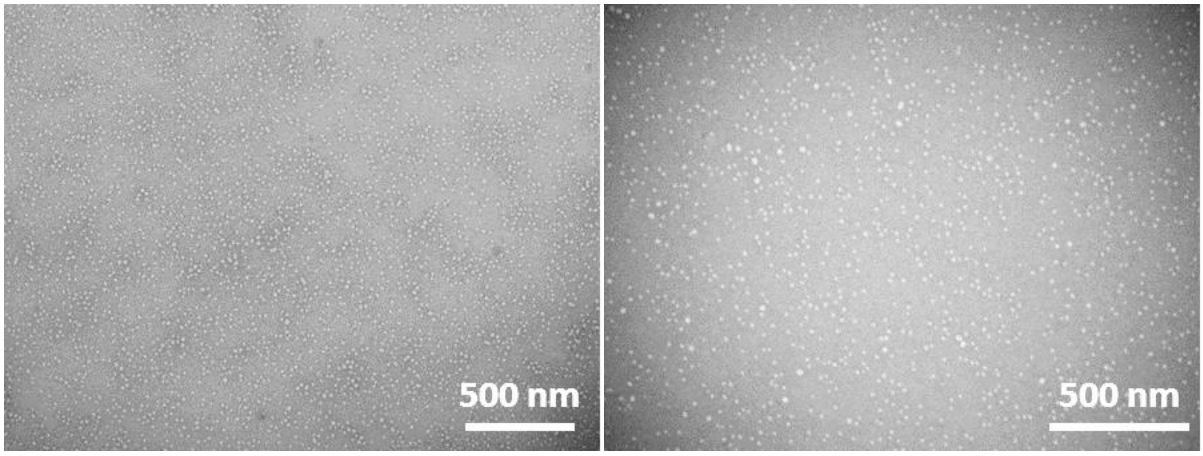

Figure 94: Additional TEM images of micelles formed by solvent exchange from PBO_{42}-*b*-PG_{77}.

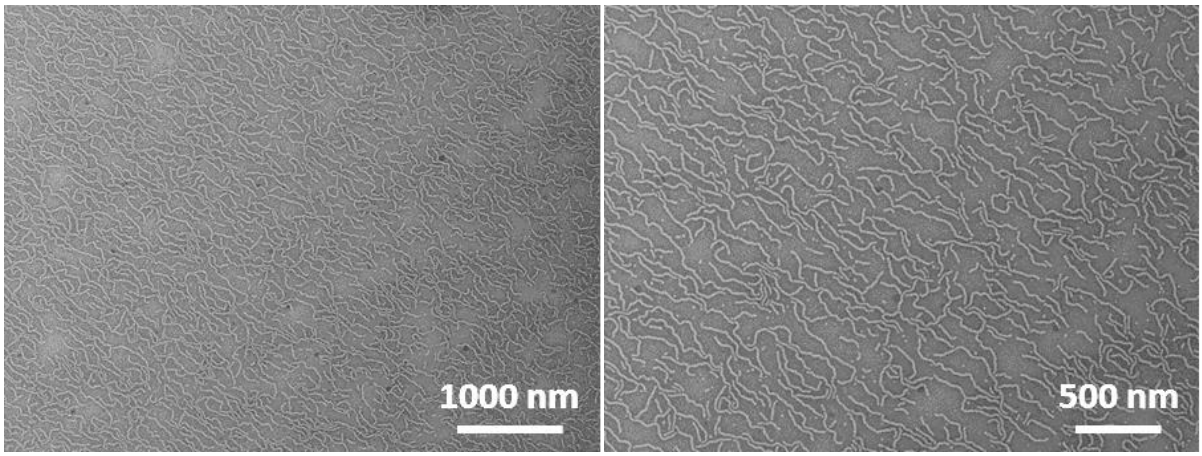

Figure 95: Additional TEM images of worms formed by solvent exchange from PBO_{42}-*b*-PG_{35}.

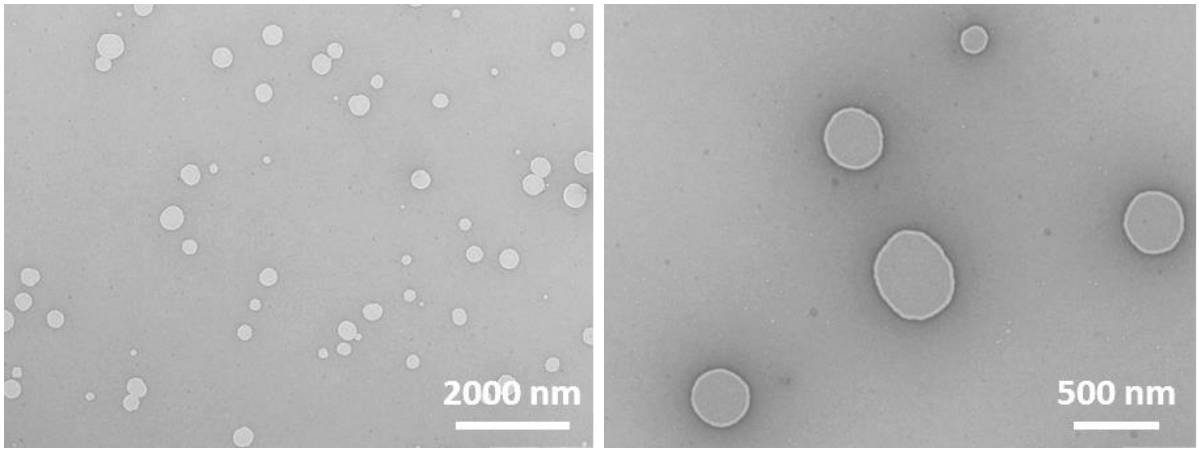

Figure 96: Additional TEM images of SUVs after extrusion with a 200 nm membrane formed by solvent exchange from PBO_{42}-*b*-PG_{21}.

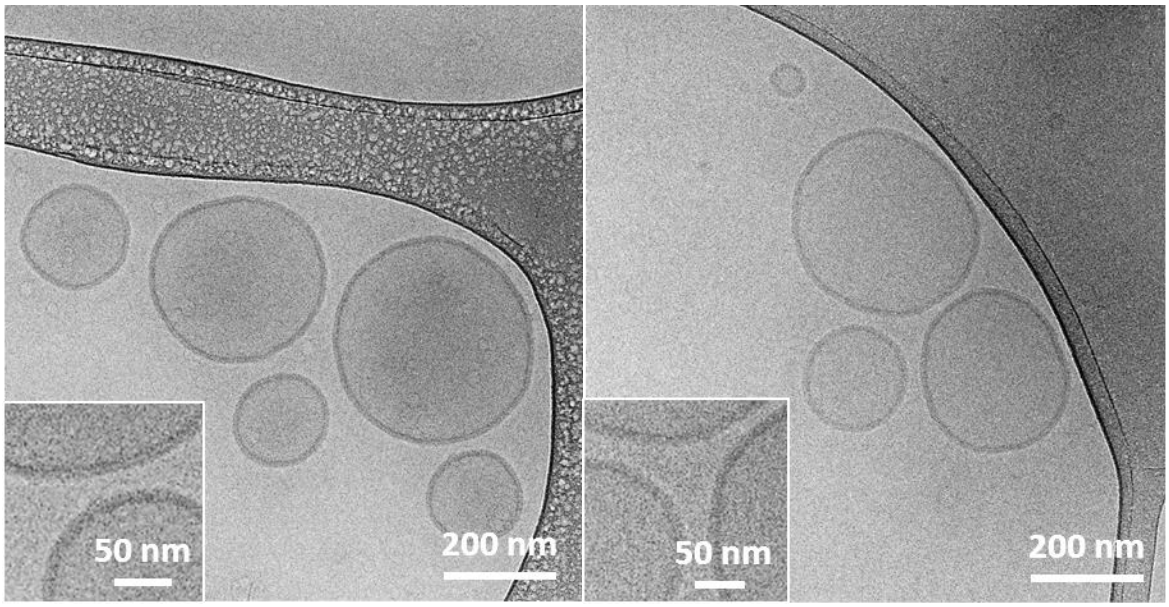

Figure 97: Additional Cryo-TEM images of SUVs after extrusion with a 200 nm membrane formed by solvent exchange from PBO_{42}-*b*-PG_{21}. The insets show the polymer membrane in detail.

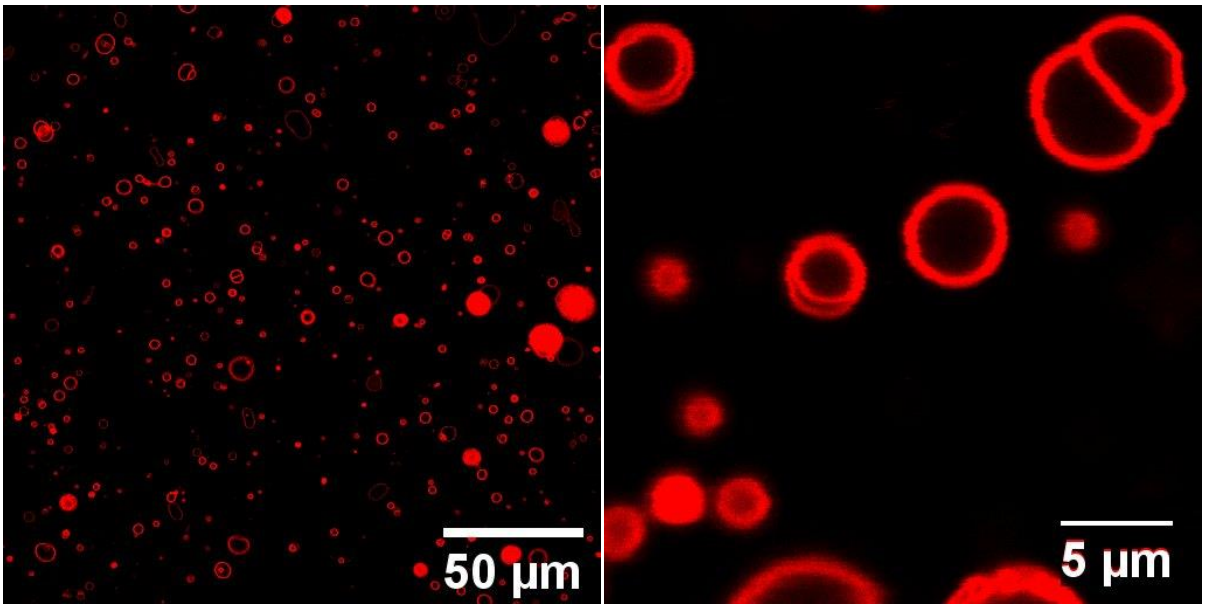

Figure 98: Additional CLSM images of the GUVs formed by film rehydration from PBO_{42}-*b*-PG_{21}.

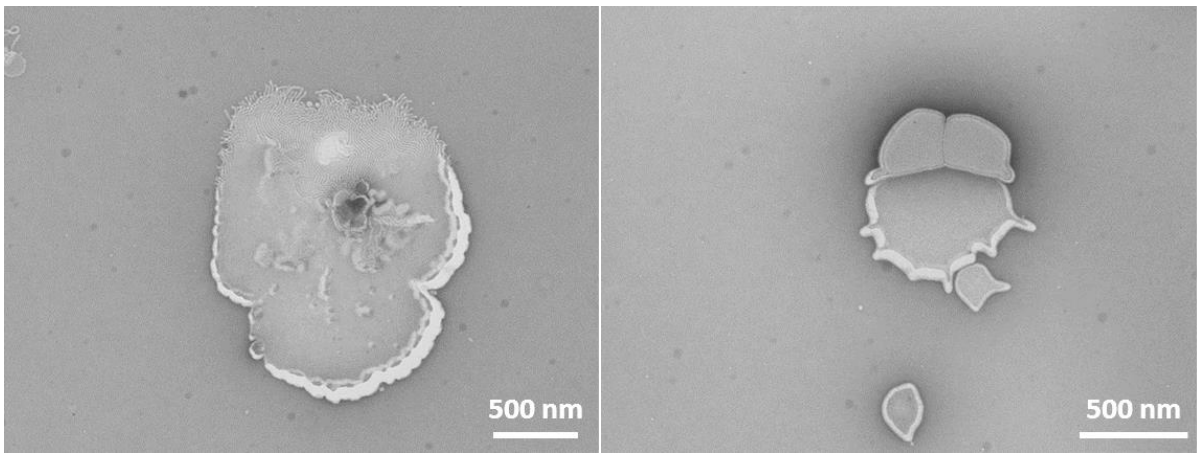

Figure 99: Additional TEM images of the self-assemblies formed by film rehydration from PBO_{42}-*b*-PG_{21}.

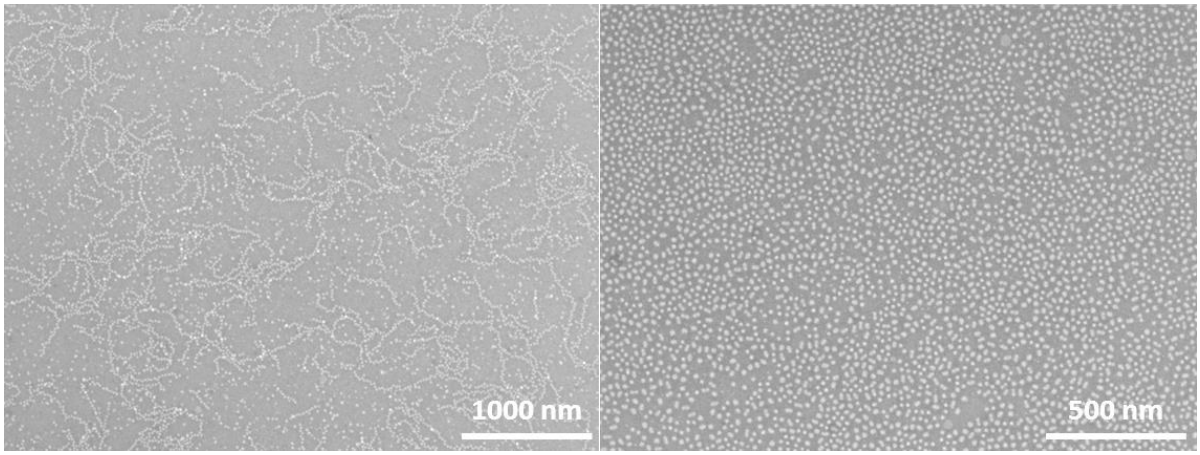

Figure 100: Additional TEM images of the self-assemblies formed by film rehydration from PBO_{42}-*b*-PG_{77}.

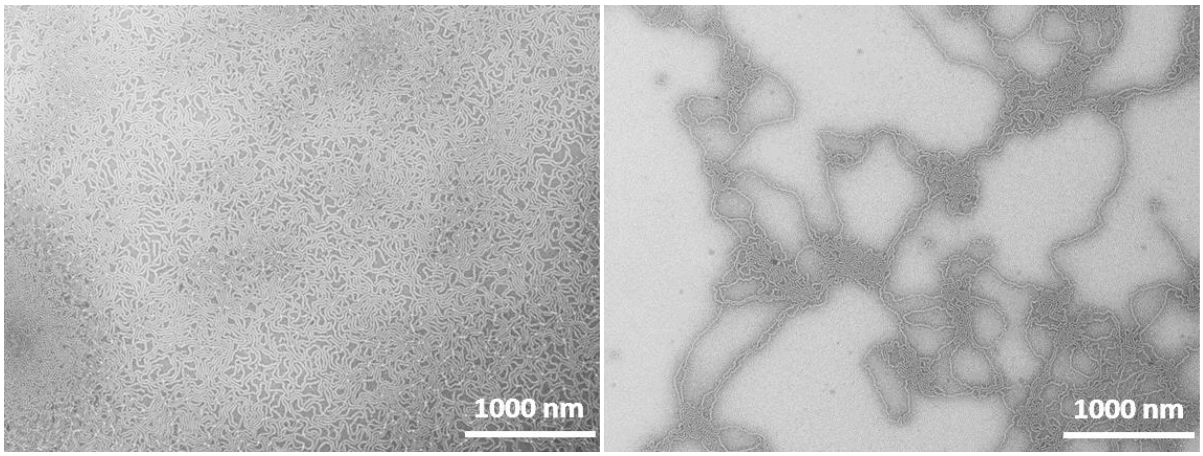

Figure 101: Additional TEM images of the self-assemblies formed by film rehydration from PBO_{42}-*b*-PG_{35}.

8.1.3. Calculation of the end-to-end distance and the contour length

Estimation of the end-to-end distance R_{coil} in coil-like conformation of the PBO blocks

R_{coil} of the PBO blocks in an coiled conformation was estimated using the average C-C bond length (0.146 nm)[218] and the bond angle of a tetrahedron (109.5 °).The DP was multiplied by 3 as every repeating unit consists of three bonds. The equation is as follows (DP = degree of polymerisation, l = lengths of one bond, θ = bond angle):[15]

$$R_{coil}{}^2 = 3 \cdot DP \cdot l^2 \cdot \frac{1-\cos\theta}{1+\cos\theta}$$

$$R_{coil} = \sqrt{3 \cdot 42 \cdot (0.146\,nm)^2 \cdot \frac{1-\cos 109.5}{1+\cos 109.5}} = 2.32 \text{ nm}$$

Estimation of the maximum chain lengths $R_{contour}$ in stretched conformation of the PBO blocks

$R_{contour}$ between the two ends of the polymer chain for an ideal stretched conformation of the PBO blocks was estimated using the average C-C bond length (0.146 nm)[218] and the bond angle of a tetrahedron (109.5 °).The DP was multiplied by 3 as every repeating unit consists of three bonds. The equation is as follows (DP = degree of polymerisation, l = lengths of one bond, θ = bond angle):[15]

$$R_{contour} = 3 \cdot DP \cdot l \cdot \sin\left(\frac{\theta}{2}\right)$$

$$R_{contour} = 3 \cdot 42 \cdot 0.146 \text{ nm} \cdot \sin\left(\frac{109.5}{2}\right) = 15.0 \text{ nm}$$

8.2. Synthesis, SUV and GUV formation of isotactic PBO-*b*-PG

8.2.1. Kinetic analysis

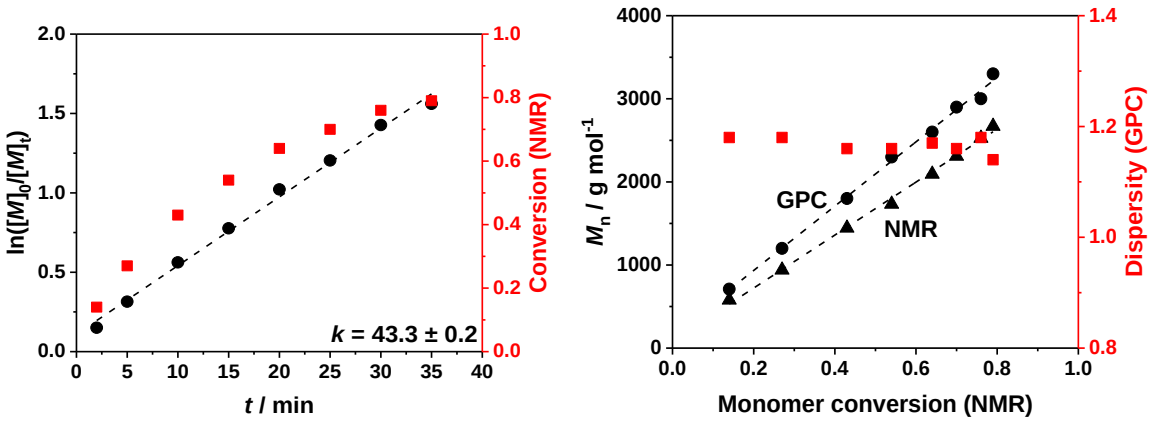

Figure 102: Kinetics of the (*R*/*S*)-PBO synthesis.

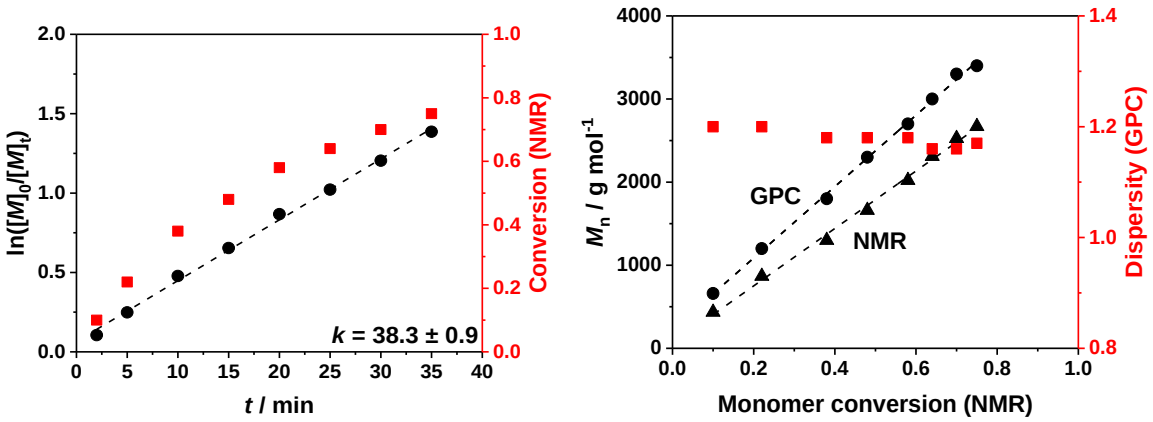

Figure 103: Kinetics of the (*R*)-PBO synthesis.

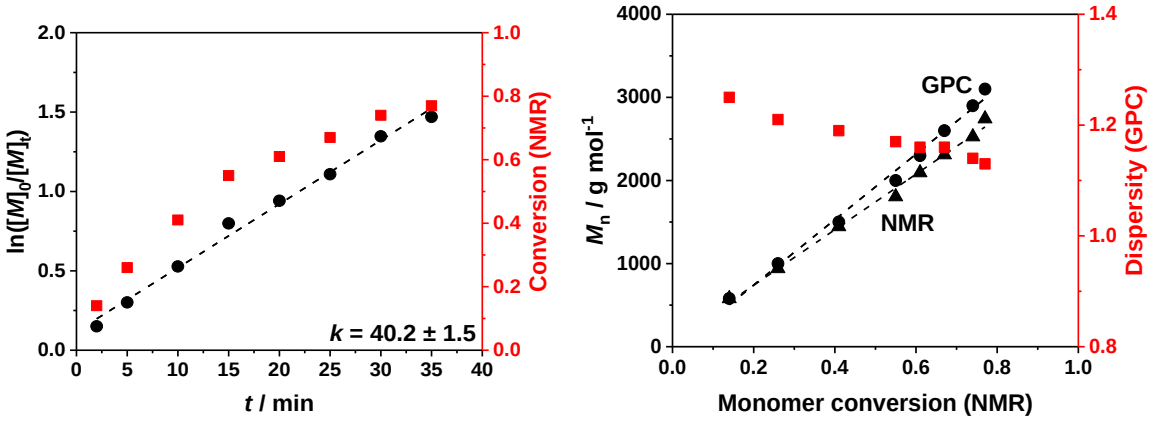

Figure 104: Kinetics of the (*S*)-PBO synthesis.

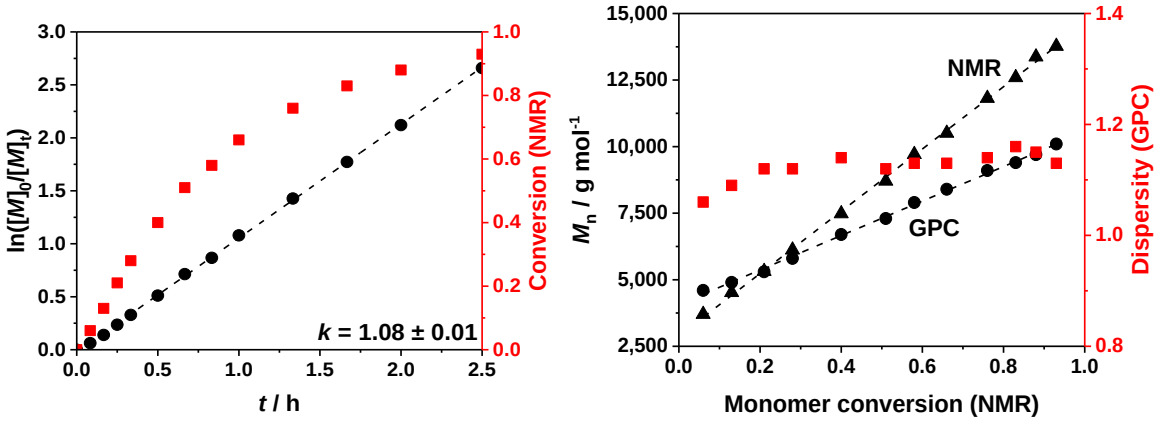

Figure 105: Kinetics of the (*R*/*S*)-PBO-*b*-(*R*/*S*)-PEEGE synthesis.

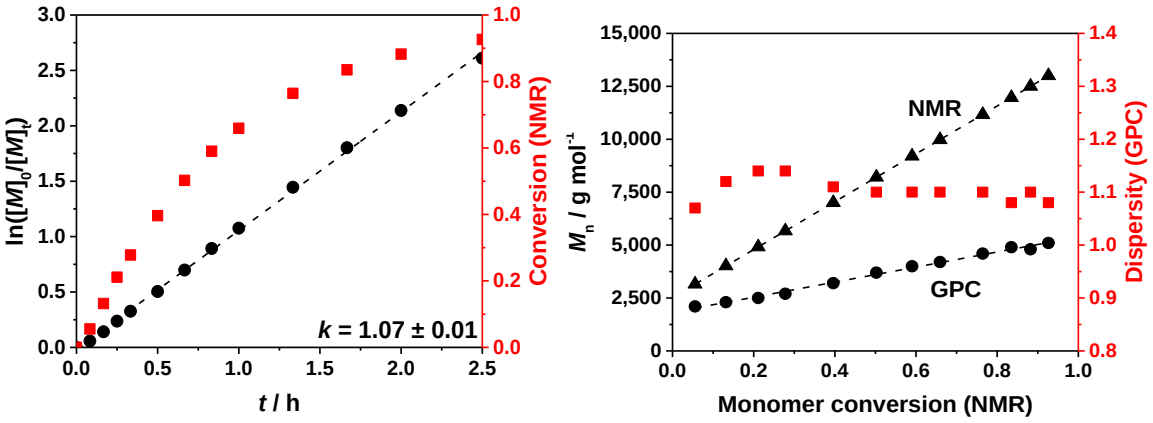

Figure 106: Kinetics of the (*R*)-PBO-*b*-(*R*)-PEEGE synthesis.

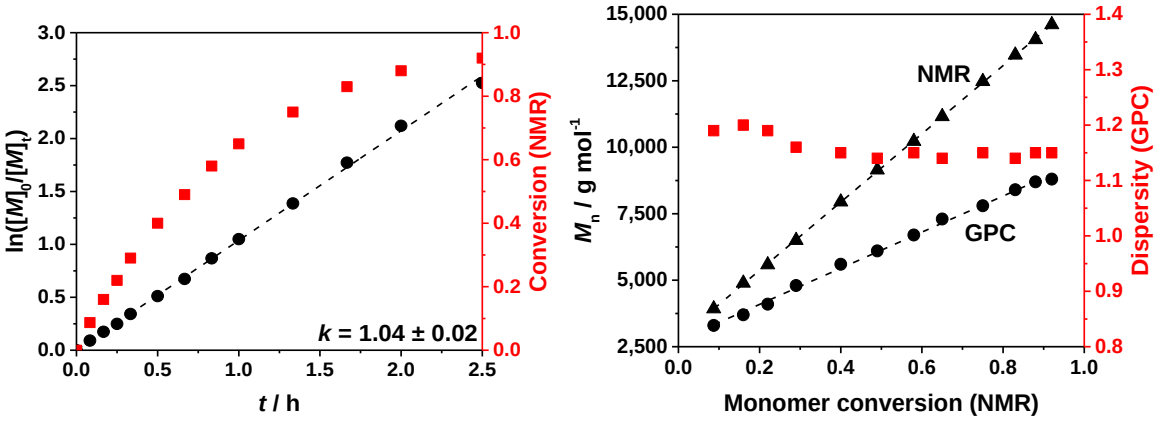

Figure 107: Kinetics of the (*S*)-PBO-*b*-(*S*)-PEEGE synthesis.

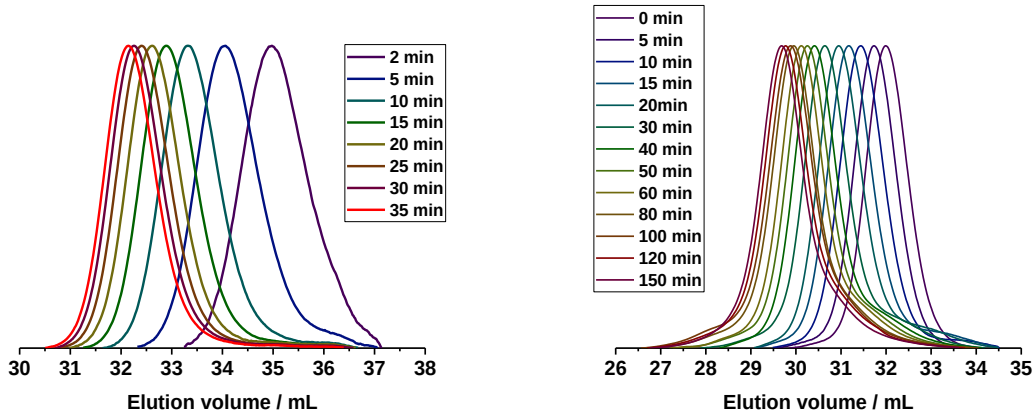

Figure 108: GPC traces of the kinetic measurements of (*R*/*S*)-PBO (left) and (*R*/*S*)-PBO-*b*-(*R*/*S*)-PEEGE (right).

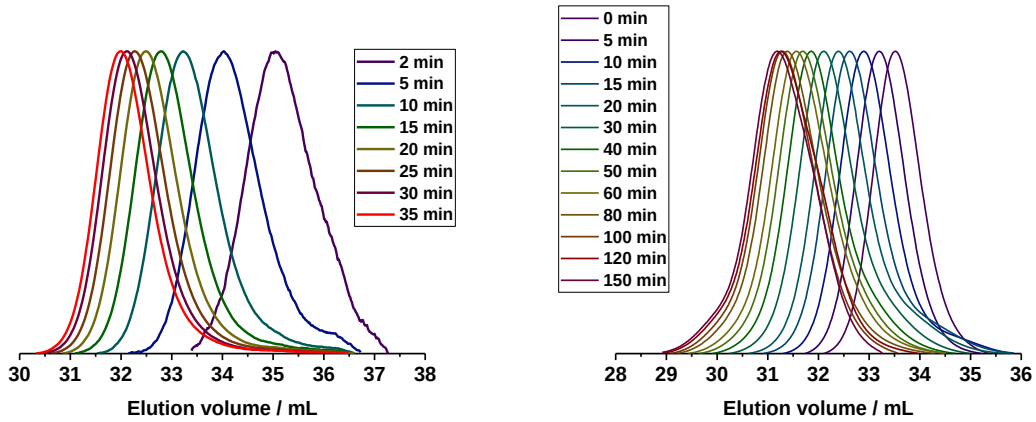

Figure 109: GPC traces of the kinetic measurements of (*R*)-PBO (left) and (*R*)-PBO-*b*-(*R*)-PEEGE (right).

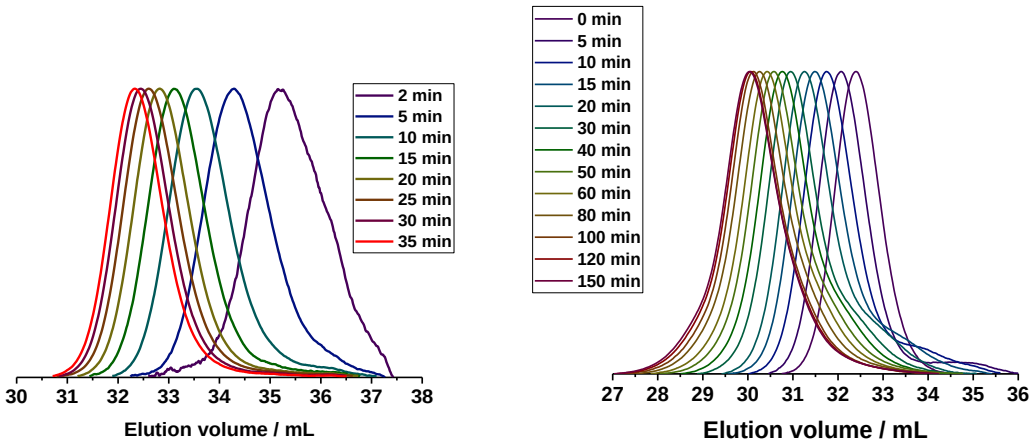

Figure 110: GPC traces of the kinetic measurements of (*S*)-PBO (left) and (*S*)-PBO-*b*-(*S*)-PEEGE (right).

8.2.2. BCP characterisation

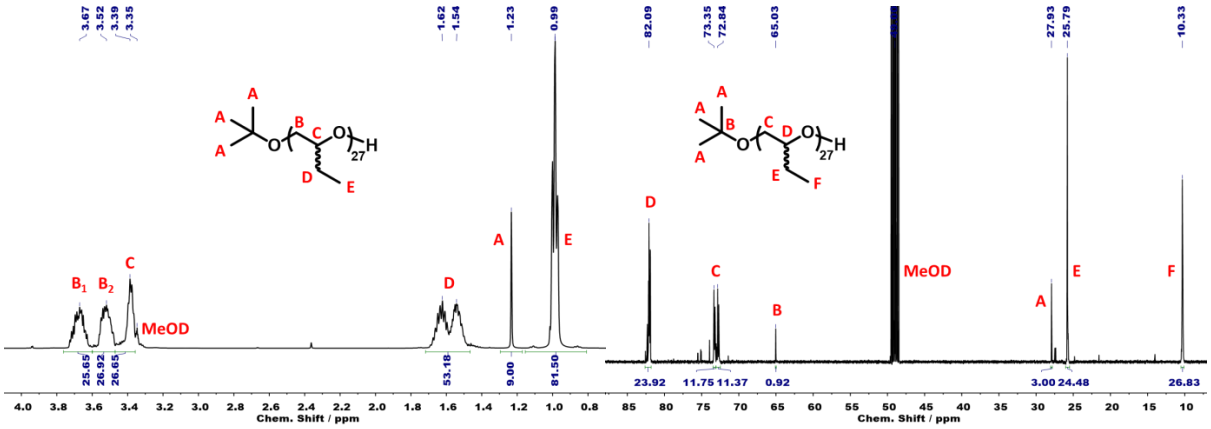

Figure 111: ^{1}H NMR spectrum (left) and ^{13}C NMR spectrum (right) of (*R*/*S*)-PBO$_{27}$ in MeOD.

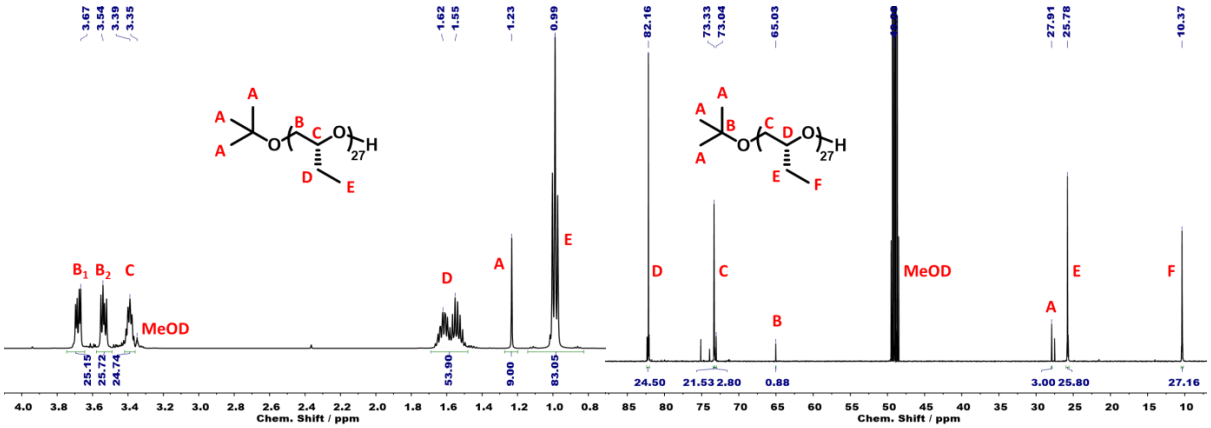

Figure 112: ^{1}H NMR spectrum (left) and ^{13}C NMR spectrum (right) of (*R*)-PBO$_{27}$ in MeOD.

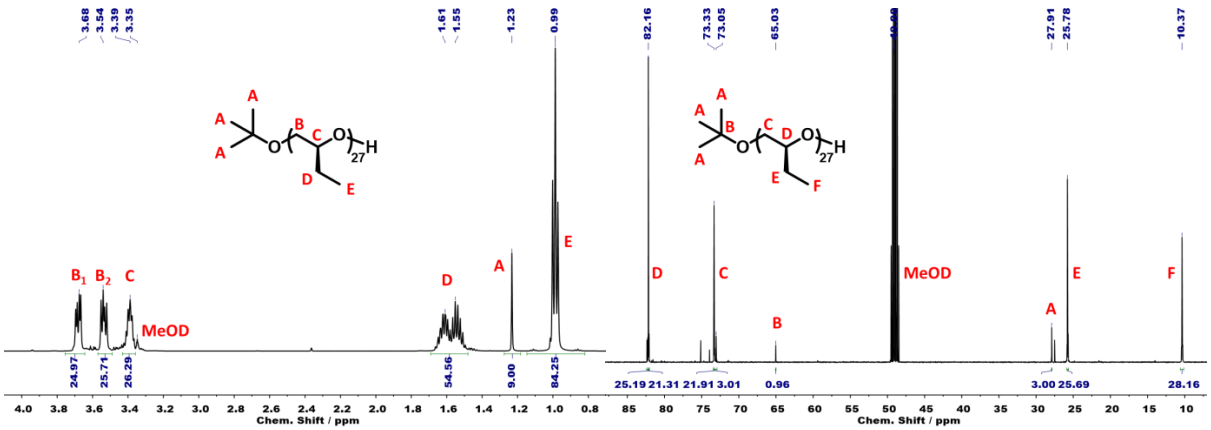

Figure 113: ^{1}H NMR spectrum (left) and ^{13}C NMR spectrum (right) of (*S*)-PBO$_{27}$ in MeOD.

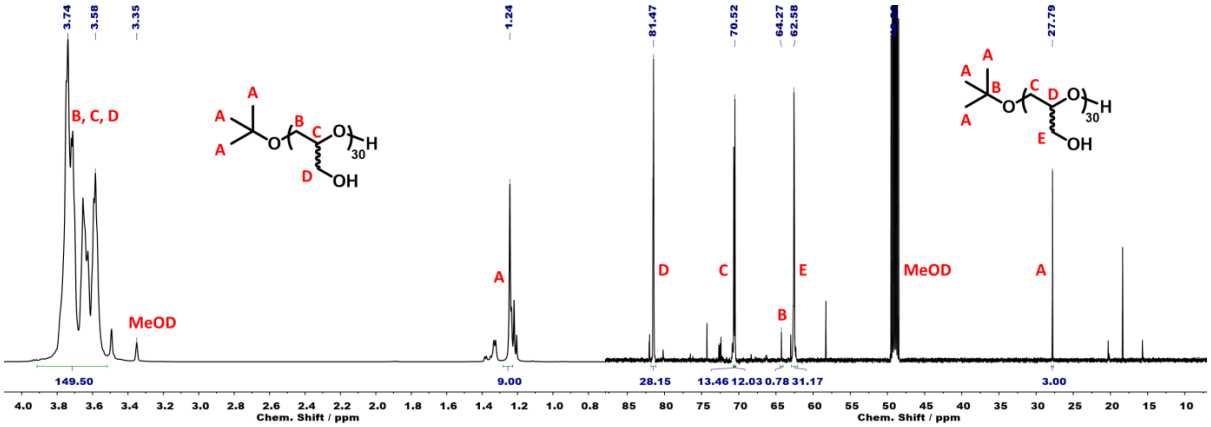

Figure 114: ^{1}H NMR spectrum (left) and ^{13}C NMR spectrum (right) of (*R*/*S*)-PG$_{30}$ in MeOD.

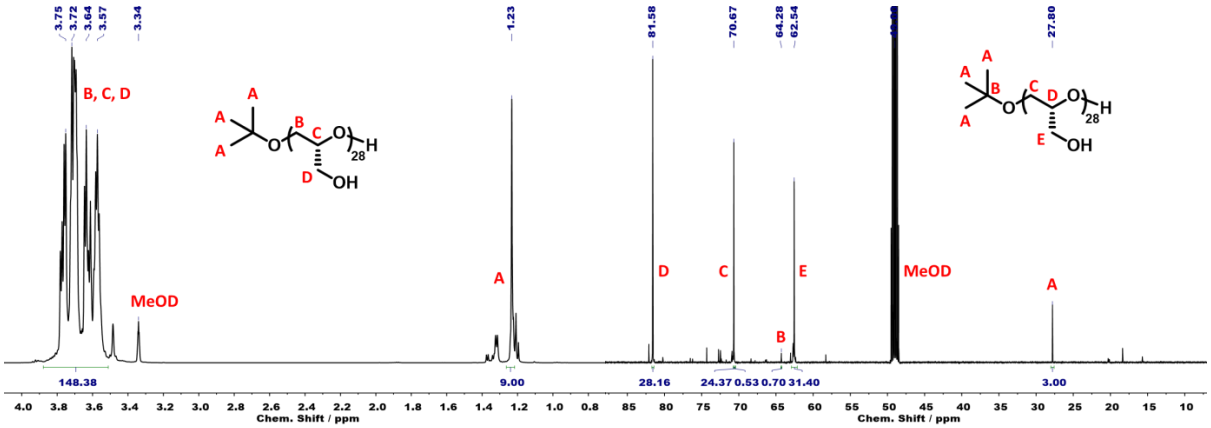

Figure 115: ^{1}H NMR spectrum (left) and ^{13}C NMR spectrum (right) of (*R*)-PG$_{28}$ in MeOD.

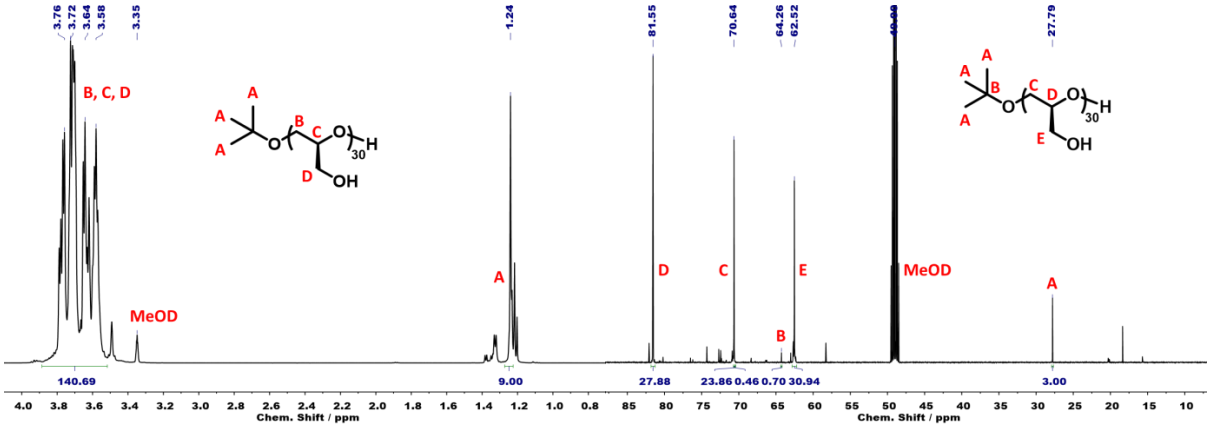

Figure 116: ^{1}H NMR spectrum (left) and ^{13}C NMR spectrum (right) of (*S*)-PG_{30} in MeOD.

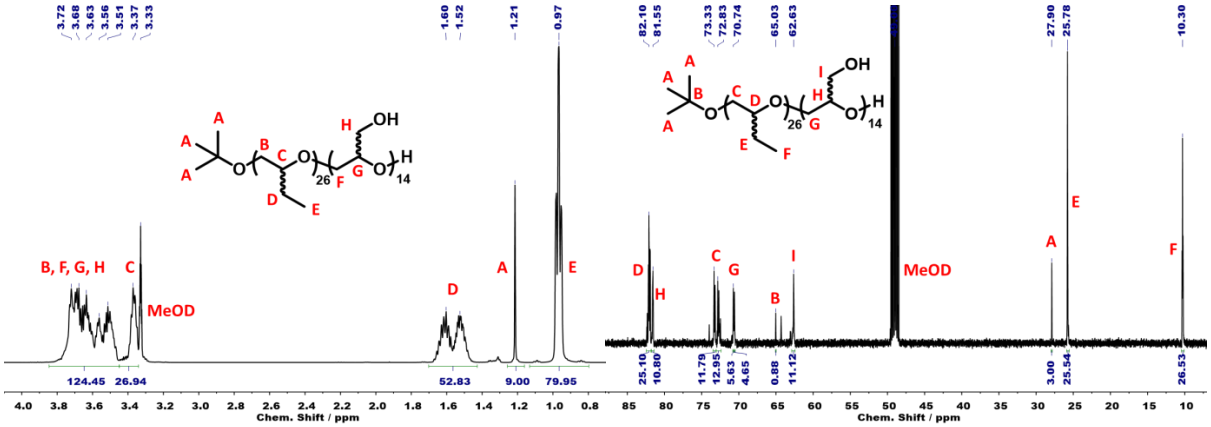

Figure 117: ^{1}H NMR spectrum (left) and ^{13}C NMR spectrum (right) of (*R*/*S*)-PBO_{26}-*b*-(*R*/*S*)-PG_{14} in MeOD.

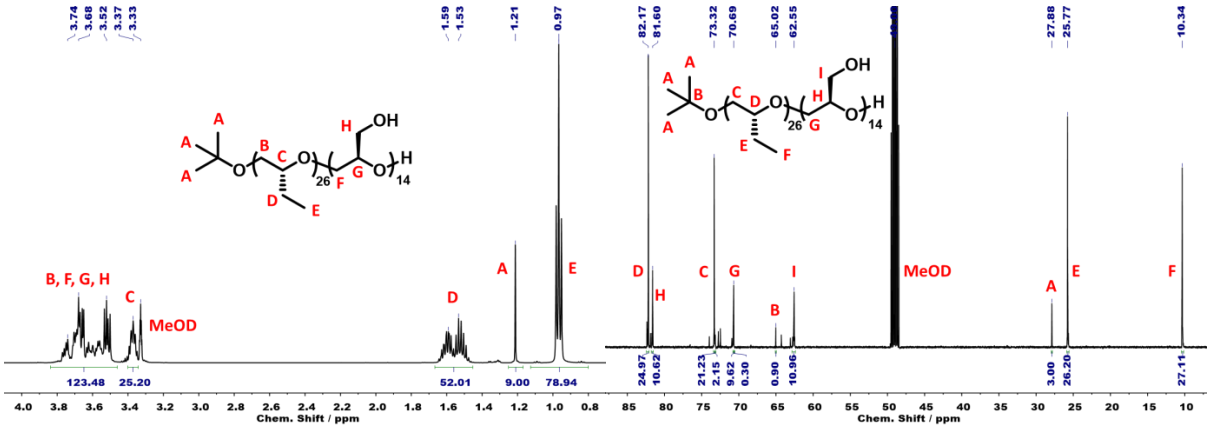

Figure 118: ^{1}H NMR spectrum (left) and ^{13}C NMR spectrum (right) of (*R*)-PBO_{26}-*b*-(*R*)-PG_{14} in MeOD.

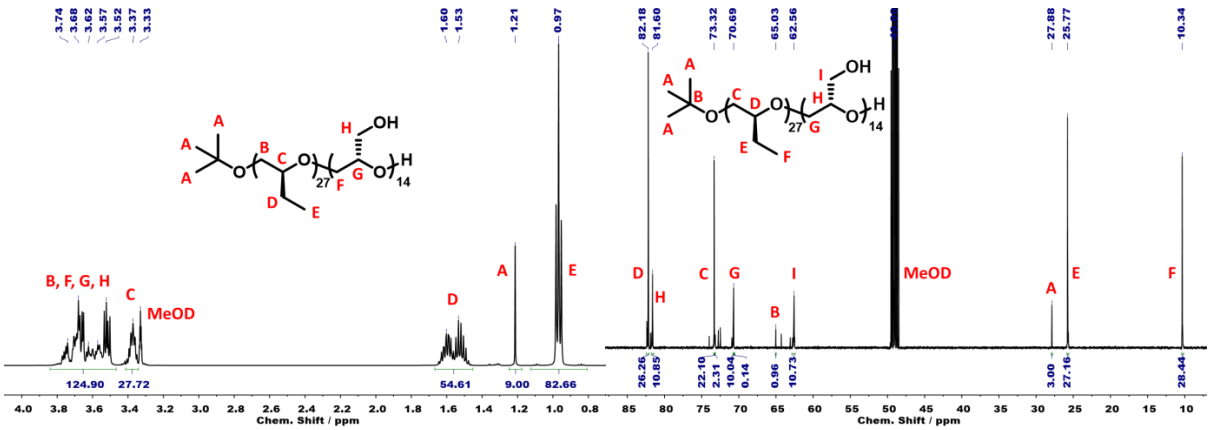

Figure 119: ^{1}H NMR spectrum (left) and ^{13}C NMR spectrum (right) of (*S*)-PBO$_{27}$-*b*-(*S*)-PG$_{14}$ in MeOD.

8.2.3. Self-assembly characterisation

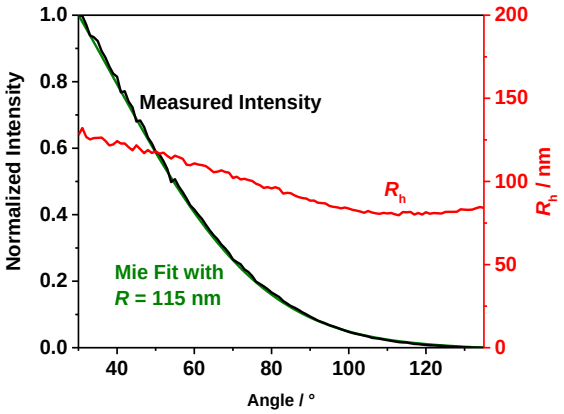

Figure 120: DLS and SLS data (Mie fit) of (*R*/*S*)-PBO$_{26}$-*b*-(*R*/*S*)-PG$_{14}$ SUVs before extrusion.

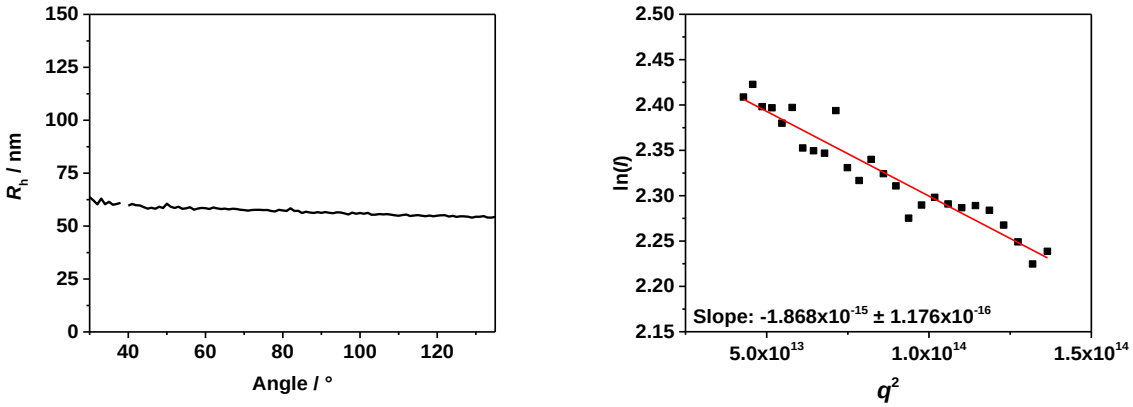

Figure 121: DLS and SLS data (Guinier fit) of (*R*)-PBO$_{26}$-*b*-(*R*)-PG$_{14}$ SUVs before extrusion.

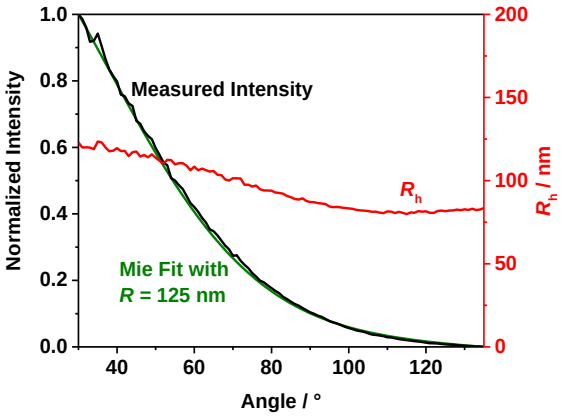

Figure 122: DLS and SLS data (Mie fit) of (*S*)-PBO$_{27}$-*b*-(*S*)-PG$_{14}$ SUVs before extrusion.

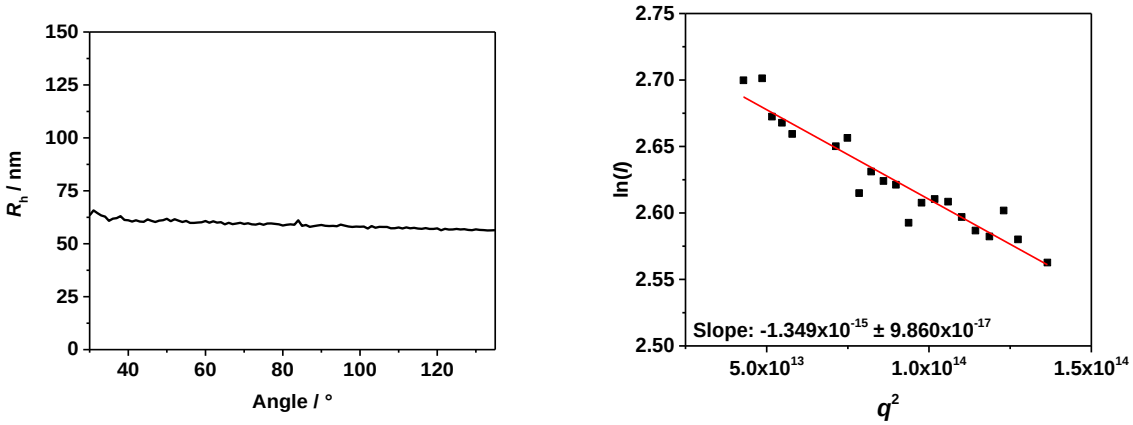

Figure 123: DLS and SLS data (Guinier fit) of (*R*/*S*)-PBO$_{26}$-*b*-(*R*/*S*)-PG$_{14}$ SUVs after extrusion with a 100 nm membrane.

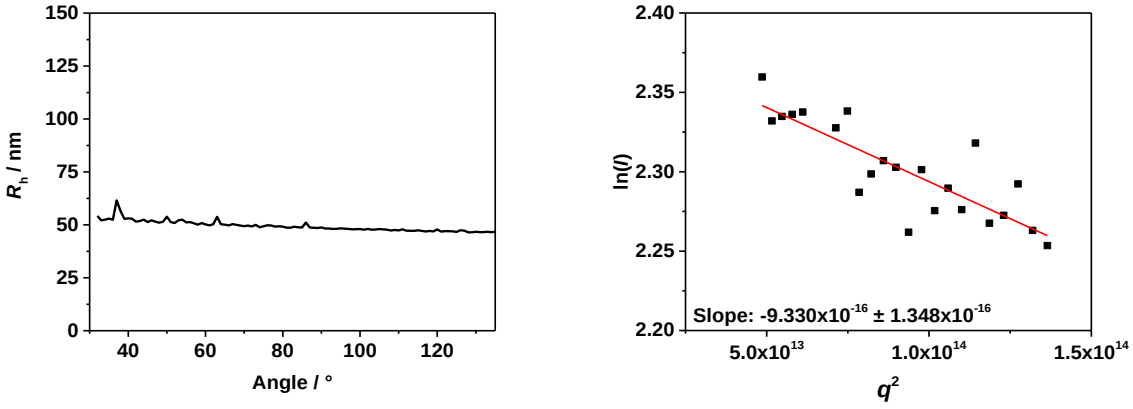

Figure 124: DLS and SLS data (Guinier fit) of (*R*)-PBO$_{26}$-*b*-(*R*)-PG$_{14}$ SUVs after extrusion with a 100 nm membrane.

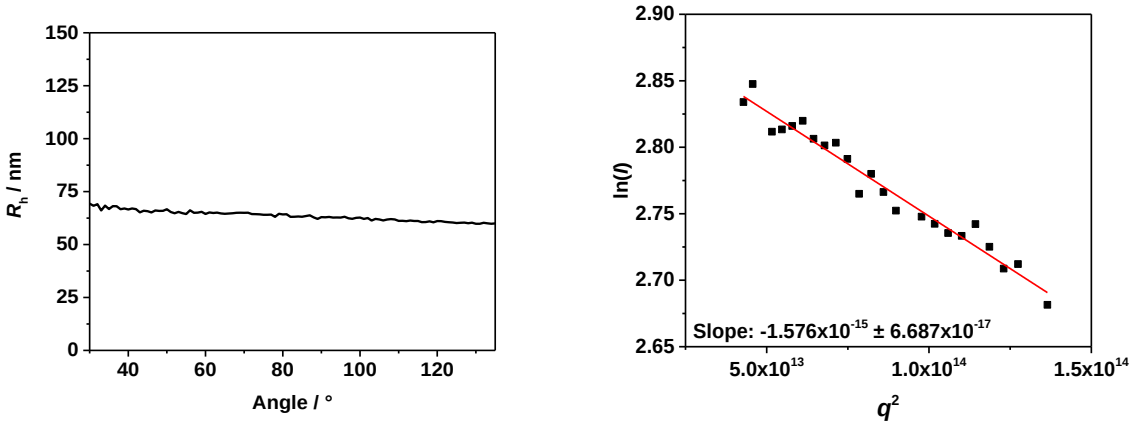

Figure 125: DLS and SLS data (Guinier fit) of (*S*)-PBO_{27}-*b*-(*S*)-PG_{14} SUVs after extrusion with a 100 nm membrane.

8.2.4. Calculation of the effective conformation

For a fully stretched conformation the contour length $R_{contour}$ would be:

$$R_{contour} = l * n * d * \sin\left(\frac{\theta}{2}\right)$$

PBO_{26} has 3 bonds per repeating unit (l) and 26 repeating units (n). Taking the bond length of PEO as a reference (d), this becomes for a tetrahedral bond angle (θ):

$$R_{contour} = 3 * 26 * 0.145\ \text{nm} * \sin\left(\frac{109.5}{2}\right) = 9.2\ \text{nm}$$

The end-to-end distance of a random coil-like conformation (R_{coil}) is given as

$$R_{coil} = \sqrt{\frac{1 - cos\theta}{1 + cos\theta} * l * n * d}$$

Taking the same values as above results for PBO_{26} in

$$R_{coil} = \sqrt{\frac{1.33}{0.67} * 3 * 26} * 0.145\ \text{nm} = 1.8\ \text{nm}$$

Effective conformation:

The side chain of PBO prevents an arrangement in a perfect coil-like conformation. However, a fully stretched conformation can also not be achieved. Consequently, it exhibits a mixed conformation of

both components. The degree of stretching *x* can thus be calculated using the membrane thickness *l* (effective length $R_{eff} = l/2$ as it is a bilayer system) and the theoretical lengths $R_{contour}$ and R_{coil} as follows:

$$R_{eff} = x * R_{contour} + (1 - x) * R_{coil}$$

For PBO_{26} *x* is accordingly

$$x = \frac{R_{eff} - R_{coil}}{R_{contour} - R_{coil}} = \frac{5.6\ \text{nm} - 1.8\ \text{nm}}{9.2\ \text{nm} - 1.8\ \text{nm}} = 51\%$$

--> PBO is 51% stretched in a bilayer membrane

8.2.5. OmpF expression and purification

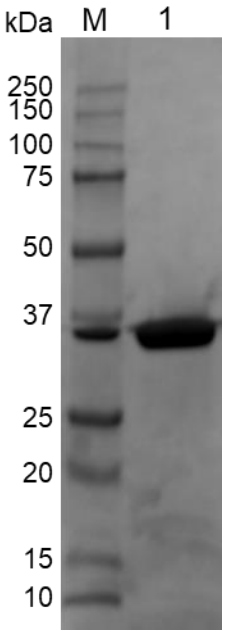

Figure 126: SDS-PAGE of purified OmpF. M: Marker (Precision Plus Protein standard), Lane 1: Purified OmpF in 3% OG. 10 µg protein were boiled at 95 °C for 5 min in loading buffer (f.c. 2% SDS, 50 mM Tris-HCl pH 6.8, 10% glycerol, 0.004% bromophenol blue, 100 mM DTT).